Numerical Investigation of Micro-structural Transport Parameters and Corrosion Modelling of Metallic Supported Solid Oxide Fuel Cells

Georg Reiss

ICE Strömungsforschung GmbH

Montanuniversität Leoben

February 2015

Abstract

Metallic supported Solid Oxide Fuel Cells (SOFCs) are considered to be a cost-effective and competitive alternative to state-of-the-art all-ceramic SOFCs. In substituting the supporting ceramic by a porous metal-layer, the advantages of the ductile alloy can be exploited and the mechanical strength is improved. However, this new technology originates different problems, which have to be solved before the product is ready for the market. The most important issue is corrosion, inevitably taking place at the operating conditions. The growing oxide layer will continuously fill the pores and a sufficient gas-diffusion through the layer may be one limiting factor for the long-term applicability of metallic supported SOFCs.

In order to understand the implications of corrosion on the gas-diffusion, a modelling study on a microstructural level was pursued. The metallic support was measured with X-ray tomography and reconstructed into a computational geometry. Different surface representations (stair-step, smooth) were analysed and their influence on the results assessed. A geometrical evaluation tool was programmed that determines e.g. porosity distribution, averaged pore diameter, number of pores.

An enhanced corrosion model based on Wagner's theory was implemented in *OpenFOAM* which describes the growth of the oxide thickness depending on corrosion rate constants, which can be easily retrieved by measurements. The model is applied on complex 3-D microstructures, where also the shrinkage of the alloy, due to consumption of Cr-ions for the oxide formation, is taken into account as a boundary condition.

The transient oxide growth and its corresponding change of the microstructure impedes the gas-diffusion. This was assessed by determining the change of the concentration over-potential, which results from a decreased mass transport. Furthermore, the effective diffusion coefficient was computed, which is an important input parameter for simulations on cell- and stack-level.

It has been shown in this work that the application of periodic boundary conditions for the lateral walls increase the accuracy of the solution dramatically, compared to the state-of-the-art symmetry approach, and that more reliable results can be obtained from smaller geometries. In addition to that, it is now possible to evaluate the change of the microstructure due to corrosion and its transient influence on the gas-diffusion, which allows predicting the degradation of the SOFC caused by corrosion of the metallic support.

Kurzfassung

Die Entwicklung metallgestützer Hochtemperatur-Brennstoffzellen (solid oxide fuel cells SOFCs) zeigte eine vergleichbare, aber kostengünstigere Alternative zu herkömmlichen keramischen SOFCs. Die Metallstützschicht verbessert durch ihre Duktilität die mechanischen Eigenschaften der SOFC, birgt aber andere Probleme, die vor einer Vermarktung gelöst werden müssen. Die größte Herausforderung in Bezug auf die Metallstützschicht ist die Korrosion. Die wachsende Oxidschicht füllt das Porenvolumen, wodurch die Gasdiffusion und die Versorgung der Anode mit genügend Brennstoff erschwert wird. Dies scheint ein limitierender Faktor in der Lebensdauer von metallgestützten SOFCs zu sein.

Um abschätzen zu können, welchen Einfluss die Korrosion auf den Massentransport hat, wurden Simulationsmodelle auf Mikrostrukturebene entwickelt. Die Metallstützschicht wurde mit Röntgentomographie vermessen und in ein Rechengitter umgewandelt. Dabei wurden auch unterschiedliche Oberflächen (stair-step, geglättet) untersucht und deren Einfluss auf das Simulationsergebnis ermittelt. Zudem wurde ein Algorithmus programmiert, mit dessen Hilfe z.B. die Porositätsverteilung, der mittlere Porendurchmesser oder die Anzahl der Poren bestimmt werden können.

Das Korrosionsmodell basiert auf Wagners Theorie und wurde in *OpenFOAM* implementiert. Damit konnte das Wachstum der Oxidschicht in Abhängigkeit der gemessenen Wachstumsraten ermittelt werden. Die Rechnungen wurden auf den komplexen 3-D Mikrostrukturen ausgeführt. Durch das Oxidwachstum kommt es zu einer Schrumpfung des Metalls, da Cr-Ionen aus dem Metall in das Oxid eingebaut werden. Dieses Zurückziehen wurde als Randbedingung berücksichtigt.

Die Änderung des Porenvolumens führt zu einer Verringerung des diffusiven Massentransports. Dieser Effekt wurde durch die Bestimmung der Konzentrationsüberspannung ermittelt und bewertet. Außerdem wurde der effektive Diffusionskoeffizient der Mikrostruktur bestimmt, welcher als wichtiger Modellparameter für Simulationen auf Zell- und Stacklevel verwendet wird.

Es konnte in dieser Arbeit gezeigt werden, dass periodische Randbedingungen die Genauigkeit der Rechenergebnisse im Vergleich zu den herkömmlich verwendeten Randbedingungen erheblich erhöhen und es somit möglich ist, bessere Ergebnisse auf kleineren Geometrien zu

bekommen. Der größte Fortschritt konnte aber mit der neuen Korrosionssimulation erzielt werden, da nun die zeitliche Änderung der Mikrostruktur und deren Einfluss auf die Gasdiffusion ermittelt werden kann. Dadurch ist eine Abschätzung der Degradation der SOFC aufgrund von Korrosion der Metallstützschicht möglich.

Acknowledgements

I would like to thank Wilhelm Brandstätter for giving me the possibility to work on this project and for his support and encouragement. The discussions and feedback from Christian Weiß helped me on my way. I am very grateful to Henrik Lund Frandsen for his continuous support and challenging feedback and for giving me guidance in the scientific world.

It was a pleasure and inspiring to work with my colleagues from the *METSAPP*-project, who established a friendly, cooperative and innovative atmosphere. Many thanks to my colleagues at ICE Strömungsforschung GmbH, especially Bernhard Gschaider who was my guider with his swiss army knife through *OpenFOAM*, and Andrea Kreuzig who took it upon herself to proof-read my thesis.

The *METSAPP*-project has received funding from the European Union's Seventh Framework Programme (FP7/2007-2013) for the Fuel Cells and Hydrogen Joint Technology Initiative under grant agreement n° 278257.

Finally, I want to thank my wife and my two children for their love, support and for being the way they are. They are making my life worthwhile, and I am grateful for our time together.

Affidavit

I declare in lieu of oath, that I wrote this thesis and performed the associated research myself, using only literature cited in this volume.

.....

Georg Reiss

Contents

Abstract **i**

Acknowledgements **iv**

List of Notations **x**

1 Introduction **1**

1.1 Motivation and objectives 1

1.2 Publications 7

1.3 Outline 7

2 SOFC in a minute **9**

2.1 Basics and loss mechanisms 9

2.2 Metallic supported SOFC 12

3 Theoretical background **14**

3.1 Corrosion 14

3.1.1 High-temperature corrosion theory 14

3.1.2 Weight-gain measurement 21

3.2 Mass-transport 22

3.2.1 Convective flow and permeability 23

3.2.2 Diffusion modelling 27

3.2.3 Diffusion coefficient modelling 35

3.2.4 Effective diffusion coefficient 37

4 Geometry reconstruction **41**

4.1 Sample measurement 41

4.1.1 Focused-ion-beam scanning-electron-microscopy 42

4.1.2 X-ray computed tomography 43

4.2 Reconstruction algorithm 43

4.3 Representative equivalent volume 46

4.4 Smoothing of the geometry 50

4.5 Artificial geometry 56

5 Simulation and modelling **58**

5.1 Corrosion simulation 58

5.1.1 Simulation approach 58

5.2 Porosity distribution and geometric evaluation 65

5.3 Mass-transport simulation 66

5.3.1 Flow simulation 66

5.3.2 Evaluation of the scaling factor for the effective diffusion coefficient . . . 70

5.3.3 Evaluation of the scaling factor with corrosion 72

6 Validation **74**

6.1 Corrosion model 74

6.1.1 One-dimensional growth 74

6.1.2 Growth correction for voxel geometries 76

6.1.3 Growth on convex and concave surfaces 77

6.1.4 Comparison to micro-graphs 80

6.1.5 Comparison to mass-gain measurement of metal-support 82

6.2 Mass transport 84

6.2.1 Permeability 84

6.2.2 Diffusion 87

6.2.3 Effective diffusion coefficient 88

7 Results **97**

7.1 Geometric evaluation 97

7.2 Mass-transport model 100

7.2.1 Permeability 100

7.2.2 Effective diffusion coefficient 104

7.3 Corrosion 106

8 Conclusions **111**

8.1 Mass-transport modelling 111

8.2 Corrosion modelling 112

8.3 Applications 113

8.4 Future Work 113

List of Tables **115**

List of Figures **117**

Bibliography **124**

List of Notations

$R_{D(\text{anode})}$ impedance resistance related to the diffusion (V)

β transfer coefficient (-)

$\Delta r^{t \to t+\Delta t}$ metal retraction (m)

Δve_i vector average of each vertex (m)

ϵ porosity (-)

ϵ_{corr} porosity caused by corrosion (-)

ϵ_{eff} effective porosity (-)

η_{act} activation polarisation (V)

η_{conc} concentration polarisation (V)

Γ thermodynamic factor (-)

γ scale factor for smoothing(-)

κ geometry surface correction factor (-)

λ first Lamé constant (Pa s)

λ mean free path of gas molecules (m)

$\langle \boldsymbol{u} \rangle$ bulk-volume average velocity ($\mathrm{m\,s^{-1}}$)

$\mathfrak{D}_{ij}$ Maxwell-Stefan diffusivity ($\mathrm{m^2\,s^{-1}}$)

$\mathscr{D}_{ij}$ binary diffusion coefficient ($\mathrm{m^2\,s^{-1}}$)

$\mathscr{D}_{ij}^{eff}$ effective binary diffusion coefficient ($\mathrm{m^2\,s^{-1}}$)

$\mathscr{D}_{k,i}$ effective Knudsen diffusion coefficient ($\mathrm{m^2\,s^{-1}}$)

μ dynamic viscosity ($\mathrm{Pa\,s}$)

Ω_D diffusion collision integral (-)

ρ_i mass density ($\mathrm{kg\,m^{-3}}$)

ρ_m density of metal ($\mathrm{kg\,m^{-3}}$)

ρ_{ox} density of oxide ($\mathrm{kg\,m^{-3}}$)

σ_{ij} characteristic Lennard-Jones length (Å)

τ tortuosity (-)

θ negative scale factor for smoothing (-)

$\mathrm{G^0}$ standard Gibbs free-energy (J)

$\mathrm{PB_{ratio}}$ Pilling-Bedworth ratio (-)

$\boldsymbol{f}$ volume forces ($\mathrm{kg\,s^{-2}\,m^{-2}}$)

$\boldsymbol{J}_i$ molar diffusion flux ($\mathrm{kmol\,m^{-2}\,s^{-1}}$)

$\boldsymbol{j}_i$ mass diffusion flux ($\mathrm{kg\,m^{-2}\,s^{-1}}$)

$\boldsymbol{j}_i^{porous}$ superficial axial diffusion ($\mathrm{kg\,m^{-2}\,s^{-1}}$)

$\boldsymbol{j}_{i,p}$ actual diffusion flux in the pores ($\mathrm{kg\,m^{-2}\,s^{-1}}$)

$\boldsymbol{k}_{ij}$ permeability tensor ($\mathrm{m^2}$)

$\boldsymbol{N}_i$ molar flux ($\mathrm{kmol\,m^{-2}\,s^{-1}}$)

$\boldsymbol{n}_i$ mass flux ($\mathrm{kg\,m^{-2}\,s^{-1}}$)

$\boldsymbol{n}_t$ total mass flux ($\mathrm{kg\,m^{-2}\,s^{-1}}$)

$\boldsymbol{S}$ normal surface vector ($\mathrm{m^2}$).

$\boldsymbol{U}$ molar averaged velocity ($\mathrm{m\,s^{-1}}$)

$\boldsymbol{u}$ velocity ($\mathrm{m\,s^{-1}}$)

$\boldsymbol{v}_i$ species velocity ($\mathrm{m\,s^{-1}}$)

A area ($\mathrm{m^2}$)

a ionic jump distance (Å)

A_{corr} area of the corroding faces ($\mathrm{m^2}$)

A_{init} initial surface area ($\mathrm{m^2}$)

A_{ret} area of the retracting faces ($\mathrm{m^2}$)

B_1 corrosion constant ($\mathrm{m\,s^{-1}}$)

B_2 corrosion constant ($\mathrm{s^{-1}}$)

C proportionality constant ($\mathrm{m^3\,mol^{-1}}$)

c concentration ($\mathrm{mol\,m^{-3}}$)

c_i molar density ($\mathrm{mol\,m^{-3}}$)

D ionic diffusivity ($\mathrm{m^2\,s^{-1}}$)

d_p mean pore diameter (m)

d_{H_2} diameter of hydrogen molecule (m)

E^0 standard electrode potential (V)

E_{rev} reversible or open circuit voltage (OCV) (V)

F Faraday constant ($\mathrm{C\,mol^{-1}}$)

f scaling factor (-)

F_c number of corroding faces per cell (-)

G oxide growth parameter (-)

I current (A)

i current density ($\mathrm{A\,m^{-2}}$)

i_0 exchange current density ($\mathrm{A\,m^{-2}}$)

j_{ox} flux of Cr-ions ($\mathrm{mol\,m^{-2}\,s^{-1}}$)

k scalar permeability ($\mathrm{m^2}$)

k_l linear rate constant ($\mathrm{m\,s^{-1}}$)

K_n Knudsen number (-)

k_p parabolic rate constant ($\mathrm{m^2\,s^{-1}}$)

$k_{p,m}$ parabolic rate constant ($\mathrm{kg^2\,m^{-4}\,s^{-1}}$)

l edge length of a cube (m)

L_D Debye length (m)

L_{eff} actual distance between two points (m)

M molecular weight ($\mathrm{g\,mol^{-1}}$)

m mass (kg)

m_{init} initial weight (kg)

M_m molecular weight of metal ($\mathrm{g\,mol^{-1}}$)

M_{ox} molecular weight of oxide ($\mathrm{g\,mol^{-1}}$)

m_{ox} weight of the oxide (kg)

n number of corroding faces per retraction face (-)

N_a Avogadro's number (mol^{-1})

n_e number of electrons per reaction (-)

p pressure (Pa)

p_{H_2O} partial pressure water vapour (Pa)

p_{H_2} partial pressure hydrogen (Pa)

p_{O_2} partial pressure oxygen (Pa)

Q volume flow rate ($\mathrm{m}^3\,\mathrm{s}^{-1}$)

q specific flow rate ($\mathrm{m}\,\mathrm{s}^{-1}$)

R universal gas constant ($\mathrm{J}\,\mathrm{mol}^{-1}\,\mathrm{K}^{-1}$)

r radius of capillary tubes (m)

$R_{e,i}$ electronic and ionic resistance (Ω)

s Forchheimer term (m)

S_{w_i} molar source or sink ($\mathrm{kmol}\,\mathrm{m}^{-3}\,\mathrm{s}^{-1}$)

s_{w_i} mass source or sink ($\mathrm{kg}\,\mathrm{m}^{-3}\,\mathrm{s}^{-1}$)

T temperature (K)

t time (s)

t_p time at witch linear growth is switched to parabolic growth (s)

t_r residence time (s)

U_l potential losses (V)

U_{cell} cell voltage (V)

V_e entire volume (m^3)

V_m partial molar volume of the out-diffusing species ($m^3\,mol^{-1}$)

V_{cell} volume of one computational cell (m^3)

V_{diff} change of pore volume (m^3)

ve'_i displacement vector (m)

ve_j vector of each vertex (m)

w_i mass fraction (-)

w_{ij} weight for each vertex (-)

w_{ox} mass gain ($kg\,m^{-2}$)

X_1 oxide thickness below which Nernst-Einstein relationship is valid (m)

x_{H_2O} molar fraction of water vapour (-)

x_{H_2} molar fraction of hydrogen (-)

x_{O_2} molar fraction of oxygen (-)

x_{corr} oxide thickness (m)

$x_{corr}^{t\rightarrow t+\Delta t}$ change of oxide thickness during one time step (m)

z number of metal atoms (-)

z_{ox} number of cations per formula oxide (-)

Chapter 1

Introduction

1.1 Motivation and objectives

Solid Oxide Fuel Cells (SOFCs) are a promising, alternative technology that offers effective conversion of chemical stored energy to electricity, with efficiencies as high as 55 % and even up to 90 % in hybrid configuration with gas turbines and combined heat and power generation [58]. So it is claimed since the last decades and although there are some example applications [10, 17, 23] the big break-through in SOFC-technology and the reliability for the mass market is still not reached. It seems that SOFCs are destined to be a niche product.

One reason may lie in the higher production costs for the different ceramic materials compared to conventional power generation. Another reason which is a more prominent one is the durability and reliability of SOFCs. The degradation of the SOFC is defined as potential drop at constant current density during operating lifetime (expressed in $\mu V\,h^{-1}$). Every single component can contribute to the overall degradation and the most common failure mechanisms for ceramic SOFCs are [25, 89, 101]:

1. *Anode*:

   (a) coarsening of nickel particles;

   (b) crack formation in the electrolyte during re-oxidation of the anode support;

   (c) carburisation on nickel particles during internal reforming;

   (d) formation of nickel sulfide when using unfiltered hydrocarbon fuel.

2. *Electrolyte*:

   (a) loss of ionic conductivity due to phase changes, impurities and dopant diffusion;

   (b) cracks caused by thermal cycling, volume expansion, stresses;

   (c) delamination from either the anode or the cathode.

3. *Cathode*:

   (a) densification of the structure;

   (b) reaction with the zirconia electrolyte and formation of insulation phases;

   (c) reaction with volatile chromium species from the interconnect.

4. *Interconnect*:

   (a) formation of less-conductive oxide layers.

The assembling of SOFCs in stacks and varying operating conditions provoke additional problems with e.g. sealing, stresses, evenly flow distribution, thermal-cycling etc., which can accelerate the above mentioned failure mechanisms. Recent developments try to decrease the operating temperature below 800 °C as this will result in a simplification of the design and a higher long-term stability of the system [89]. In order to minimise the accompanied performance loss due to higher ohmic losses in the electrolyte, higher conductive materials were developed. Operating the SOFC at even lower temperatures (600 °C to 700 °C) will allow the usage of new materials to further improve the cell and lower the overall costs.

These are the main aims for the development of Metallic Supported Solid Oxide Fuel Cells (MS-SOFCs). In this new technology the ceramic support of the anode is replaced by a cheaper porous metallic support which exhibits a number of advantages such as a higher re-oxidation tolerance of the applied alloys, improved mechanical strength and a higher thermal conductivity

of the substrate. Recent metallic supported cell and stack developments have shown very promising results compared to the state-of-the-art all-ceramic SOFC [7, 9, 28–30, 59, 90–92]. Nevertheless, the porous metallic substrate is prone to other failure mechanisms which are unique for this technology e.g.: Creep may lead to a loss of integrity [54], and the corrosion of the porous metallic substrate will occur even at low water vapour partial pressures and will change the microstructure.

The variety of possible failure mechanisms and their interaction, combined with several coupled physical phenomena taking place during the operation of an SOFC-stack, makes it virtually impossible to attribute measurement results to failures. The attempt to understand the physics, such as electronic and ionic charge transfer; gas diffusion and flow; electro-chemical reactions; heat transfer and solid mechanics, and their interaction in the SOFC has lead to numerous numerical implementations and solutions of multi-physics models [1, 12, 36].

Adding up to its complexity the physical phenomena occur at different length scales, from electro-chemical reactions at sub-micron level at the triple-phase boundary, to flow in the gas channel at a macroscopic mm to cm level. A high spatial resolution of the entire SOFC including its microstructure would be required to obtain meaningful results. However, the resolution is limited by the available computer resources and it is impractical to use a detailed microstructure for an entire cell- or stack-simulation. Using a resolution of 1 µm for the calculations of an entire SOFC-stack (12 cm × 12 cm × 10 cm) would lead to approximately 1×10^{15} computational cells, which even exceeds the memory capacities of super computers.

A practical way to overcome this problem and still obtain meaningful results is to use homogenised models. In this approach the microstructure is considered to be pseudo-homogeneous with defined porous parameters, such as porosity, tortuosity, permeability, heat-, ionic-, electric-conductivity and so on [4]. The drawback of this approach is that these porous parameters have to be determined. This is straightforward for some, e.g. the porosity, but the evaluation of a permeability tensor requires more effort, not to mention the determination of the tortuosity which is an important parameter describing the diffusion through the microstructure. Additional parameters are used in the constitutive electro-chemistry models, namely the

Butler-Volmer equation and in Arrhenius' law. All in all, there are a couple of parameters that can't be exactly determined and are used as fitting parameters, which is a worrying situation having in mind John von Neumann's words:

> With four parameters I can fit an elephant, and with five I can make him wiggle his trunk.

Efforts must be undertaken to minimise the unknown parameters in order to improve the implemented models and obtain more meaningful results.

Two routes for the determination of mass-transport related parameters like porosity, tortuosity and permeabilities of the microstructure are available. Firstly, measurements of the cell based on electro-chemical impedance spectroscopy. Thereby, the impedance is measured while various operating parameters, like the temperature, fuel composition, current density etc., are varied [57]. An analysis of the distribution of relaxation times enables the separation of the individual loss mechanisms. It is therefore possible to obtain the contribution of the mass-transport to the overall Area-Specific Resistance (ASR). The fitting to an appropriate diffusion model will yield the values for the porosity and tortuosity. However, this approach depends on the possibility to discern the individual loss mechanisms and the ability to vary the operating parameters. This can be a delicate venture if the SOFC does not tolerate temperatures above 800 °C, as is the case with the current generation of metallic supported SOFC, due to limited stability of the anode.

Therefore, the second route is a viable alternative. Simulations are carried out on the reconstructed microstructure and homogenised parameters are determined, which describe the metallic support adequately. The microstructure can be measured either by Focused Ion Beam - Scanning Electron Microscopy (FIB-SEM) or X-ray computed tomography. Both methods offer the opportunity to obtain 3-D information of the porous electrode, which can be reconstructed and converted into a 3-D computational geometry, which incorporates the real microstructural features. More details on the two measurement techniques and the reconstruction are given in Chapter 4.

Various works have used this approach to analyse the microstructure and retrieve homogenised parameters for anode supported SOFC [33, 35, 40, 45, 46, 55, 94], but it was, to the author's knowledge, not yet applied to the porous metallic support. The basic approach to evaluate the effective diffusion coefficient, which is a measure for the diffusive mass-transport in the porous electrodes, is to apply symmetry boundary conditions for the lateral boundary (parallel to the main diffusion path) [33, 35, 45, 46, 94]. This is the easiest way to deal with the lateral boundaries, but also a problematic one. The symmetry boundary condition basically resembles a wall, which means that no mass-flux in or out of the geometry is possible trough the lateral walls which introduces a lot of dead-end pores.

The workaround to limit the influence of this unnatural boundary condition is to perform the simulations on a sufficiently large volume, so that the ratio between dead-end and continuous pores is small enough. However, a larger volume will lead to the need of more computing power and time to perform the simulation, and on inhomogeneous microstructures the required volume could easily exceed the available memory resources. It was shown that with increasing size of the investigated volume the evaluated parameters converge because of the diminishing influence of the lateral boundaries [46]. Nevertheless, the effects of different boundary conditions at the lateral walls were not discussed yet. So far only the effect of different boundary conditions on the top and bottom boundaries is discussed [55]. As Alan Mathison Turing, a computer pioneer, puts it:

> Science is a differential equation, religion is a boundary condition.

In this work the influence of different boundary conditions, namely the state-of-the-art symmetry and the periodic condition, is evaluated and compared to each other and measurement results, to lessen our need to *believe* in the choice of the boundary conditions. The periodic boundary condition couples boundary faces on opposite walls which overlap, and presumes that the sum of the mass-flow of both faces is zero. In other words, what leaves from one side enters on the other. This resembles also reality where the pores which are cut off deliberately by the computational volume will continue and are not blocked. It will be shown in this work that the

implementation of periodic boundary conditions will substantially improve the results of the computations, compared to the state-of-the-art approach.

The accuracy of all current microstructural models that are used to determine homogenised parameters depends on the quality of the reconstructed microstructure. During the operation degradation will affect the microstructure. This could be for example a volume expansion of the Ni-particles in a Ni-YSZ anode for the anode supported SOFC, or the oxide growth in the metallic supported SOFC due to corrosion. The latter case is part of this research.

In order to assess the impact of corrosion on the metallic support, experiments were carried out to determine the mass gain of potential substrate material [60–63]. However, it is difficult to draw conclusions from these measurements, as the local influence of the microstructure, e.g. blocking of pores, can hardly be assessed. In addition to that, long-term tests have to be carried out, which are normally time and cost consuming. It was up till now not possible to evaluate the influence of corrosion on the mass-transport in the metallic support, and the obtained results of the homogenised parameters were limited to the initial operating phase of the SOFC.

In this work, a basic corrosion model is presented to compute the change of the microstructure and determine its influence on the mass-transport. It is based on the theory of Wagner [96], who proposed a parabolic rate law based on corrosion measurements at high temperatures >500 °C, to describe the growth of the oxide layer. The basic assumption is that the diffusion of either metal- or oxide-ions through the oxide layer is the rate limiting step of the reaction. This proved to be true as long as the film thickness is sufficiently large and forms a continuous layer (e.g. >1 µm for temperatures above 500 °C) [3]. During the initial on-set of corrosion, till a continuous layer is formed, the reaction is faster and kinetics may show a linear behaviour [44]. A combination of linear followed by parabolic rate models will be used to describe the thickness increase of the oxide layer adequately.

Unlike other corrosion simulation works [37, 67, 75], where the thickness of the oxide is purely a boundary condition to compute the ion species distribution in the oxide layer, this work focuses on the volume change of the 3-D microstructure due to the growth of the oxide layer. The oxide

thickness is determined by applying first a linear and subsequently a parabolic rate law. The metal-retraction, which is a shrinkage of the alloy caused by the consumption of Cr-ions for the formation of the oxide, is determined by a mass balance following the procedure proposed in [37]. It is thus possible to effectively determine the volume change of the pores.

The results of the corrosion solver are coupled with the evaluation model of the transport parameters to determine, for the first time, the change of these parameters due to corrosion. This facilitates the estimation of the SOFC performance after longer operation times without time and cost consuming long-term test.

1.2 Publications

A 3-D microstructural code for solving a corrosion model and evaluating transport parameters is presented in this Thesis. Most of the models and the results have been and will be published in the following papers:

1. Georg Reiss, Henrik L. Frandsen, Wilhelm Brandstätter, André Weber. "Numerical evaluation of micro-structural parameters of porous supports in metal-supported solid oxide fuel cells". In: *Journal of Power Sources* 273. (7.10.2014), 1006-1015.

2. Georg Reiss, Henrik L. Frandsen, Christian Weiß, Wilhelm Brandstätter. "Numerical Evaluation of the Oxide Growth in Metal-supported Solid Oxide Fuel Cells and its Influence on Mass Transport". Submitted to: *Journal of Power Sources*.

1.3 Outline

A concise overview of the Thesis is as follows:

1. In *Chapter 1: Introduction* the context of the Thesis is explained. A short summary on state-of-the-art microstructural modelling to retrieve homogenised transport parameters

as well as on corrosion modelling is given.

2. *Chapter 2: SOFC in a minute* gives a brief introduction in the operation principal of SOFCs and explains the differences to metallic supported SOFCs.

3. *Chapter 3: Theoretical background* gives an overview about corrosion and mass-transport theory and models.

4. In *Chapter 4: Geometry reconstruction* measurement techniques are explained which can be utilised to obtain a three-dimensional information of the porous microstructure. The reconstruction algorithm for creating computational geometries is explained and the advantages and drawbacks of surface representation, as well as boundary conditions, are discussed.

5. *Chapter 5: Simulation and modelling* summarises and explains the implementation of the corrosion and the mass-transport model. Furthermore, the geometric analysis of the microstructure, as well as the determination of the permeability tensor of the metallic support, are described.

6. *Chapter 6: Validation* focuses on the validation of the proposed and developed models.

7. In *Chapter 7: Results* the potential of the corrosion and the evaluation model are demonstrated on a metallic support.

8. *Chapter 8: Conclusions* summarises the most important findings and gives a future outlook.

Chapter 2

SOFC in a minute

2.1 Basics and loss mechanisms

An SOFC is a device designed to convert chemical energy into electricity and heat. A schematic drawing of a single SOFC including its interconnects is shown in Figure 2.1. Unlike in power plants, the fuel is not combusted, but electro-oxidised at the anode by oxygen ions, which are transported from the cathode through the electrolyte. The most common fuel is hydrogen and the overall reaction at the anode is:

$$\mathrm{H_2(g) + O^{2-} \rightarrow H_2O(g) + 2}e^{-}. \tag{2.1}$$

The electrons move through an external circuit to the cathode where molecular oxygen (present in air) is reduced to oxide ions:

$$\frac{1}{2}\mathrm{O_2(g) + 2e^{-} \rightarrow O^{2-}}. \tag{2.2}$$

These reactions take place in the vicinity of the electrolyte at the so-called triple phase boundary (TPB), where the electrode (electronic phase), the electrolyte (ionic phase) and the gas phase (hydrogen, air) are in contact. However, in reality these reactions are more complex and stepwise in nature, including gas phase transport (convection and diffusion) from the gas flow in the gas channels to the porous electrodes; diffusion in porous media; species absorption, de-

sorption and dissociation; surface reaction; bulk exchange and charge transfer [58]. Depending on the operating conditions one of the above mentioned steps is rate limiting.

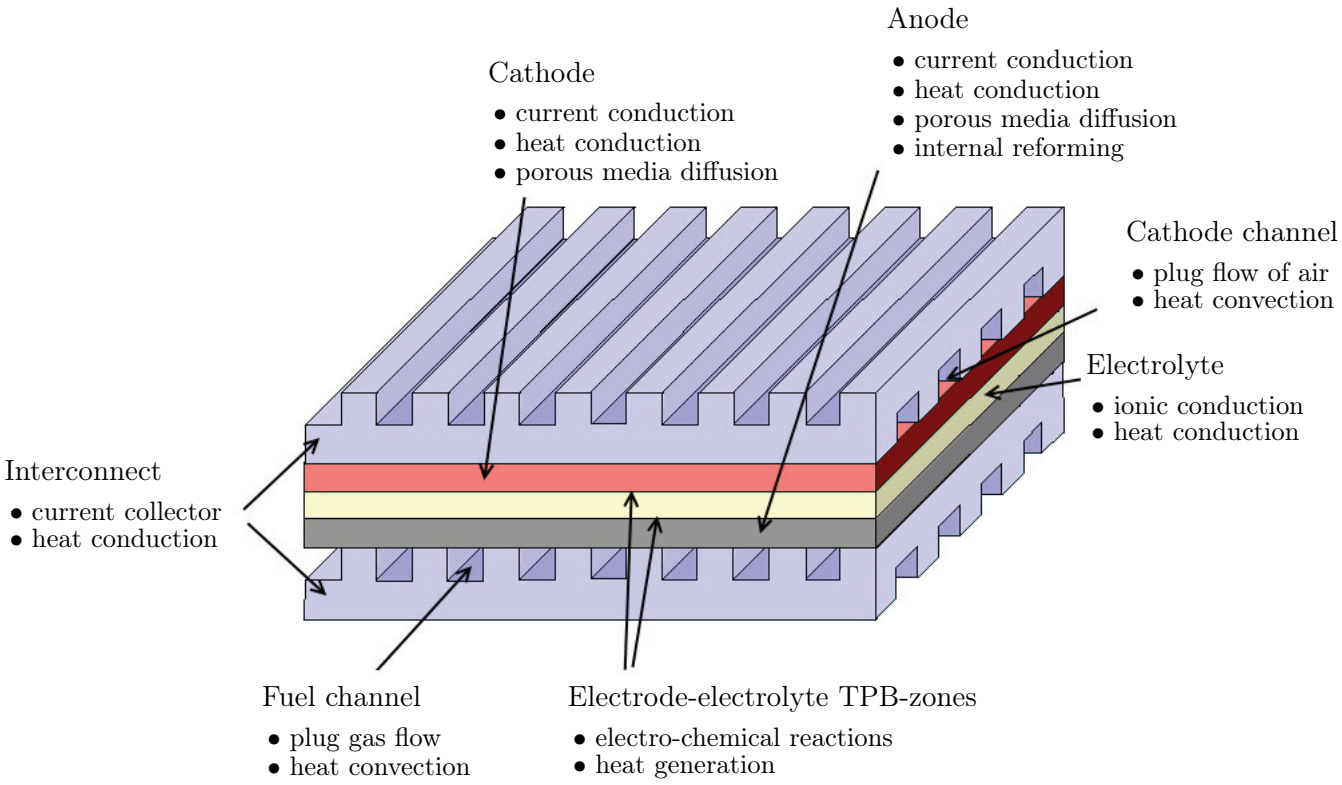

Figure 2.1: Principal sketch of the individual components of a single SOFC, including their functions (according to [58]).

The theoretical reversible E_{rev} or open circuit voltage (OCV) of a single SOFC operated with hydrogen and oxygen is 1.229 V at standard conditions (273.15 K, 1.033×10^5 Pa). It can be calculated by the Nernst equation [58]:

$$E_{rev}(p,T) = E^0(T^0,p^0) - \frac{RT}{2F} ln\left(\frac{x_{\mathrm{H_2O}}}{x_{\mathrm{H_2}}\sqrt{x_{\mathrm{O_2}}}}\right) + \frac{RT}{4F}\ln p, \tag{2.3}$$

where E^0 is the standard electrode potential, R the universal gas constant, T the temperature, F Faraday's constant, x the molar concentration and p the pressure. The actual measured OCV lies slightly below E_{rev}. This difference is denoted U_l which represents potential losses due to residual electronic conduction in the electrolyte and possible micro-cracks in the electrolyte which lead to a cross over of gases. When a current I is drawn from the SOFC the voltage

drops further [58]:

$$U_{cell} = E_{rev} - U_l - IR_{e,i} - (\eta_{act} + \eta_{conc}), \tag{2.4}$$

due to ohmic losses, where $R_{e,i}$ is the electronic and ionic resistance, η_{act} denotes the charge transfer or activation polarisation, and η_{conc} is the concentration polarisation. The individual mechanisms that cause the potential loss are summarised in more detail [18]:

1. *Activation polarisation*: This can be seen as an energy barrier which has to be overcome so that the reaction can start. It can be quantified by the well-known and widely used Butler-Volmer equation:

$$i = i_0 \left(\exp\left(\beta \frac{n_e F \eta_{act}}{RT} \right) - \exp\left(-(1-\beta) \frac{n_e F \eta_{act}}{RT} \right) \right), \tag{2.5}$$

   where i_0 is the exchange current density, β is the transfer coefficient, normally 0.5, and n_e is the number of electrons transferred per reaction.

2. *Ohmic polarisation*: These losses occur due to the resistance of the electrolyte for the ions and the electrode material for the electrons.

3. *Concentration polarisation*: Whenever a current is drawn the species concentration at the reaction site will be lower compared to the bulk concentration of the gas stream. This gas transport loss gets more significant at higher current densities, when more fuel is consumed. The diffusion through the porous anode can be a rate limiting step. Therefore, the diffusion through the microstructure will be investigated in this study. The resulting concentration over-potential at the anode side can be calculated by applying the Nernst equation [21]:

$$\eta_{\text{conc}} = \frac{RT}{2F} \ln \left(\frac{p_{\text{H}_2}^{\text{bulk}} p_{\text{H}_2\text{O}}^{\text{AFL}}}{p_{\text{H}_2\text{O}}^{\text{bulk}} p_{\text{H}_2}^{\text{AFL}}} \right), \tag{2.6}$$

   where p_i denotes the partial pressure of H_2 and H_2O at the gas-channel metallic support interface (bulk) and the metallic support anode functional layer interface (AFL).

Figure 2.2 summarises a typical voltage-current characteristic. At low current densities the activation polarisation is predominant. At higher values a linear relation between the current

density and the voltage can be seen, so it can be concluded that ohmic polarisation is prevailing. By increasing the current density further, the concentration polarisation gets higher and a steeper drop in the potential can be observed.

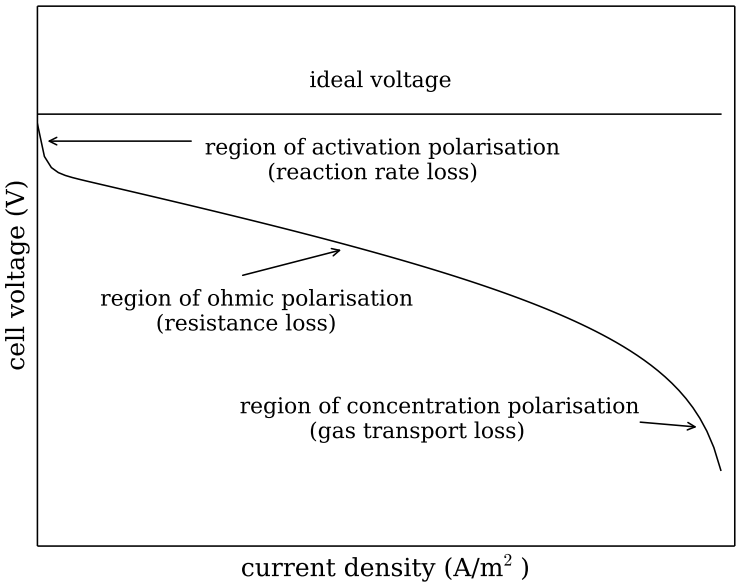

Figure 2.2: Ideal and actual fuel cell voltage-current characteristics according to [48].

2.2 Metallic supported SOFC

The state-of-the-art anode-supported SOFC consists entirely of ceramic, which is electrochemically active, although only in a small region, the triple-phase boundaries, reactions occur. Metallic supported SOFCs substitute the supporting ceramic material with a sintered metal powder and try to minimise the costs, with improved performance.

The porous metallic support, which is analysed in this study, is produced at the Technical University of Denmark (DTU). A comprehensive description of the entire cell can be found in [9], whilst the most important aspects are summarised here: The support is made by tape-casting, and the slurries contain Fe-Cr-powder (22 % Cr-based stainless steel alloy), organic solvent and additives required for the process.

In order to obtain an electro-chemical active region, Yttria-Stabilised Zirconia (YSZ) was added to the metal-powder to form a so-called cermet (ceramic+metal) layer, which will later be infiltrated. The electrolyte is produced using similar tape-casting techniques, where the powder is based on ZrO_2 co-doped with Sc_2O_3 and Y_2O_3. The individual tapes are dried and laminated together. Thereafter, the laminated half-cell is sintered above 1000 °C in reducing atmosphere (H_2/Ar). After the sintering process, the porous metallic support is infiltrated with $Ce_{0.8}Gd_{0.2}O_{1.9}$ (CGO20) + 10 wt.% Ni to form the electro-catalytic active phase, which acts as a fuel electrode. The final step is the screen-printing of the cathode (LSCF/CGO), as well as the cathode contact layer (LSC), and the subsequent in-situ firing during cell testing at a maximum temperature of 800 °C. A cross-sectional micro-graph of a half-cell after sintering without infiltration is shown in Figure 2.3.

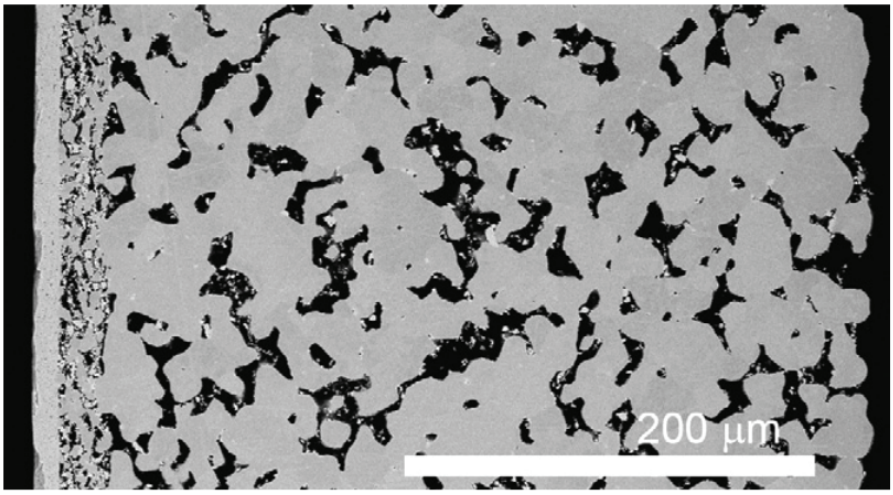

Figure 2.3: Cross-section of a sintered planar metallic supported half cell, without infiltration and screen-printed cathode. The dense electrolyte is shown to the left, followed by the cermet layer (anode) and the metallic support [9].

Chapter 3

Theoretical background

3.1 Corrosion

3.1.1 High-temperature corrosion theory

The porous metallic support of a metallic supported SOFC is prone to corrosion in the H_2-H_2O-atmosphere even at very low water-vapour partial pressures. The Richardson Ellingham diagram for the oxidation of metals is shown in Figure 3.1. It summarises the standard Gibbs free-energy change ΔG^0 versus the temperature for different metals and their oxides [44]. A lower ΔG^0 indicates an easier formation of the oxide. The equilibrium line in the diagram for Cr_2O_3 has a more negative ΔG^0 than Fe_2O_3, therefore the formation of Cr_2O_3 is the preferred reaction. Drawing a line (red) from the point H on the left-hand side of the diagram and intersecting it with the free-energy line for the formation of Cr_2O_3 at 650 °C yields a $^{H_2}/_{H_2O}$-ratio of $\approx 2 \times 10^5$, which would equal a water partial pressure of 5×10^{-6} at the equilibrium. A higher ratio (less water vapour) would reduce chromia to pure chromium; more water vapour will oxidise chromium. Consequently, at 650 °C a small amount of water vapour is sufficient to form a stable oxide.

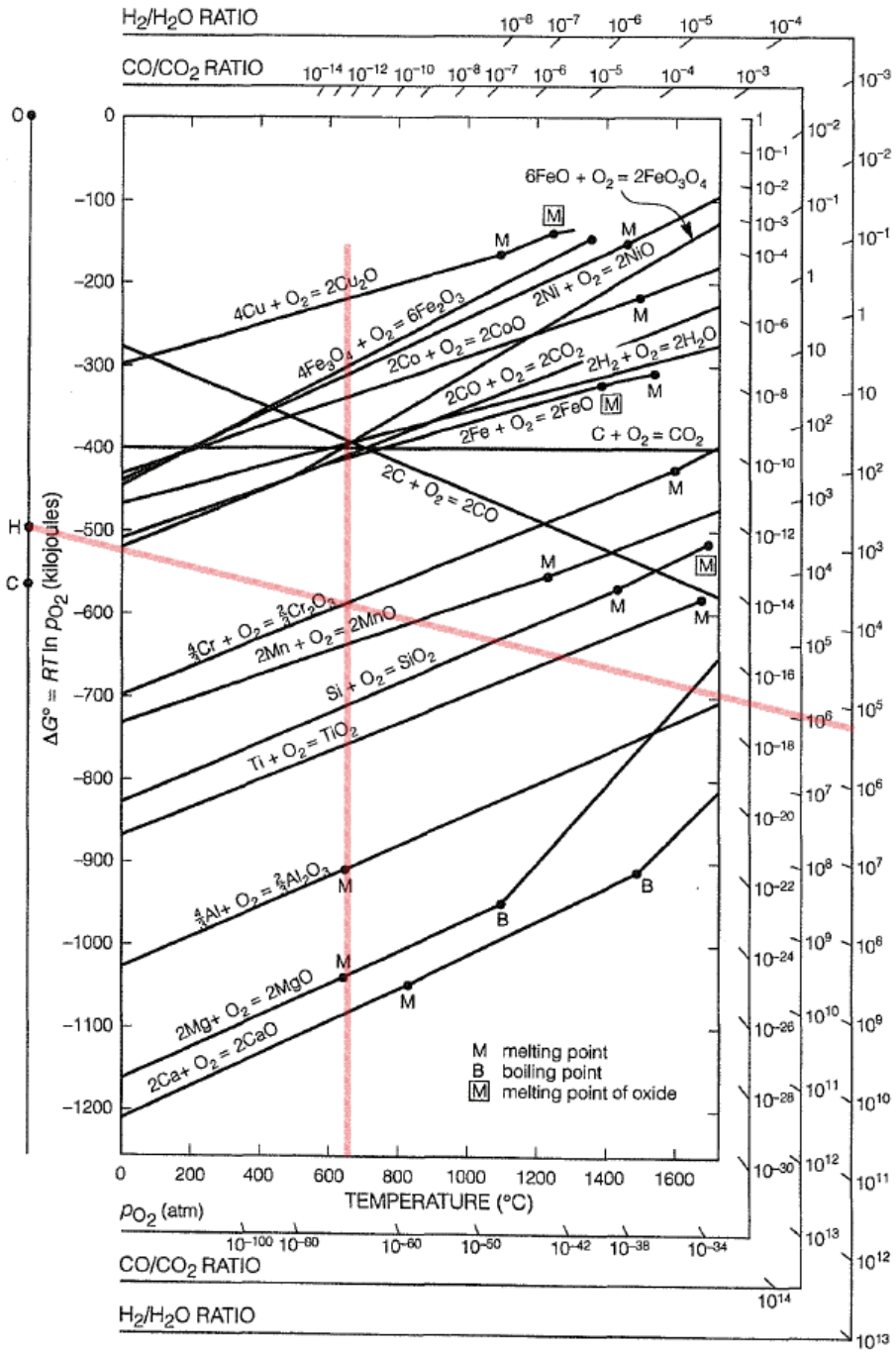

Figure 3.1: Richardson Ellingham diagram of free energy versus temperature for oxidation of metals [44]

The actual corrosion process comprises various reactions [44], which are depicted in a simplified way in Figure 3.2. In the beginning of the reaction the oxidant is adsorbed at the metal surface (Figure 3.2(a)). It reacts with the metal and forms an oxide which grows lateral, till a continuous layer is formed (Figure 3.2(b)). Thereafter, the oxide film becomes thicker and the gas or the metal ions have to diffusive through the oxide layer to form more oxide (Figure 3.2(c)), for which reason the further corrosion process slows down. Depending on the oxide and the surrounding

conditions the oxide layers can have cavities and cracks, which will lead to a faster corrosion process compared to continuous layers. (Figures 3.2(d) and (e)).

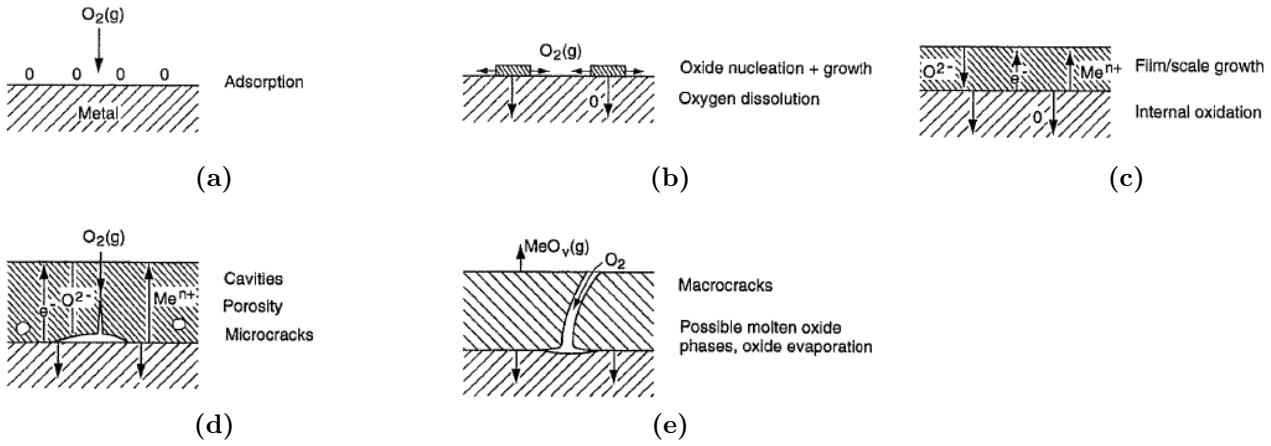

Figure 3.2: Formation of an oxide film during high-temperature metal oxidation [44].

In general the oxidation of a metal M to its oxide reads:

$$x\mathrm{M} + y\mathrm{H_2O} \rightarrow \mathrm{M}_x\mathrm{O}_y + y\mathrm{H_2}. \tag{3.1}$$

This chemical reaction will take place in the beginning of the corrosion, when the gas and the metal surface can interact directly (Figure 3.2(a) and (b)). As soon as continuous oxide layer is formed, the following electro-chemical reactions occur:

$$\mathrm{M} \rightarrow \mathrm{M}^{2+} + 2\mathrm{e}^-, \tag{3.2}$$

where the liberated pair of electrons migrates through the oxide and reduce oxygen:

$$\frac{1}{2}\mathrm{O_2} + 2\mathrm{e}^- \rightarrow \mathrm{O}^{2-}. \tag{3.3}$$

The migration of the electrons and the ions depends on the formed oxide and the concentration of the dominant oxide defects [44]:

1. *cation interstitials* (Figure 3.3a): The metal cations are liberated at the metal-oxide interface and move between the lattice positions of the cations and anions to the oxide-

gas interface, where the oxide is formed.

2. *anion vacancies* (Figure 3.3b): The O^{2-} anions migrate from the oxide-gas interface through the oxide lattice by changing place with anion vacancies to the metal-oxide interface, where they react with metal-ions and form the oxide.

3. *cation vacancies* (Figure 3.3c): Here, the metal cations move from the metal-oxide to the oxide-gas interface through cation vacancies, where the oxide is formed.

An elaborate summary of the basic theory of high-temperature corrosion is presented in [3]. The growth of the oxide film can be described with the following models, which depend on the thickness of the film: The theory of thick films developed by Wagner [96] and the theory of thin films by Cabrera and Mott [15]. Wagner's model is based on many measurements and observations from corrosion experiments that show parabolic weight gain, where the square of the film thickness x_{corr} is proportional to time t:

$$x_{corr}^2 = k_p t. \tag{3.4}$$

k_p is the parabolic rate constant. The basic assumption is that the diffusion across the film is the slowest, and therefore the rate-limiting step of all reactions. This diffusion flux through a compact and perfectly adherent oxide film is proportional to the concentration difference Δc across the film thickness x_{corr}. The steady-state flux with a constant ionic diffusivity D is proportional to the rate of scale thickening $\frac{\mathrm{d}x_{corr}}{\mathrm{d}t}$:

$$\frac{\mathrm{d}x_{corr}}{\mathrm{d}t} = CD\frac{\Delta c}{x_{corr}}, \tag{3.5}$$

where C is a proportionality constant [44]. The integration of Equation (3.5) with $x_{corr} = 0$ at $t = 0$ yields Equation (3.4), where $k_p = CD\Delta c$. Thus, the parabolic rate constant k_p is direct proportional to the ionic diffusivity D and Equation (3.5) can be reformulated to:

$$\frac{\mathrm{d}x_{corr}}{\mathrm{d}t} = \frac{k_p}{2x_{corr}}. \tag{3.6}$$

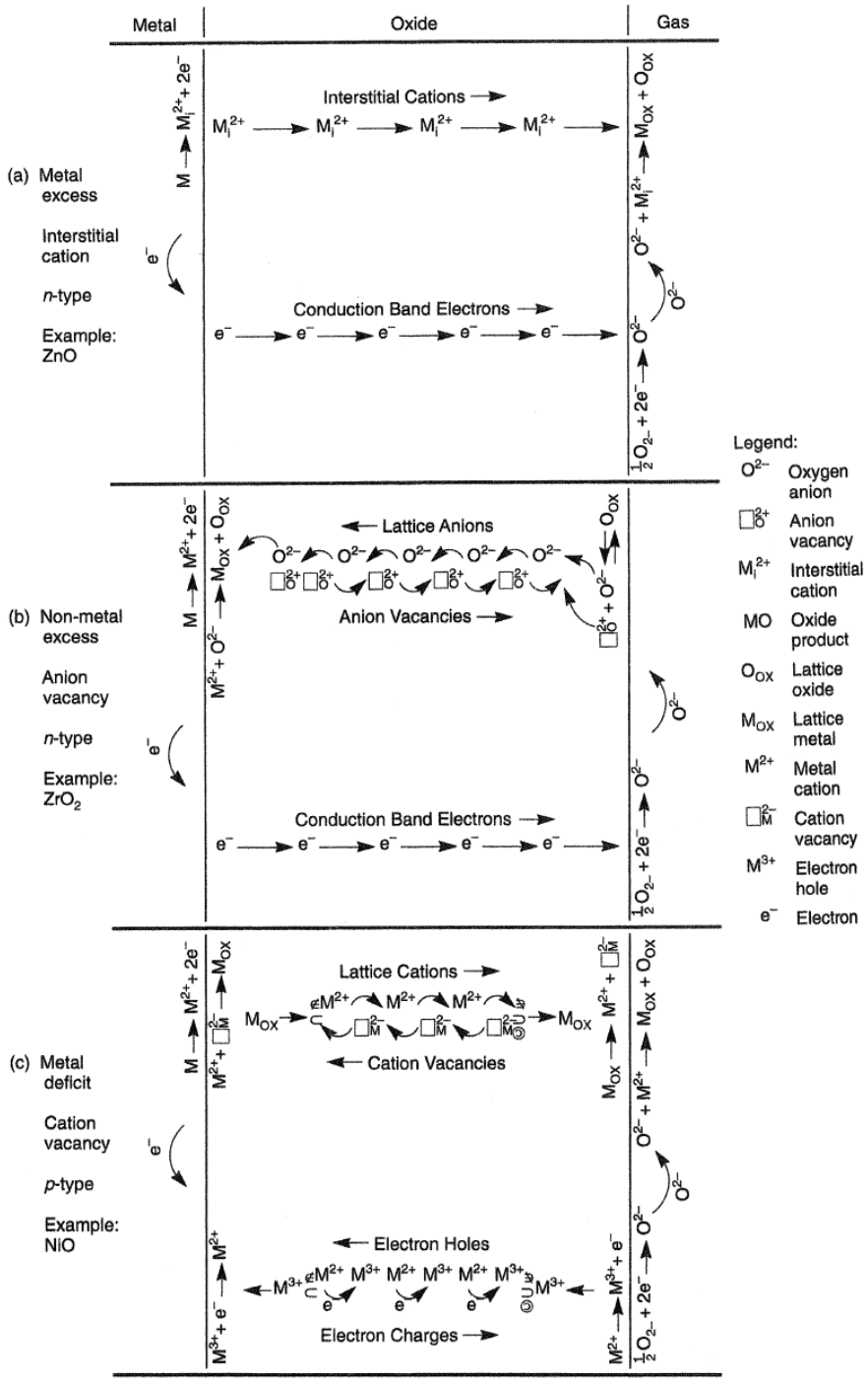

Figure 3.3: Processes occurring in three types of oxide surface scale during high-temperature oxidation [44].

Wagner's model is accepted to be valid for films thicker than 1 µm. This limit comes from the consideration that the electric field across the oxide, which is caused by ambipolar diffusion of the positive and/or negative ions and electrons, has to be sufficiently small so that the Nernst-Einstein relationship is still valid [3]. (The Nernst-Einstein equation relates the limiting ionic conductivity to the ionic diffusion coefficient.)

In thinner films the large electric field can cause atom jumps from the metal in the oxide and Cabrera and Mott were able to show that the oxidation rate decreases exponentially as film thickness increases, which leads to an inverse logarithmic law [3]:

$$\frac{\mathrm{d}x_{corr}}{\mathrm{d}t} = \frac{D}{a}\exp\left(\frac{X_1}{x_{corr}}\right), \tag{3.7}$$

where D has the dimensions of a diffusion coefficient, a is the ionic jump distance and X_1 is equal to the upper limit of thickness defined in the basic assumptions.

The validity of both, thin and thick film theories is depicted in Figure 3.4. Very thin oxide films <20 nm are described with the theory by Cabrera and Mott, while films thicker than the Debye length L_D, a limit where the Nernst-Einstein equation is valid, can be calculated by Wagner's theory.

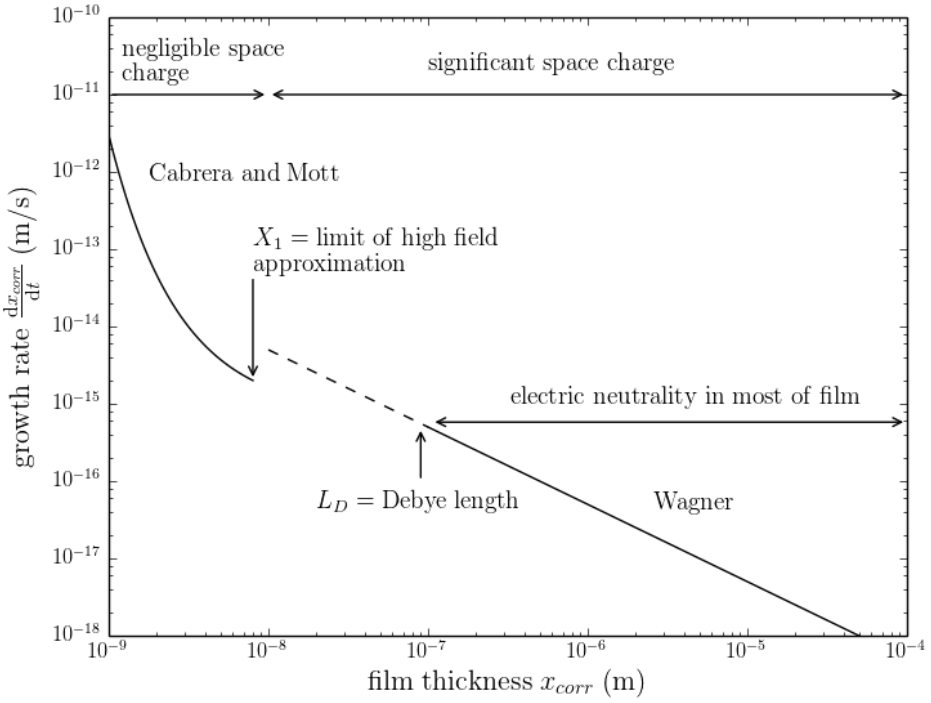

Figure 3.4: Growth rate of an oxide film as a function of its thickness, calculated with the theory of Cabrera and Mott when thin ($x_{corr} < X_1$) and of Wagner when thick ($x_{corr} > L_D$). The parameters used are appropriate to a film of NiO growing by lattice diffusion at 500 °C according to [3].

The dotted line between the two basic theories is considered as a transition regime and is adequately discussed in [99], where the kinetics where found to be describable by a direct

logarithmic rate law:

$$\ln\left(\frac{\mathrm{d}x_{corr}}{\mathrm{d}t}\right) = B_1 - B_2 x_{corr}, \tag{3.8}$$

where B_1 and B_2 are constants. Nevertheless, logarithmic behaviour is mainly observed for lower temperatures (<400 °C), while at higher temperatures linear reaction kinetics for thin films are prevailing:

$$\frac{\mathrm{d}x_{corr}}{\mathrm{d}t} = k_l, \tag{3.9}$$

where k_l is the linear rate constant. This means that in this early stages of corrosion the film is non protective and the chemical reaction is the rate limiting step. As the film thickens the kinetics can turn into a parabolic growth [44].

The consumption of Cr-ions for the formation of the oxide results in a shrinkage of the alloy, which can be estimated by the Pilling-Bedworth ratio, normally used to determine the protectiveness of the oxide [44]:

$$\mathrm{PB_{ratio}} = \frac{\text{volume of oxide produced}}{\text{volume of metal consumed}} = \frac{M_{ox}\rho_m}{z\rho_{ox}M_m}. \tag{3.10}$$

M_{ox} is the molecular weight and ρ_{ox} the density of the oxide, while M_m and ρ_m are the atomic weight and density of the pure metal, and z is the number of metal atoms in the oxide molecule. The Pilling-Bedworth ratio is 2.02 for chromium, which means that the volume of the oxide is twice as large as the volume of the metal, or in other words: When the oxide growths 1 µm the metal retracts by ~ 0.5 µm.

A procedure to calculate the metal-retraction r is proposed in [37]. The flux j_{ox} of the least noble element, required for the growth of the oxide $\Delta x_{corr}^{t\to t+\Delta t}$ during a time step Δt, is defined by:

$$j_{ox} = \frac{z_{ox}\rho_{ox}}{M_{ox}} \frac{\Delta x_{corr}^{t\to t+\Delta t}}{\Delta t}. \tag{3.11}$$

The corresponding metal-retraction of the source faces $\Delta r^{t\to t+\Delta t}$ can be calculated:

$$\Delta r^{t\to t+\Delta t} = -V_m j_{ox} \Delta t, \tag{3.12}$$

where V_m is the partial molar volume of the out-diffusing species. With the knowledge of the oxide thickness and the retraction of the metal-oxide-interface the change of the porous volume can be determined, which will be described in Chapter 5.1.

3.1.2 Weight-gain measurement

Having dealt with the basic theoretical principles of corrosion, we now want to see how this knowledge can be used to assess the applicability of metals in SOFCs. One way is to conduct corrosion experiments [60–63]. Hereby, potential Fe-Cr-powders are compacted at pressures in the range from 400 kPa to 600 kPa. The subsequent sintering is done in pure hydrogen at temperatures ranging from 800 °C to 1200 °C. The samples undergo thermogravimetric measurements as they corrode at different temperatures and water vapour content.

One problem addressed in [62] is the question how to relate the measured mass gain Δm to a surface A. The parabolic rate law Equation (3.4) would then read:

$$\left(\frac{\Delta m}{A}\right)^2 = k_{p,m}t. \tag{3.13}$$

Sometimes the apparent area of the sample is used, but the actual surface area might be different depending on the porosity, which makes a comparison quite difficult. Another approach is to use a relative weight gain $\Delta m/m_{init}$ related to the initial weight m_{init} of the sample. However, this is not satisfactory as better alternatives are available: The actual surface area can be determined by BET-measurements (named after the founders of the theory Stephen Brunauer, Paul Hugh Emmett and Edward Teller).

Once the parabolic rate constant $k_{p,m}$ ($\mathrm{kg^2\,m^{-4}\,s^{-1}}$) for the weight-gain is determined, it has to be converted to the parabolic rate constant k_p ($\mathrm{m^2\,s^{-1}}$), which describes the growth of the thickness. Therefore the density of the oxide ρ_{ox} is used:

$$k_p = \frac{k_{p,m}}{\rho_{ox}^2}. \tag{3.14}$$

The sintered metallic supports analysed in this study were measured by Åsa Persson at DTU. The surface area was determined with BET-measurements prior to the weight-gain measurements. The sintered specimen were cut to 10 mm × 10 mm samples, which were cleaned in acetone and ethanol. The experiments were conducted in a furnace at three different temperatures normally used in SOFC applications, namely 650 °C, 750 °C and 850 °C (850 °C being used for accelerated corrosion). The anode gas should simulate a high fuel utilisation and consisted of an $Ar/H_2/H_2O$-atmosphere with a p_{H_2O}/p_{H_2}-ratio of 9. This was achieved by mixing pure Ar with H_2-gas, which was flown through a water bottle.

The samples were heated up and cooled down with a ramp of 120 °C h^{-1}. They were kept at a constant temperature for 250 h, before the samples were cooled down and weighted. These oxidation cycles were repeated for up to 3000 h. Unfortunately, due to the long measurement intervals, it was not possible to describe the initial linear corrosion regime adequately. Therefore, lacking better information the first 300 h were considered to follow linear kinetics.

All the above mentioned studies evaluate and assess the applicability of potential Fe-Cr-powders by comparing their weight gain. This will be sufficient for a rough guess and a first go or no-go decision. Moreover, the measurements are limited to some hundreds to thousand hours, while the desired life-time of SOFCs is above 40.000 h. Long-term tests require a lot of resources and time. For these reasons it is desirable to break new ground and develop simulation tools, which are capable of using the information gained from corrosion experiments in models to describe the change of the microstructure adequately, and allow an estimation of the degradation caused by the corrosion.

3.2 Mass-transport

The gaseous mass-transport in the SOFC can be divided in a convective part, which is predominant in the gas-channels, and a mixture of a convective and diffusive transport in the electrodes. Due to the dense microstructure the diffusive mass-transport is predominant in the electrodes.

3.2.1 Convective flow and permeability

Darcy was the first to introduce an empirical law in 1856 [22] to describe a linear relationship between specific discharge q (the volume flow rate Q divided by the area $q = \frac{Q}{A}$) and the pressure drop $\frac{\Delta p}{\Delta l}$ [4] for flows in porous media:

$$q \sim \frac{\Delta p}{\Delta l}. \tag{3.15}$$

It is assumed in theory that the *inertial forces* $\boldsymbol{\nabla} \cdot \rho(\boldsymbol{u}\boldsymbol{u})$ in the creeping flow regime (low Reynolds numbers) are negligible compared to the *viscous forces*, and the steady-state Navier-Stokes equation

$$\rho \frac{\partial \boldsymbol{u}}{\partial t} + (\rho \boldsymbol{u} \cdot \nabla)\, \boldsymbol{u} = -\nabla p + \mu \triangle \boldsymbol{u} + (\lambda + \mu)\, \nabla\, (\nabla \cdot \boldsymbol{u}) + \boldsymbol{f}, \tag{3.16}$$

reduces to a linear relationship between the pressure and the velocity [13]:

$$\nabla p = \mu \nabla^2 \boldsymbol{u}. \tag{3.17}$$

In the above equations the density of the fluid is denoted ρ, μ is the dynamic viscosity, λ the first Lamé constant defined as $\lambda = -\frac{2}{3}\mu$ and $\boldsymbol{f}$ stands for various volume forces such as gravity.
Thus Equations (3.18) and (3.17) can be written in scalar form:

$$q = \frac{k}{\mu} \frac{\Delta p}{\Delta l} \tag{3.18}$$

The permeability k is an important parameter to describe the flow in the microstructure on a macroscopic level. A lower and upper limit for the applicability of Darcy's law is reported in [4]. It is argued that the lower limit results from the necessity of a minimum gradient, below which no flow is to be expected. The upper limit was found by experiments where the results of the measured pressure drop at given velocities deviate from the linear relationship reported in Equation (3.18). Darcy's law is only valid at low Reynolds numbers ($\mathrm{Re} < 1 - 10$), where

the flow is laminar and the viscous forces are predominant. But the applicability of Darcy's law is also reported to be Re $\ll 1$ [64].

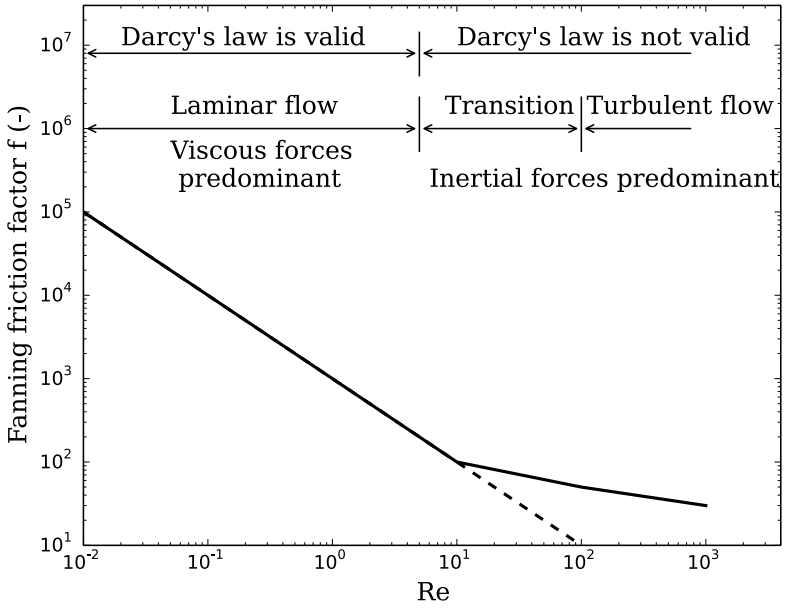

Figure 3.5: Schematic classification of flow through porous media according to [4]

.

At higher Reynolds numbers the *inertial forces* become more dominant (see Figure 3.5). For these cases Forchheimer [27] suggested a non-linear relationship between the pressure gradient and the superficial velocity more than hundred years ago. His one-dimensional motion equation takes the form:

$$\Delta p = a_1 U_x + a_2 U_x^2, \tag{3.19}$$

where the pressure drop is proportional to the superficial velocities [4]. The first term on the right-hand side attributes the linear Darcy effects at low velocities, wherein the factor $a_1 = \frac{\mu \Delta l}{k}$. The second term accounts for the non-linear nature as soon as the inertial forces became predominant. These inertial forces are proportional to the square of the velocity and the factor $a_2 = \frac{\rho \Delta l}{s}$, where s is the scalar Forchheimer term accounting for non-linear pressure drop. A schematic relationship between the superficial velocity and the pressure drop is depicted in Figure 3.6. While Darcy's law only predicts a linear pressure increase with higher velocities, the Forchheimer model also accounts for non-linear effects. The Forchheimer model is a rather simple model, but by far not the only one. Other models are presented and in discussed in [4].

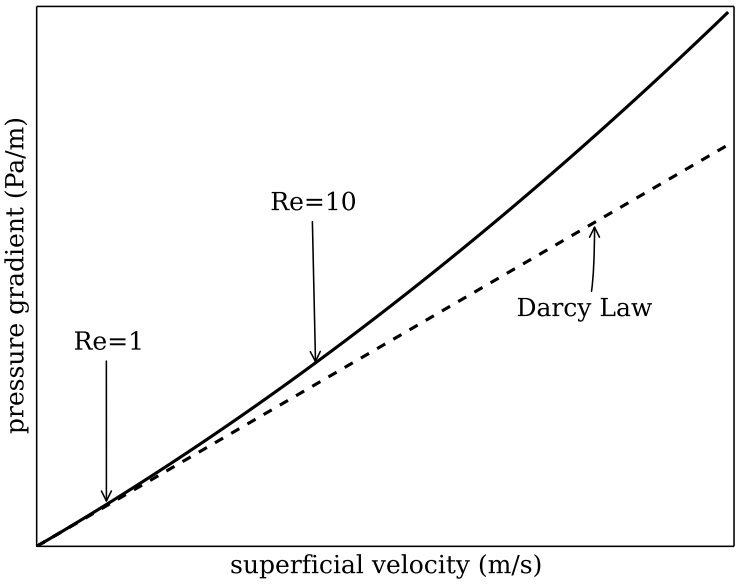

Figure 3.6: Schematic representation of experimental relationship between the superficial velocity and the pressure gradient according to [4].

The experimentally established law by Darcy for a homogeneous, incompressible fluid was limited to one-dimensional flow. The extension of Equation (3.18) to three-dimensional flow in anisotropic media has the form [4]:

$$\langle \boldsymbol{u} \rangle = \frac{\boldsymbol{k}_{ij}}{\mu} \nabla p, \tag{3.20}$$

where $\langle \boldsymbol{u} \rangle$ is the bulk-volume average velocity, ∇p the pressure gradient, $\boldsymbol{k}_{ij}$ being the permeability tensor and μ the dynamic viscosity. This extension was proved to be mathematically correct and it was found that the permeability tensor $\boldsymbol{k}_{ij}$ is a symmetric second order tensor ($k_{xy} = k_{yx}, k_{xz} = k_{zx}, k_{yz} = k_{zy}$) [66]. Thus Equation (3.20) reads:

$$\begin{pmatrix} \langle u_x \rangle \\ \langle u_y \rangle \\ \langle u_z \rangle \end{pmatrix} = \frac{1}{\mu} \begin{pmatrix} k_{xx} & k_{xy} & k_{xz} \\ k_{yx} & k_{yy} & k_{yz} \\ k_{zx} & k_{zy} & k_{zz} \end{pmatrix} \begin{pmatrix} \frac{\partial p}{\partial x} \\ \frac{\partial p}{\partial y} \\ \frac{\partial p}{\partial z} \end{pmatrix} \tag{3.21}$$

One-dimensional permeability can be measured in laboratory either by applying a fixed pressure and determining the flow rate through the sample, or by applying a fixed flow rate and

determining the pressure drop [4]. The flow medium can be a liquid or a gas, although it was found after comparing many experimental data of different materials that the permeability of one and the same material varies, depending whether the fluid was an incompressible liquid or a compressible gas.

The air permeability tends to be higher than the liquid permeability in the same porous media. The reason is that Darcy's law is based on laminar flow theory, where a zero fluid velocity is assumed at the solid wall. This is only true for liquids, while gas molecules are interacting with the solid wall in form of collisions, especially when the mean free path of the gas molecules approaches the dimensions of the pores. This flow is known as *Knudsen flow* [4]. Klinkenberg [51] derived the following relationship for the permeabilities of gases and liquids:

$$k_g = k_l\Big(1 + 4c\frac{\lambda}{r}\Big), \tag{3.22}$$

where k_g is the permeability of the gas, k_l is the permeability of the liquid, λ is the mean free path of the gas molecules, $c \sim 1$ is a proportionality factor and r is the radius of the capillary tubes in Klinkenberg's model. Additional models are reviewed in [79].

Recent benchmark studies [2, 93] describe the experimental determination not only of the 1-D permeability but of the entire permeability tensor in textiles. The basic experimental set-up can be distinguished by three main criteria:

1. flow geometry (linear, radial),
2. injection boundary condition (constant pressure, constant flow rate),
3. saturation of the specimen (saturated/unsaturated).

In these experiments the position of the flow front of the liquid is tracked and used to determine the permeability tensor. However, the principal directions of the permeability tensor have to be known, otherwise more experiments in different directions are needed, or the pressure gradient has to be measured simultaneously in different directions [2]. If the principal directions of the

permeability are unknown, as this would be the case in the metallic support microstructure, six independent experiments would be required to derive all six components of the symmetric permeability tensor [4].

Another way to determine the permeability tensor is to use the actual microstructures obtained by measurements (see Chapter 4) and simulate the flow through the pores. This procedure is used in this work and is described in more detail in Chapter 5.3.1.

3.2.2 Diffusion modelling

The microstructure of SOFCs is normally rather dense with a very low permeability, and mass-transport is mainly based on diffusion. The species conservation equation for a species i reads:

$$\frac{\partial(\rho w_i)}{\partial t} + \nabla \cdot (\rho w_i \boldsymbol{u}) + \nabla \cdot \boldsymbol{j}_i = s_{w_i}, \tag{3.23}$$

where ρ is the density of the gas, w_i is the mass fraction of species i, $\boldsymbol{u}$ is the mass averaged velocity, which is also used in the momentum conservation and continuity equations, $\boldsymbol{j}_i$ is the mass diffusion flux of species i relative to the mass averaged velocity and s_{w_i} is the mass source or sink of the species i.

Here an important term, the mass averaged velocity, needs a more thorough explanation, as this may lead to some confusion in the definitions of diffusion modelling. A detailed overview of different reference frames and diffusion fluxes is given in [86]: Each species i in a gas has its own velocity $\boldsymbol{v}_i$, with respect to a stationary coordinate reference frame. Then its mass flux $\boldsymbol{n}_i$ can be defined as:

$$\boldsymbol{n}_i = \rho_i \boldsymbol{v}_i, \tag{3.24}$$

with ρ_i as the mass density of species i. The sum over all species yields the entire mass flux $\boldsymbol{n}_t$:

$$\boldsymbol{n}_t = \sum_{i=1}^{n} \boldsymbol{n}_i = \rho \boldsymbol{u}, \tag{3.25}$$

where the mass averaged velocity $\boldsymbol{u}$ is defined as:

$$\boldsymbol{u} = \sum_{i=1}^{n} w_i \boldsymbol{v}_i. \tag{3.26}$$

As it is sometimes more convenient to use a molar reference frame, Equation (3.23) can be re-formulated with a molar averaged velocity $\boldsymbol{U}$:

$$\frac{\partial(cx_i)}{\partial t} + \nabla \cdot (cx_i \boldsymbol{U}) + \nabla \cdot \boldsymbol{J}_i = S_{x_i}, \tag{3.27}$$

where c is the mixture molar density, x_i is the mole fraction and $\boldsymbol{J}_i$ is the molar flux of species i. Similar definitions as before can be made for the species molar flux $\boldsymbol{N}_i$:

$$\boldsymbol{N}_i = c_i \boldsymbol{v}_i, \tag{3.28}$$

with c_i being the molar density of species i. The entire molar flux $\boldsymbol{N}_t$ is again the sum over all species molar fluxes:

$$\boldsymbol{N}_t = \sum_{i=1}^{n} \boldsymbol{N}_i = c\boldsymbol{U}, \tag{3.29}$$

where the molar averaged velocity $\boldsymbol{U}$ is defined as:

$$\boldsymbol{U} = \sum_{i=1}^{n} x_i \boldsymbol{v}_i. \tag{3.30}$$

Various definitions have been introduced which are needed to describe diffusion processes. Nevertheless, there is more to define because in the species conservation equations (3.23) and (3.27) the mass diffusion flux $\boldsymbol{j}_i$ or the molar diffusion flux $\boldsymbol{J}_i$ are needed. These fluxes are defined relative to the flux of the mixture. And *that's when your headache begins*, based loosely on Elvis, because the first question to answer is which mixture velocity should be used. And for each reference velocity there are at least two diffusion fluxes which can be defined, mass and molar fluxes. If the mass averaged velocity $\boldsymbol{u}$ is chosen as reference velocity, the mass diffusion flux reads:

$$\boldsymbol{j}_i = \rho_i(\boldsymbol{v}_i - \boldsymbol{u}), \tag{3.31}$$

with the constraint that the sum of the diffusion mass fluxes is zero:

$$\sum_{i=1}^{n} \boldsymbol{j}_i = \mathbf{0}. \tag{3.32}$$

The total mass flux $\boldsymbol{n}_t$ and the mass diffusion flux are related as follows:

$$\boldsymbol{n}_i = \boldsymbol{j}_i + \rho_i \boldsymbol{u} = \boldsymbol{j}_i + w_i \boldsymbol{n}_t. \tag{3.33}$$

The same holds true if the molar averaged velocity $\boldsymbol{U}$ is chosen as reference velocity:

$$\boldsymbol{J}_i = c_i(\boldsymbol{v}_i - \boldsymbol{U}), \tag{3.34}$$

again with

$$\sum_{i=1}^{n} \boldsymbol{J}_i = \mathbf{0}. \tag{3.35}$$

The total molar flux $\boldsymbol{N}_t$ is related to the molar diffusion flux by:

$$\boldsymbol{N}_i = \boldsymbol{J}_i + c_i \boldsymbol{U} = \boldsymbol{J}_i + x_i \boldsymbol{N}_t. \tag{3.36}$$

It is possible to convert the diffusion fluxes from one reference frame to another. For example the transformation of the mass diffusion flux $\boldsymbol{j}_i$ relative to the mass averaged velocity $\boldsymbol{u}$ to the mass diffusion flux $\boldsymbol{j}_i^U$ relative to the molar averaged velocity $\boldsymbol{U}$ is defined by [86]:

$$\boldsymbol{j}_i^U = \sum_{k=1}^{n-1} B_{ik}^{uo} \boldsymbol{j}_k, \tag{3.37}$$

where the coefficients of B_{ik}^{uo} are given by:

$$B_{ik}^{uo} = \delta_{ik} - w_i\left(\frac{x_k}{w_k} - \frac{x_n}{w_n}\right). \tag{3.38}$$

The inverse transformation is defined as:

$$\boldsymbol{j}_i = \sum_{k=1}^{n-1} B_{ik}^{ou} \boldsymbol{j}_k^U , \tag{3.39}$$

with B_{ik}^{ou}:

$$B_{ik}^{ou} = \delta_{ik} - w_i\big(1 - \frac{w_n x_k}{x_n w_k}\big). \tag{3.40}$$

Table 3.1 summarises common reference velocities together with the definition of the diffusion fluxes and the corresponding constraints.

Table 3.1: Diffusion fluxes and constraints [86]

$\boldsymbol{j}_i^a$	Mass diffusion flux relative to an arbitrary reference velocity	
	$\boldsymbol{j}_i^a = \rho_i(\boldsymbol{v}_i - \boldsymbol{u^a})$	$\sum_{i=1}^n \frac{a_i}{w_i}\boldsymbol{j}_i^a = \boldsymbol{0}$
$\boldsymbol{j}_i$	Mass diffusion flux relative to mass averaged velocity	
	$\boldsymbol{j}_i = \rho_i(\boldsymbol{v}_i - \boldsymbol{u})$	$\sum_{i=1}^n \boldsymbol{j}_i = \boldsymbol{0}$
$\boldsymbol{j}_i^U$	Mass diffusion flux relative to molar averaged velocity	
	$\boldsymbol{j}_i^U = \rho_i(\boldsymbol{v}_i - \boldsymbol{U})$	$\sum_{i=1}^n \frac{x_i}{w_i}\boldsymbol{j}_i^U = \boldsymbol{0}$
$\boldsymbol{J}_i^a$	Molar diffusion flux relative to an arbitrary reference velocity	
	$\boldsymbol{J}_i^a = c_i(\boldsymbol{v}_i - \boldsymbol{u^a})$	$\sum_{i=1}^n \frac{a_i}{x_i}\boldsymbol{J}_i^a = \boldsymbol{0}$
$\boldsymbol{J}_i$	Molar diffusion flux relative to molar averaged velocity	
	$\boldsymbol{J}_i = c_i(\boldsymbol{v}_i - \boldsymbol{U})$	$\sum_{i=1}^n \boldsymbol{J}_i = \boldsymbol{0}$
$\boldsymbol{J}_i^u$	Molar diffusion flux relative to mass averaged velocity	
	$\boldsymbol{J}_i^u = c_i(\boldsymbol{v}_i - \boldsymbol{u})$	$\sum_{i=1}^n \frac{w_i}{x_i}\boldsymbol{J}_i^u = \boldsymbol{0}$

Why to bother with different reference velocities? The answer is that under certain conditions either the mass or the molar averaged velocity is zero and Equations (3.23) and (3.27) simplify. As an example, this is the case in an anode of the SOFC where an H_2-H_2O-fuel mixture is used. An equimolar counter-diffusion takes place where for each hydrogen molecule that diffuses from

the gas-channel to the anode-functional-layer, one water molecule is formed and diffuses back $\boldsymbol{N}_{H_2O} = -\boldsymbol{N}_{H_2}$. This results in a zero entire molar flux and thus also the molar averaged velocity has to be zero:

$$\boldsymbol{N} = \sum_{i=1}^{n} \boldsymbol{N}_i = c_t \boldsymbol{U} = \boldsymbol{0}. \tag{3.41}$$

However, this does not mean that the mass averaged velocity $\boldsymbol{u}$ is zero as well. In the case of a H_2-H_2O-fuel mixture the ratio of the molecular weight of water and hydrogen is 9. This means that for each water molecule which diffuses from the anode-functional-layer to the gas-channel, 9 hydrogen molecules would have to diffuse in the opposite direction to satisfy the diffusion constraint in Equation (3.32), which would increase the driving force of the hydrogen diffusion.

This effect is balanced by a mass averaged velocity from the anode functional layer which transports the water vapour to the gas-channel. The result of this is a pressure gradient in the microstructure which has a significant influence on the results, when the Maxwell-Stefan model (see Chapter 3.2.2.2) is applied, where the pressure gradient is part of the driving force. The differences and the influence on the concentration over-potential will be shown in Figure 6.13 in Chapter 6.2.

3.2.2.1 Fick model

The species conservation equations (3.23) and (3.27) contain the mass and molar diffusion fluxes. It is hard to determine the species velocity $\boldsymbol{v}_i$ by measurements, for which reason constitutive laws are needed to model these diffusion fluxes. Fick was one who provided an empirical law to relate the diffusion fluxes to concentration gradients [86]:

$$\boldsymbol{j}_i = -\rho \mathscr{D}_{ij} \nabla w_i. \tag{3.42}$$

$\mathscr{D}_{ij}$ is the binary diffusion coefficient of species i diffusing in species j, defined in Chapter 3.2.3. Equation (3.42) represents the mass diffusion flux in a mass averaged velocity frame. The mass

diffusion flux in a molar averaged velocity frame would be:

$$\boldsymbol{j}_i^U = -M_i \frac{\rho}{M} \mathscr{D}_{ij} \nabla x_i \qquad \text{with} \qquad \sum_{i=1}^{n} \frac{w_i}{x_i} \boldsymbol{j}_i^U = \mathbf{0}, \tag{3.43}$$

where M_i is the molar mass of species i and M is the molar mass of the mixture. Note that normally $\boldsymbol{j}_i \neq \boldsymbol{j}_i^U$, but the entire mass flux of species i has to be same:

$$\boldsymbol{n}_i = \boldsymbol{j}_i + \rho_i \boldsymbol{u} = \boldsymbol{j}_i^U + \rho_i \boldsymbol{U}. \tag{3.44}$$

In analogy, the Fick equation (3.42) in the mass averaged frame can be defined for molar diffusion fluxes in a molar averaged velocity reference frame:

$$\boldsymbol{J}_i = -c \mathscr{D}_{ij} \nabla x_i. \tag{3.45}$$

3.2.2.2 Maxwell-Stefan Model

A more general model to describe diffusive fluxes especially of more than two components is the Maxwell-Stefan model. It is capable of describing typical diffusive effects which occur at multi-component diffusion like counter-diffusion. In the limit of binary-diffusion the Maxwell-Stefan model reduces to the Fick model. The derivation of the Maxwell-Stefan model is based upon a force balance on a control volume [86]. The general Maxwell-Stefan equations have the form [53]:

$$\boldsymbol{d}_i = \sum_{j=1}^{n} \frac{x_i x_j (\boldsymbol{u}_i - \boldsymbol{u}_j)}{\mathfrak{D}_{ij}} \tag{3.46}$$

The driving force $\boldsymbol{d}_i$ for ideal gas mixtures, without external body forces, can be formulated as follows:

$$\boldsymbol{d}_i \equiv -\nabla x_i - \frac{1}{p}(x_i - w_i) \nabla p. \tag{3.47}$$

The diffusion coefficient $\mathfrak{D}_{ij}$ in Equation (3.46) is called the Maxwell-Stefan diffusivity and is related to the binary diffusion coefficient:

$$\mathscr{D}_{ij} = \mathfrak{D}_{ij}\Gamma, \tag{3.48}$$

where Γ is the thermodynamic factor, which can be assumed to be $\Gamma = 1$ for gaseous mixtures at low to moderate pressures [53].

Using the definition of molar fluxes $\boldsymbol{N}_i = c_i \boldsymbol{u}_i$, Equation (3.46) can be reformulated [86]:

$$-\nabla x_i - \frac{1}{p}(x_i - w_i)\nabla p = \sum_{j=1}^{n} \frac{(x_j \boldsymbol{N}_i - x_i \boldsymbol{N}_j)}{c_t \mathscr{D}_{ij}}, \tag{3.49}$$

or in terms of molar diffusion fluxes $\boldsymbol{J}_i$:

$$-\nabla x_i - \frac{1}{p}(x_i - w_i)\nabla p = \sum_{j=1}^{n} \frac{(x_j \boldsymbol{J}_i - x_i \boldsymbol{J}_j)}{c_t \mathscr{D}_{ij}}, \tag{3.50}$$

Unlike the Fick model no reference velocity is defined in the Maxwell-Stefan model (Equation (3.46)), where the species velocities $(\boldsymbol{u}_i - \boldsymbol{u}_j)$ are affected by the driving force. Only $n-1$ molar diffusion fluxes $\boldsymbol{J}_i$ are independent. The selected reference frame resides in the chosen constraint:

$$\sum_{i=1}^{n} \boldsymbol{J}_i = \boldsymbol{0} \quad \rightarrow \quad \text{molar averaged velocity frame} \tag{3.51}$$

$$\sum_{i=1}^{n} \frac{w_i}{x_i} \boldsymbol{J}_i = \boldsymbol{0} \quad \rightarrow \quad \text{mass averaged velocity frame} \tag{3.52}$$

Although it may be sometimes more convenient to use one or the other reference frame, it is advised to use the mass averaged velocity $\boldsymbol{u}$ because this velocity is also defined in the momentum equations. If the velocity $\boldsymbol{u}$ is not zero, a pressure distribution within the microstructure will be calculated, which has a significant influence on the driving force of the Maxwell-Stefan model and the results (see Chapter 6.2.2).

3.2.2.3 Dusty-Gas Model

Both, the Fick and the Maxwell-Stefan model, describe the diffusion of gases. In a porous matrix the interaction between the gaseous species and the pores gets more important. In general, three different types of diffusion mechanisms can be distinguished, depending on the pore size [53]:

- Bulk or free molecular diffusion is significant for large pore sizes, typically >1 µm;
- Knudsen diffusion becomes more dominant if the mean-free path of the species is much larger than the pore diameter. In this case it is more likely for the gas-molecules to hit the walls than to interact with each other;
- Surface diffusion of absorbed molecular species along the pore wall surface, which is prevailing in micro-pores <2 nm.

The dusty-gas model is an extension of the Maxwell-Stefan model taking into account dust particles as an additional species, and considering the interaction between the n species with the immobile and evenly distributed dust particles. The basic equations read [53]:

$$-\frac{1}{RT}\boldsymbol{\nabla} p_i = \sum_{j=1}^{n} \frac{(x_j \boldsymbol{N}_i - x_i \boldsymbol{N}_j)}{\mathscr{D}_{ij}^{eff}} + \frac{\boldsymbol{N}_i}{\mathscr{D}_{k,i}}. \tag{3.53}$$

$\mathscr{D}_{k,i}$ represents the effective Knudsen diffusion coefficient of species i, defined in Chapter 3.2.3. The meaning of the effective diffusion coefficient $\mathscr{D}_{ij}^{eff}$ is a scaled binary diffusion coefficient, which takes into account the influence of the microstructure on the mass-transport, and will be addressed in more detail in Chapter 3.2.4.

It was stated earlier that Knudsen diffusion becomes more dominant if the mean free path of the species molecules is in the range or smaller than the mean pore diameter. The mean free path λ_{H_2} of H_2 can be estimated according to [94]:

$$\lambda_{H_2} = \frac{RT}{\sqrt{2}\pi d_{H_2}^2 N_a p}, \tag{3.54}$$

where N_a is Avogadro's number, R is the gas constant, T is the temperature, d_{H_2} is the diameter of the H_2 molecule and p is the pressure. At an operating temperature of 923 K and a pressure of 1×10^5 Pa, and by assuming that the diameter of H_2 is d_{H_2} =0.2 nm, the mean free path of hydrogen molecules is close to 700 nm. Martin Knudsen also defined a dimensionless number, the so-called *Knudsen*-number K_n [4]:

$$K_n = \frac{\lambda}{L}, \tag{3.55}$$

depending on the mean free path λ of the molecules and a characteristic length L which could be i.e. the average pore diameter d_p.

Knudsen diffusion is relevant if the *Knudsen*-number $K_n > 1$. At the same time this would violate the validity of the continuum modelling approach where the application of the Navier-Stokes equations is justified. This is normally at $K_n < 0.01$, while at $K_n \approx 1$ a slip-flow regime must be assumed [4]. The modelling approach of the Knudsen diffusion takes molecule-wall interactions into account, but is coupled in SOFC-simulations with the continuum approach, which is no longer applicable. Instead statistical mechanics should be pursued. However, the dusty-gas model is widely used in SOFC-simulations [31, 84, 95, 98] with or without the knowledge of its limitations.

3.2.3 Diffusion coefficient modelling

The binary diffusion coefficient $\mathscr{D}_{ij}$ needed for the diffusion models can be estimated by several correlations, namely the Chapman-Enskog model, the Wilke-Lee model or the Fuller-Schettler-Giddings model. A summary of those models can be found in [70]. Only the Chapman-Enskog model is repeated here to highlight the dependencies of the diffusion coefficient. The model is based on the Boltzmann equation and it reads for ideal gases [74]:

$$\mathscr{D}_{ij} = \frac{0.00266 T^{3/2}}{p M_{ij}^{1/2} \sigma_{ij}^2 \Omega_D}, \tag{3.56}$$

where σ_{ij} is the characteristic length defined as the average

$$\sigma_{ij} = \frac{\sigma_i + \sigma_j}{2}, \tag{3.57}$$

M_{ij} is calculated with the molar masses of the species i and j

$$M_{ij} = \frac{2}{\left(\frac{1}{M_i}\right) + \left(\frac{1}{M_j}\right)}, \tag{3.58}$$

and Ω_D is the diffusion collision integral:

$$\Omega_D = \frac{A}{\widehat{T}^B} + \frac{C}{\exp\left(D\widehat{T}\right)} + \frac{E}{\exp\left(F\widehat{T}\right)} + \frac{G}{\exp\left(H\widehat{T}\right)} \tag{3.59}$$

where

$$\widehat{T} = \frac{kT}{\epsilon_{ij}} \qquad A = 1.06036 \qquad B = 0.15610$$

$$C = 0.19300 \qquad D = 0.47635 \qquad E = 1.03587$$

$$F = 1.52996 \qquad G = 1.76474 \qquad H = 3.89411.$$

The Lennard-Jones energy ϵ_{ij} can be determined with:

$$\epsilon_{ij} = \left(\epsilon_i \epsilon_j\right)^{1/2}. \tag{3.60}$$

Thus, the binary diffusion coefficient depends mainly on the temperature and the pressure.

For small porous structures the diffusion coefficient for the Knudsen diffusion is defined as [83]:

$$\mathscr{D}_{ki} = \frac{d_p}{3}\sqrt{\frac{8RT}{\pi M_i}}. \tag{3.61}$$

It mainly depends on the pore diameter d_p and the temperature. Very small pore diameters will lead to a small Knudsen diffusion coefficient. Looking at Equation (3.53) the following cases can be distinguished:

1. $d_p \ll \rightarrow \mathscr{D}_{ki} \ll \rightarrow$ Diffusion mainly influenced by $\mathscr{D}_{ki}$

2. $d_p \gg \rightarrow \mathscr{D}_{ki} \gg \rightarrow$ Diffusion mainly influenced by $\mathscr{D}_{ij}$.

3.2.4 Effective diffusion coefficient

In Chapter 3.2.2.3 an important term for the simulation of homogenised microstructures was introduced: the effective diffusion coefficient $\mathscr{D}_{ij}^{eff}$. Simulations on cell- or stack-level are limited by computer resources, so that a detailed resolution of the microstructure is not feasible. Therefore, these models have to rely on the description of a pseudo-homogenised microstructure, where the complex microstructure is considered as a block with constant porosity ϵ, tortuosity τ and permeability $\boldsymbol{K}$. This approach is also applicable with the previously introduced Fick and Maxwell-Stefan model, where the binary diffusion coefficient is replaced by the effective diffusion coefficient. The reliability of the results depends on an accurate determination of these microstructural parameters.

The determination of the microstructural porosity, as well as the tortuosity will be briefly discussed. An averaged porosity can be easily retrieved from the reconstructed geometry:

$$\epsilon = \frac{\sum_{i=1}^{n} V_{cell,i}}{V_e}, \tag{3.62}$$

where $V_{cell,i}$ is the volume of the i-th porous computational cell and V_e is the entire volume of the reconstructed geometry.

The tortuosity is more difficult to define, let alone to determine. Various definitions exist in literature [82]. A simple geometrical definition of the tortuosity in 2-D is the ratio between the actual distance L_{eff} between point A and B and the geometrically shortest distance L :

$$\tau = \frac{L_{eff}}{L}. \tag{3.63}$$

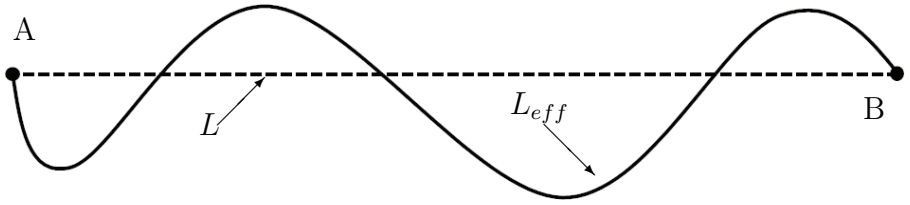

Figure 3.7: Shortest and tortuous path between two points.

Experimental approaches to determine the tortuosity, like saturation current density measurement [87] or mercury intrusion porosimetry [34], are still indirect measurements, as the parameter cannot be measured directly [82].

With the possibility to retrieve 3-D information of the microstructure via measurements techniques described in Chapter 4, computational algorithms like the fast marching method [47] or the centre of mass calculations [33] can be used to determine the geometrical tortuosity. However, the tortuosity was originally introduced as a kinematic property in SOFC models [1], comparable to the relative average length of the flow path of one fluid particle from one side of the porous structure to the other, and does not necessarily equal the geometric definition.

Both, the porosity and the tortuosity are used to scale the binary diffusion coefficient in a way that the solution of a macroscopic approach would yield the same mass-fluxes as the result in the complex microstructure. A comparison between the diffusion flux models of pure gases and gases in an ideal microstructure suggests the definition of a scaling factor f so that $\mathscr{D}_{ij}^{eff} = f\mathscr{D}_{ij}$. The analytical solution of Fick's law in Equation (3.42) yields:

$$\boldsymbol{j}_i = -\rho\mathscr{D}_{ij}\frac{\Delta w_i}{L}, \tag{3.64}$$

where Δw_i is the difference between the mass fractions at a distance L. The binary diffusion coefficient $\mathscr{D}_{ij}$ can be calculated by using various models [74], e.g. Wilke-Lee or Fuller. The decreased mass diffusion due to the presence of a porous media is taken into account by using a scaled effective diffusion coefficient:

$$\boldsymbol{j}_i^{porous} = -\rho\mathscr{D}_{ij}^{eff}\frac{\Delta w_i}{L}. \tag{3.65}$$

$\boldsymbol{j}_i^{porous}$ describes the superficial axial diffusion through the porous matrix. But also the underlying driving force $\Delta w_i/L$ is influenced by the tortuosity [4, 24]. A definition of the average diffusional flux through the pores reads:

$$\boldsymbol{j}_{i,p} = -\rho \mathscr{D}_{ij} \frac{\Delta w_i}{L_{eff}}. \tag{3.66}$$

In order to relate the actual flux in the pores $\boldsymbol{j}_{i,p}$ to the superficial axial diffusion flux $\boldsymbol{j}_i^{porous}$ the residence time t_r of species i could be used, as this has to be the same for both approaches:

$$t_r = \frac{L\rho\epsilon}{\boldsymbol{j}_i^{porous}} = \frac{L_{eff}\rho}{\boldsymbol{j}_{i,p}} \tag{3.67}$$

Note that j_i^{porous}/ϵ would equal the interstitial axial diffusion. Simplifying Equation (3.67) yields

$$\boldsymbol{j}_i^{porous} = \epsilon \frac{L}{L_{eff}} \boldsymbol{j}_{i,p}. \tag{3.68}$$

Inserting Equation (3.66) into (3.68) and using the definition of the geometric tortuosity in (3.63) results in

$$\boldsymbol{j}_i^{porous} = -\rho \frac{\epsilon}{\tau^2} \mathscr{D}_{ij} \frac{\Delta w_i}{L}. \tag{3.69}$$

A comparison between Equation (3.65) and (3.69) shows the relation between the binary diffusion coefficient and its effective counterpart for the microstructure:

$$\mathscr{D}_{ij}^{eff} = \frac{\epsilon}{\tau^2} \mathscr{D}_{ij}. \tag{3.70}$$

For convenience a scaling factor f can be defined, which incorporates the effects of the microstructure:

$$f = \frac{\epsilon}{\tau^2}. \tag{3.71}$$

Although the derivation of the correct scaling factor is straightforward, many SOFC-models [1, 16, 84, 95] use a wrong formulation $f = \epsilon/\tau$. In these macro-scale simulations the tortuosity is often used as a fitting parameter, in which case the misinterpreted use seems not to be crucial. However, correct model equations must be applied, if reliable results are to be expected. This

is even more important in microstructural modelling, where the wrong formulations would lead to erroneous results.

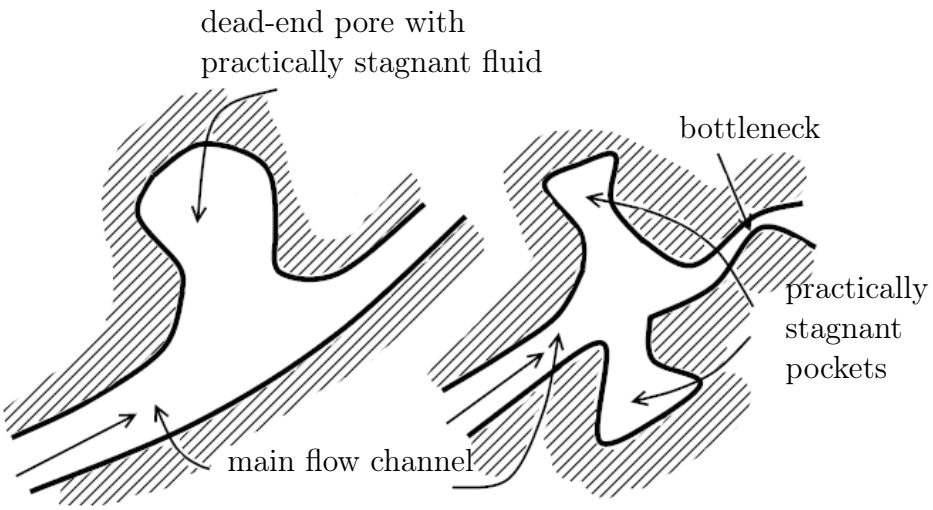

Figure 3.8: Dead-end pores, stagnant pockets and bottlenecks will effect the diffusion in the microstructure according to [4].

The definition of the geometrical tortuosity in Equation (3.63) is an idealised approach, which is not sufficient to describe real microstructures, where also pockets and dead-end pores can be present that influence the diffusion, as pictured in Figure 3.8. In addition to dead-end pores, orifices which impede diffusion have also be taken into account [83].

All these additional microstructural effects are included in the computed tortuosity, for which reason the geometrical definition holds true only for ideal microstructures. This will be shown in Chapter 6.2, where also the correct derivation of the scaling factor in Equation (3.71) will be validated. The tortuosity should therefore be understood as a parameter which describes the microstructure, including orifices, pockets and dead-end pores.

Chapter 4

Geometry reconstruction

The starting point for a simulation is the creation of a computational geometry that resembles reality, and the discretisation of this geometry into a grid, on which the physical models can be solved numerically. The following chapter describes different measurement techniques of microstructures and the reconstruction into a computational geometry. The implications of different possible boundary conditions will be addressed, as well as the problem of the representativity of the investigated volume. Furthermore, different surface representations are compared, namely a voxel (stair-step) surface and a smoothed (body-fitted) surface. Finally, the set-up of an artificial geometry with known geometric properties for validation purposes is described.

4.1 Sample measurement

The microstructure of the electrodes of an SOFC can be analysed by e.g. focused ion beam - scanning electron microscopy (FIB-SEM) or X-ray computed tomography (CT). The established methodology is to apply FIB-SEM measurements on regions with a fine porous structure where a high resolution is needed, see e.g. [47]. The drawback of this procedure is that only a small volume of the electrode can be investigated, whereas CT-scanning can be used to measure a larger region of the microstructure, given that the resolution is good enough to resolve the pores. Nevertheless, X-ray nano-tomography yields comparable results to FIB-SEM [65, 81]

even on smaller scales. The two approaches which complement and overlap each other in their regime of use are described in the following sections.

4.1.1 Focused-ion-beam scanning-electron-microscopy

The basic procedure in the FIB-SEM approach is the ablation of the material with a high current focused-ion-beam and the evaluation of the new surface with scanning-electron-microscopy. A concise description of the FIB-SEM methodology is given in [45]. The process starts with a preparation of the porous sample by infiltrating it under vacuum with a two component epoxy resin. Thus, the mechanical stability is enhanced, milled out material is not deposited in the pores and uncontrolled break-away of particles can be avoided. Furthermore, the contrast between the dark resin and the surrounding material (grey) is much better compared to pure voids, which facilitates the subsequent segmentation between the material and the pores.

The basic assembly is shown in Figure 4.1, where the FIB system is operated at high beam currents to remove material layers with a precision on sub-micron scale [26], and the new surfaces are imaged using SEM. This process is repeated several times to obtain the depth profile of the microstructure.

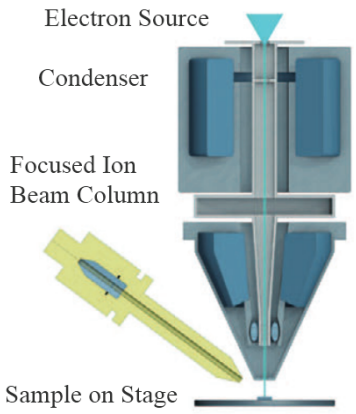

Figure 4.1: Schematic assembly of a FIB-SEM [102].

4.1.2 X-ray computed tomography

In contrary to the FIB-SEM approach X-ray CT is a non-destructive method. The basic assembly can be seen in Figure 4.2. The sample is rotated, while the absorption of the X-ray radiation is measured in the detector. An algorithm reconstructs a 3-D model, using the absorbed intensity for each rotation angle of the sample. This generated 3-D model can in turn be converted into a 2-D image stack with the corresponding depth information. The quality of the results depends on the contrast between the materials, and the resolution of the pictures. For more information the reader is referred to [14] and [49].

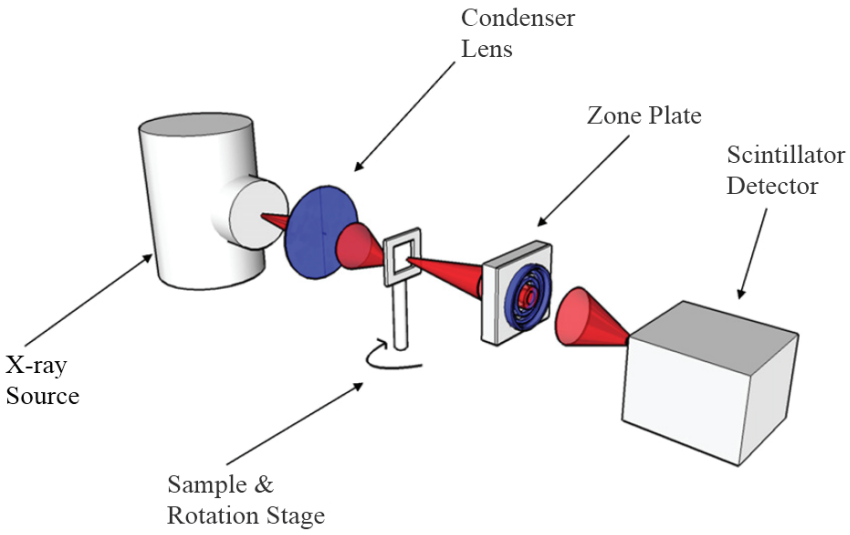

Figure 4.2: Schematic assembly of an X-ray nano CT system: X-ray optics are utilised to focus the incident and transmitted beam, enabling high-resolution 3D X-ray CT imaging [81].

4.2 Reconstruction algorithm

The input of the experimental methods described in 4.1.1 and 4.1.2 for the reconstruction is an image-stack of 2-D pictures, which represent the slices of the material in one direction. The data is processed using an in-house algorithm [56], where statistical functions, based on [11, 19, 97, 100], are applied to evaluate the data. The main goal is to regenerate the microstructure into a computational mesh. The 2-D pictures are processed consecutively, and the grey-scale value of each pixel is compared to the overall histogram of grey-scale values and to the surrounding in

order to determine whether it represents pores or material. Thus the positions where solid or pores are prevailing are identified. The result of one evaluated picture is shown in Figure 4.3.

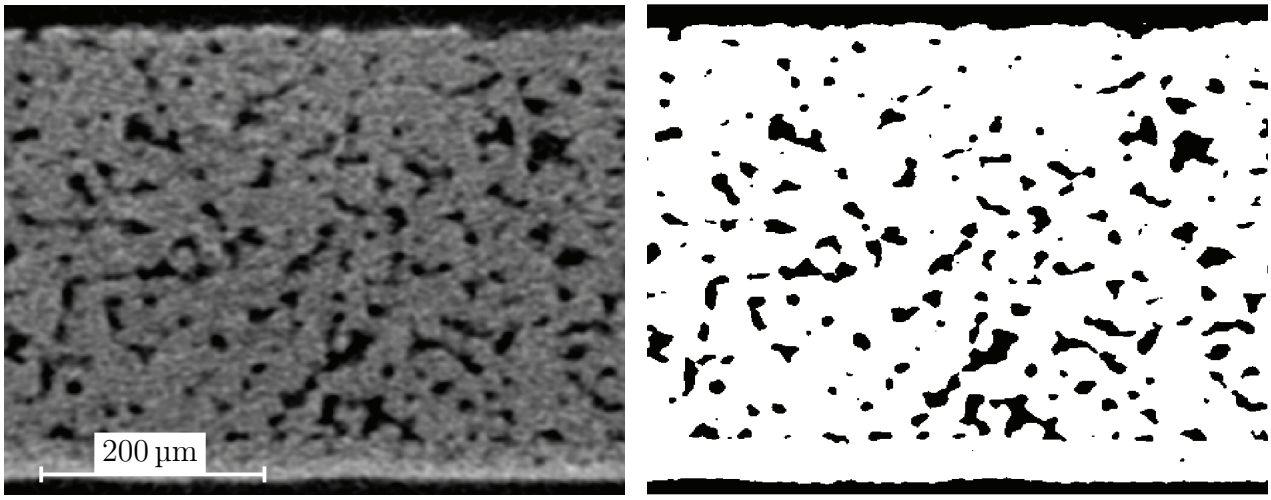

Figure 4.3: Left-hand side shows a single 2-D image representing a slice through the obtained 3-D microstructure with X-ray CT-scans. The digitalised binary image is shown on the right-hand side (white → material, black → pores) [78].

The obtained information of the algorithm is passed to an utility which builds a 3-D voxel mesh with the information of the centre points and the size of the voxels. The dimensions of one voxel correspond to the pixel size and the step width. A schematic description of the reconstruction of a computational geometry out of an image stack is shown in Figure 4.4. From the measured volume ≈1100 µm × 2200 µm × 370 µm a geometry with a volume of 300 µm × 300 µm × 350 µm is selected and reconstructed.

In addition to that, the algorithm applies a special treatment on the lateral boundary faces (parallel to the main diffusion direction, which is in z-direction) and tries to create periodic boundary conditions. The state-of-the-art approach is the application of symmetry boundary conditions which result in a wall and no mass-diffusion in or out of the geometry [33, 35, 45, 46, 94]. This will basically introduce a lot of dead-end pores and will have, depending on the microstructure, an huge influence on the solution, as reported in [78]. Periodic boundaries on the other hand allow mass transport through the boundary by defining that the mass, which leaves on the one side, has to enter on the other, ensuring mass conservation.

One remedy so far is to perform the computation on a sufficiently large volume, so that the ratio between blocked pores due to boundary restriction and continuous pores is very low. In

this case, the influence of the suboptimal symmetry boundary condition will be negligible. The drawback is that a much larger volume of the reconstructed geometry has to be used which leads to the requirement of more computing power and time to perform the simulation. It was shown in [46] that with increasing volume the values of interest (e.g. porosity, tortuosity) converge because the error due to transport via the lateral boundaries decreases. However, no comparison between periodic and symmetry boundary conditions and their influence was made. So far only the effect of different boundary conditions for the top and bottom boundaries is analysed by [55], but not for the lateral boundaries. This gap is closed in this work.

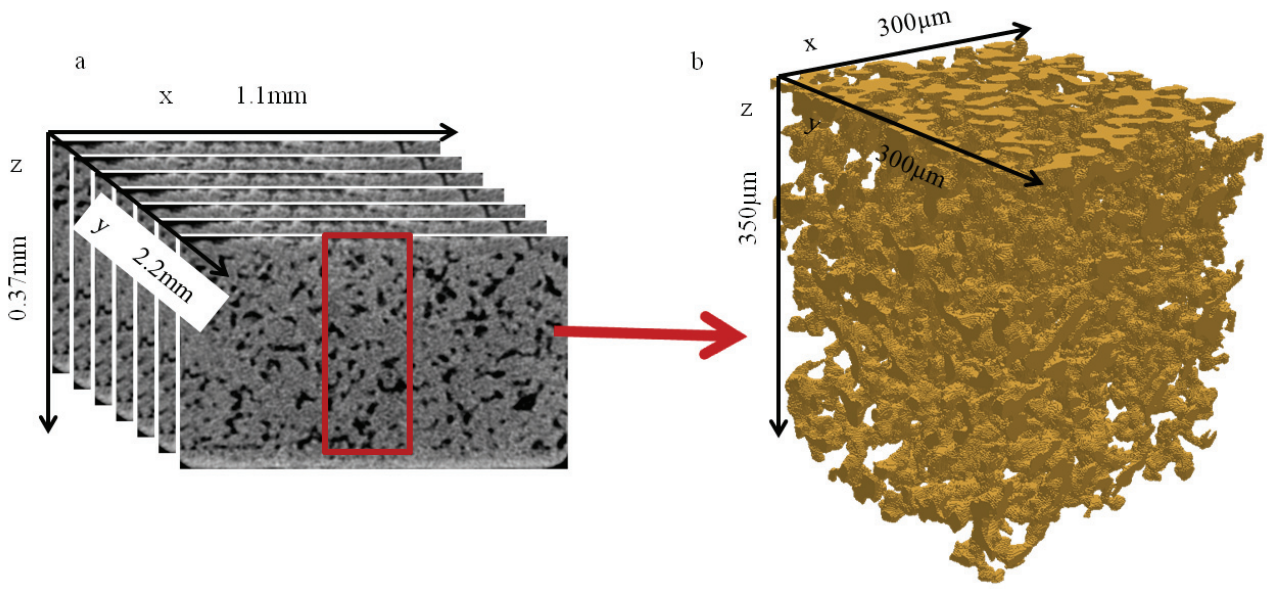

Figure 4.4: Reconstruction of a computational geometry out of an image-stack data-set obtained with X-ray CT [78].

In order to evaluate where periodic boundary conditions can be applied, it is tested if each boundary face on one wall has an corresponding face on the opposite wall. If faces are congruent the labels of these faces are copied in a list where periodic boundaries can be applied, while all boundary faces without an opposite face are written in another list, where only symmetry boundary conditions can be applied. It was thus possible to get the periodic behaviour of the geometry without changing the geometry as such. This approach is straightforward for a voxel-mesh where the faces are either congruent or the don't overlap each other. For the smoothed mesh, no standard tool was available to determine the periodicity because in this case the opposite faces can partially overlap each other. The result of the boundary face evaluation can

be seen in Figure 4.5, where boundary faces in dark blue represent symmetry walls and red boundary faces correspond to periodic boundaries. It is impossible to obtain a 100 % periodic boundary in a real microstructure. In the evaluated metallic support the amount of periodic boundary compared to the entire boundary area is about 17 %. However, with the application of partly periodic boundary conditions many pores are connected with the opposite side, and the amount of dead-end pores is reduced.

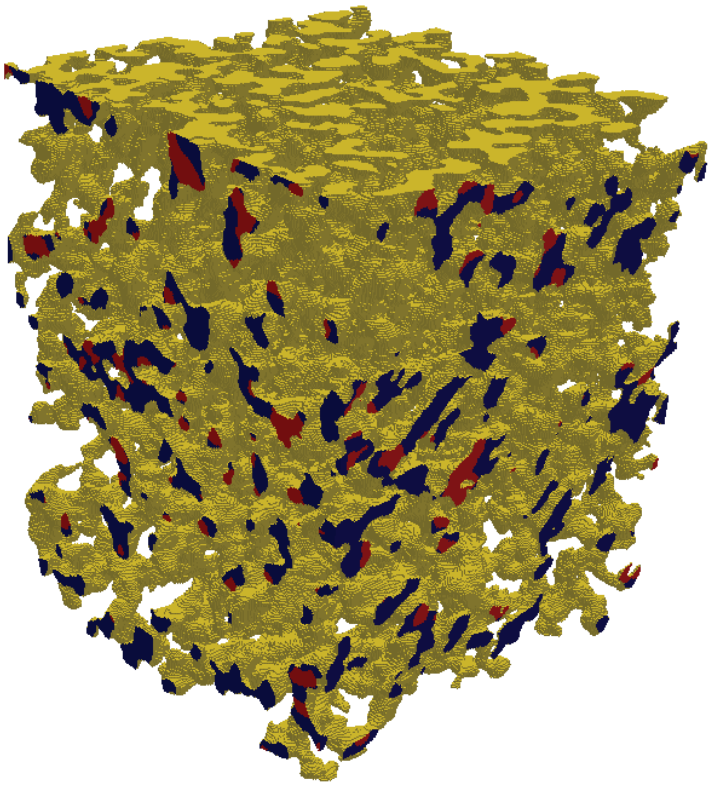

Figure 4.5: Computational geometry with lateral boundaries shown in dark blue → symmetry and red → periodic boundary. The diffusion path is from top to bottom. Approximately 17 % of the lateral boundary area can be defined to be periodic boundaries. The size of the geometry is 300 µm × 300 µm × 350 µm [78].

4.3 Representative equivalent volume

One problem which arises in microstructural modelling is the question of how trust-worthy the results are. The reconstructed volume on which the computations are carried out is roughly 5 millionth of the entire electrode volume. It is very important to determine a volume that delivers representative results. If the control volume is too small, microscopic effects will prevail and

large fluctuations can be observed [4]. At a certain volume these fluctuations become smaller and eventually will converge. One way of finding a representative volume is the so called windowing technique. In this approach a property that describes the microstructure (e.g. porosity) is evaluated for an initial, arbitrarily chosen volume. Then the volume is increased incrementally till the property has reached a constant value [46]. This volume is considered to be large enough to resemble the average properties of the entire electrode.

In order to find a representative volume of the metallic support an algorithm is programmed in *python* [76]. The open-source computer vision library (*openCV* [71]) is used to process the pictures. An image segmentation procedure [32] converts the X-ray image stack to binary images and distinguishes between solid (white) and fluid (black) regions (see also Figure 4.3). The algorithm starts with a predefined volume, segments the pictures and evaluates the porosity. Then the initial volume is increased and the porosity is evaluated again. The user is able to define the initial volume, the increment of the volume and how often it should be made larger.

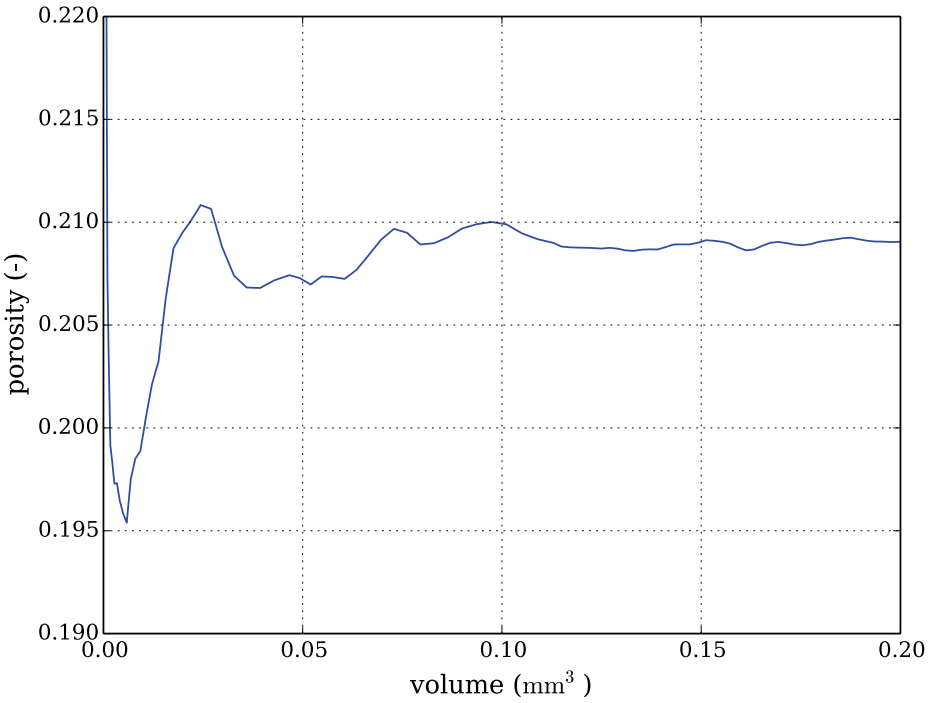

Figure 4.6: Algorithm to determine a representative volume of the metallic support. The porosity is evaluated for increasingly larger volumes till a constant porosity is reached. The minimum representative volume lies in the range of 0.1 mm^3 which corresponds a cube with approx. 500 µm × 500 µm × 350 µm.

The result is plotted in Figure 4.6. At least a volume of $0.1\,\mathrm{mm}^3$ is needed for a porosity which varies only by 2 %. This would correspond to a cube with dimensions of about $500\,\mu\mathrm{m} \times 500\,\mu\mathrm{m} \times 350\,\mu\mathrm{m}$. The length of 350 µm is limited by the height of the metallic support. A geometry of this size with a resolution of one computational cell being $1\,\mu\mathrm{m}^3$ will require 87.5 million cells, which is unfeasible for the computation on standard workstations.

This large representative volume is an indication for the inhomogeneity of the microstructure, which requires a special treatment to ensure representative and thus reliable results. Five independent sample positions on the scanned metallic support where chosen and geometries with a size of $200\,\mu\mathrm{m} \times 200\,\mu\mathrm{m} \times 350\,\mu\mathrm{m}$ where reconstructed. The size is a trade-off between a representative volume and a feasible amount of computational cells so that the computations won't need too much resources. The location of the different sample positions can be seen in Figure 4.7.

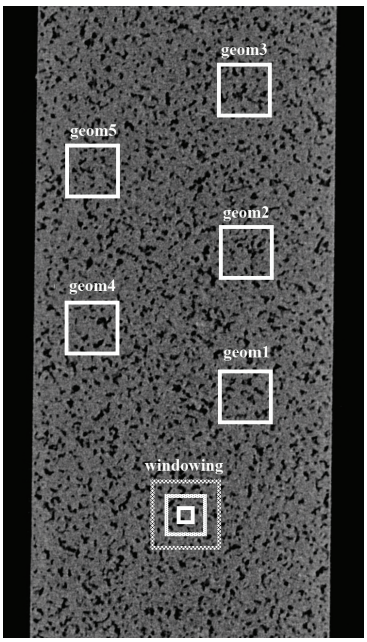

Figure 4.7: Top view of the metallic support with positions of the arbitrarily chosen samples. It is ensured that the sample positions don't overlap and a certain distance is kept to the edges [78]. One continuous square represents an area of $100\,\mu\mathrm{m} \times 100\,\mu\mathrm{m}$.

Although smaller than the computed representative volumes, the evaluation of different sample positions will give a more reliable picture of the microstructure. This is especially true in a very inhomogeneous electrode because several different positions are evaluated which can hugely differ from each other.

One option to reduce the amount of computational cells and to enlarge the considered volume is to increase the size of the computational cells. A doubling of the voxel length from 1 µm to 2 µm results in a decrease of computational cells by a factor of $\approx 2^3 = 8$. Figure 4.8 shows the reconstructed geometry with a volume of 350 µm × 350 µm × 350 µm and from left to right voxel lengths 1 µm, 2 µm and 3 µm.

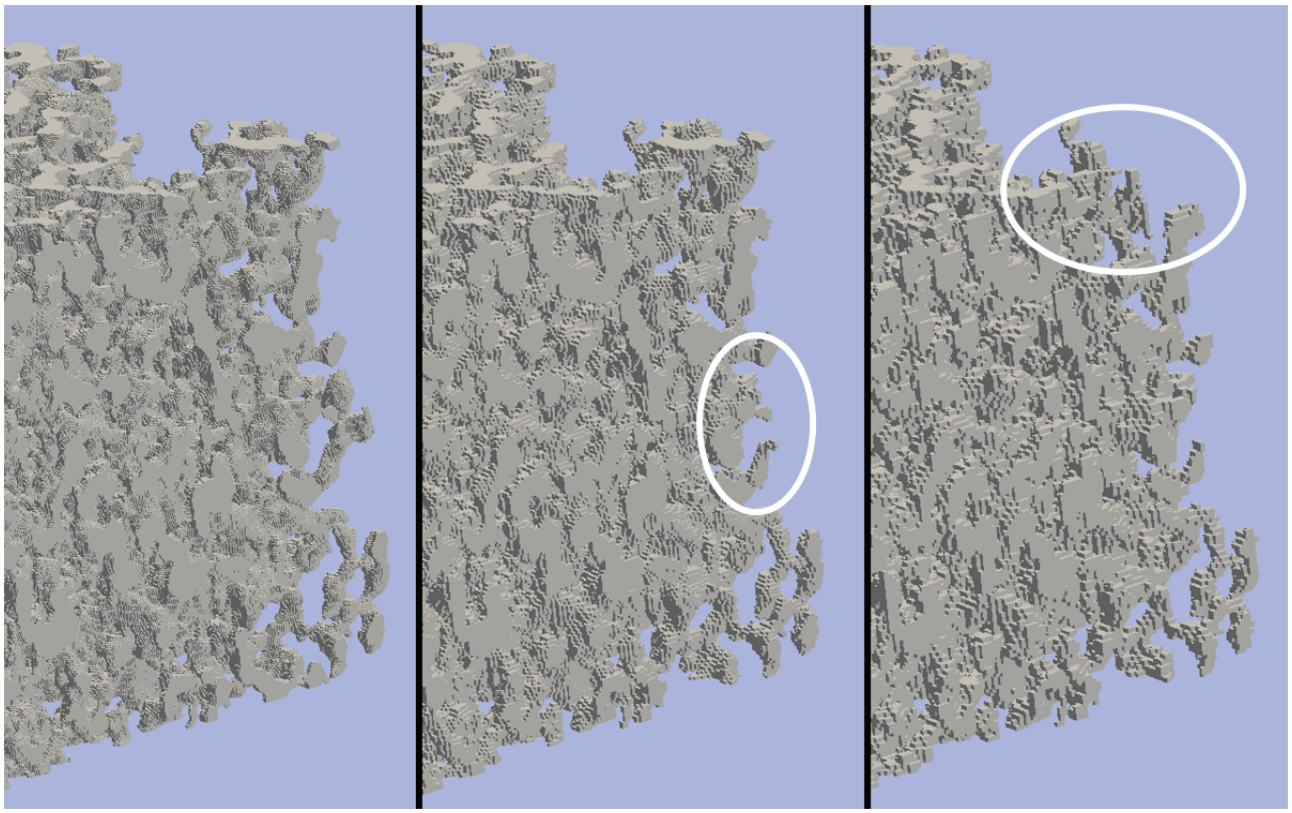

Figure 4.8: Reconstruction of the same geometry with varying voxel volumes from left to right 1 µm^3, 8 µm^3 and 27 µm^3. The circles indicate regions where the pores are not resolved properly and information is lost, compared to the 1 µm^3 case.

It has to be noted that the resolution of the X-ray scan is 1 µm and that the reconstruction algorithm uses this resolution for the segmentation. The outcome of this process step is the left picture in Figure 4.8 with a voxel length of 1 µm. Once the images are segmented a factor can be defined which determines how many pixel should be combined to one. In 3-D a factor of 2 leads to a new voxel which consists of $2^3 = 8$ smaller voxels. Whether the new voxel is solid or fluid depends on the smaller voxels. If the amount of fluid voxels > than the amount of solid voxels, then the new voxel will also be a fluid voxel. If the number of fluid voxels equals the number of solid voxels, then the algorithm decides whether the new voxel is fluid or solid depending on its neighbours.

The comparison of different voxel volumes and its effects on the number of computational cells and the porosity is summarised in Table 4.1. The expected decrease in computational cells can be seen, but also variations in the porosity of $\pm 5\,\%$ can be observed. It is difficult to draw conclusions from these averaged values, so it is worth looking at Figure 4.8 and make a visual comparison between the reconstructed geometries. From this, it can be seen that both geometries with larger voxel-volume lose information and some pores are neglected. Especially bottlenecks between pore volumes tend to be ignored after the change of the resolution, so that pores become separated and are deleted by the algorithm.

Table 4.1: Comparison of reconstructed microstructures with different voxel-sizes.

voxel-volume	number of computational cells	porosity
$1\,\mu m^3$	9.2×10^6	0.209
$8\,\mu m^3$	1.2×10^6	0.215
$27\,\mu m^3$	0.3×10^6	0.197

Furthermore, it is a rule of thumb that at least eight computational cells should fill the diameter of a pore in order to ensure proper simulation results, e.g. a distinct parabolic profile for flows. This supports the approach to entirely refrain from changing the resolution of the geometry and use a voxel length of $1\,\mu m$, despite the drawback of the smaller computational volume which can be evaluated.

4.4 Smoothing of the geometry

The outcome of the reconstruction algorithm (see Section 4.2) is a voxel (stair-step) mesh, meaning that the volume is represented by cubes, and the surface will be overestimated. This may not have an impact in simple problems, like the concentration distribution within the porous microstructure, but it probably has a significant influence on processes where the surface

area is of importance, like e.g. the pressure drop and surface reactions. It is therefore of the utmost importance to represent the structure in an accurate way and in its smooth nature. In literature a rescaling of $\Pi/6$ is proposed [55], but it was pointed out by [78] that the rescale factor depends also on the voxel resolution and the algorithm's capability of recreating the structure with voxels.

In the following section the procedure to smooth the voxel geometry is presented. In order to achieve the smoothing, the open-source utility *snappyHexMesh* which comes along with the *OpenFOAM* distribution is used. The *snappyHexMesh* utility is capable of producing 3-D hexahedral and split-hexahedral meshes from triangulated surface geometries in stereolithography (.stl) format. The initial surface is approximated by refining a starting mesh and morphing the resulting mesh on the surface. Therefore, a coarse hexahedral mesh is defined which overlaps the surface of the microstructure. Each cell that is intersected by the surface is split into eight smaller cells. This process is repeated several times till the refinement at the surface reaches a desired quality.

In a next step the algorithm determines which cells are inside or outside of the STL-surface and removes the predefined ones. The remaining part is called castellated mesh. The last step is the snapping to the surface, where the vertices in the castellated boundary are displaced onto the STL-surface, trying to preserve a pre-defined mesh quality. A more detailed description including pictures to illustrate the process can be found in [20, 72].

The surface of the original voxel geometry could be easily extracted and exported in an stl-format using the open-source software *ParaView* [50]. Two routes have been pursued in order to obtain a smoothed geometry. The first one was to directly use the voxel-surface and try to use bad feature snapping parameters in *snappyHexMesh* to smooth the surface. The other attempt was to smooth the surface prior to the snapping. A comparison between the original and the smoothed surface can be seen in Figure 4.9.

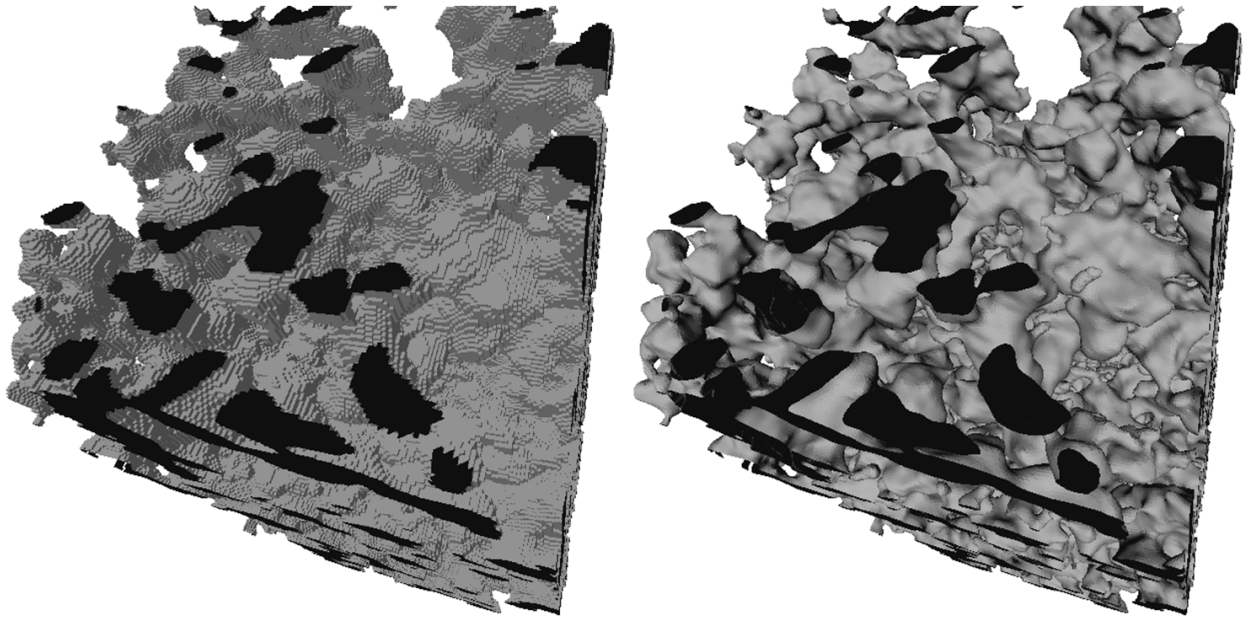

Figure 4.9: Comparison between the original rough voxel-surface (left-hand-side) and the smoothed surface (with *Meshlab*) (right-hand-side).

The smoothing of the surface was carried out with the open-source meshing software *Meshlab* [39]. It offers a huge variety of different filters and morphological operations. One technique to smooth the surface is to use the Gaussian smoothing method, which is a linear technique where the new position of each vertex is computed as a weighted average of the current positions of the vertex itself, and its neighbours which share an edge with the current vertex. It is discussed that this smoothing method has a number of advantages, but produces shrinkage [85].

The Gaussian smoothing algorithm calculates a vector average for each vertex ve_i:

$$\Delta ve_i = \sum_{j \in \tilde{i}} w_{ij} \, (ve_j - ve_i). \tag{4.1}$$

The weights w_{ij} for each vertex ve_i are positive and add up to one. Good results can be obtained with all weights w_{ij} set equal to the inverse of the number of neighbours $1/|\tilde{i}|$. After all vector averages are calculated, the position of the vertexes is updated by adding to each current vertex position ve_i the corresponding displacement vector

$$ve_i' = ve_i + \gamma \Delta ve_i. \tag{4.2}$$

The displacement vector is defined as the product of the vector average Δve_i and a scale factor

γ. The scale factor is a positive number in the range of $(0 < \gamma < 1)$. This is also the source of the shrinkage, as the Gaussian algorithm has to be applied for a number of times to acquire sufficient smoothing. Therefore, [85] suggested to apply two consecutive Gaussian smoothing steps. The first step is carried out with a positive factor γ and is applied to all vertexes. After that, a second Gaussian smoothing step is applied to all vertexes, with a negative scale factor θ, which is greater in magnitude than the first scale factor $(0 < \gamma < -\theta)$ to prevent shrinking. In the current work the improved Gaussian smoothing method is used and the result can be seen in Figure 4.9 on the right-hand-side.

The result of the creation of a volume mesh out of the original stair-step surface and the pre-smoothed surface is depicted in Figure 4.10. The left-hand-side shows a rather coarse surface where the initial cubes still can be seen. In contrast, the right-hand-side shows a smooth mesh, which is used for the simulations. Due to the better visual result it is proposed to smooth the surface mesh prior to the creation of a volume mesh.

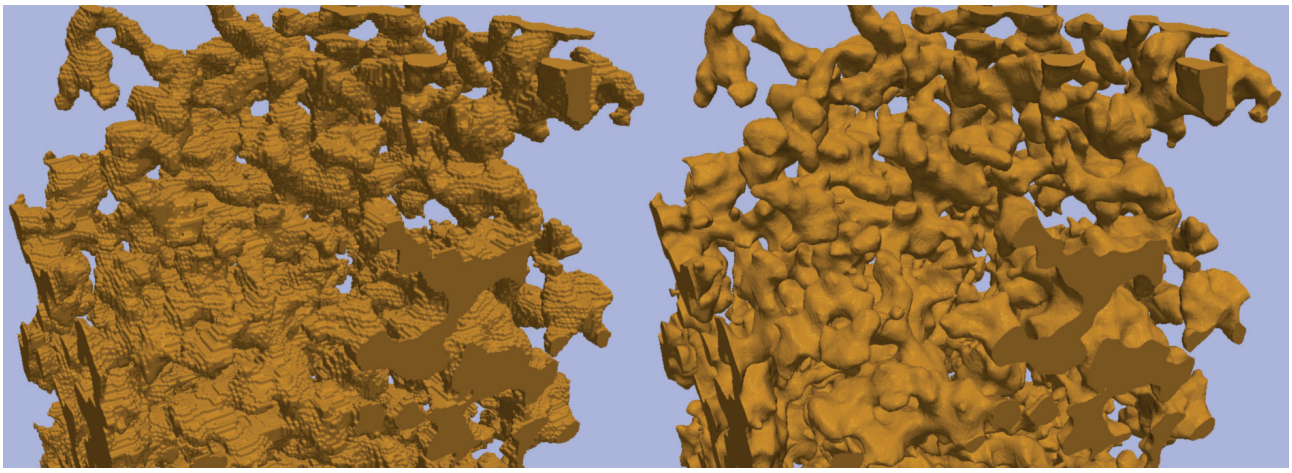

Figure 4.10: Comparison of the final smoothed volume meshes generated by the snapping of the original stair-step surface (left-hand-side) and the pre-smoothed surface (right-hand-side). While the stair-step nature can still be seen on the left-hand-side, the pre-smoothed surface can be converted in a smoothed volume mesh.

SnappyHexMesh offers a wide range of parameters to obtain the desired results. After a lot of volume mesh creations with different sets of parameters the most important are determined: *refinementSurfaces* and *nSmoothPatch*. The *refinementSurfaces* defines the min and max refinement levels of the initial starting mesh. The more often the starting mesh is refined, the better the surface mesh is approximated. This can be seen in Figure 4.11 where the red areas are obtained with a lower refinement level compared to the green areas which fill the stair-step

surface to a significantly higher degree. The *nSmoothPatch* sets the number of patch smoothing iterations before the correspondence to the surface is found. The more patch smoothing iterations are applied the smoother the surface gets.

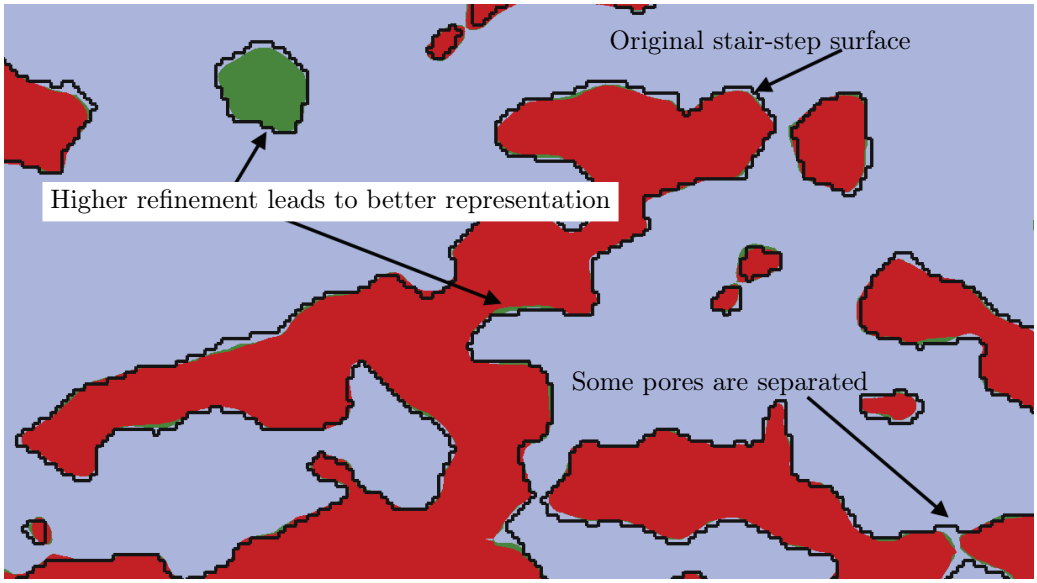

Figure 4.11: Comparison between the stair-step surface mesh and the final volume meshes for different parameter settings in *snappyHexMesh* for an arbitrarily chosen slice position of the geometry. The black lines represent the original stair-step surface, which is smoothed and then snapped. The red areas show the volume mesh with a lower refinement, while the green areas are obtained with a higher refinement. The higher the refinement the better the reconstruction of the initial geometry gets.

A comparison between the geometric features of the voxel and smoothed microstructure can be found in Table 4.2. A slight difference in the porosity can be observed which may come from the fact that in the smoothing procedure 1 µm of each edge is cut away to ensure proper results. The difference between the surface area of nearly 37 % is more striking. This is a quantification of the overestimation of the surface area by the voxel mesh and it is lower compared to the factor $\pi/6$ proposed by [55].

To what extent this will have an influence on the computational results will be discussed in Chapter 6 and 7. One drawback of the smoothing is the increase of computational cells because of the algorithm used in *snappyHexMesh*. Many refinement steps are needed in order to obtain a good representation of the initial geometry, which in turn results in a higher number of computational cells.

Another problem which comes along with the creation of a smoothed volume mesh out of a stair-step surface is that not only the visual result, but also the mesh quality depends on

Table 4.2: Geometric features of voxel and smoothed microstructure.

	porosity (-)	surface area m^2	computational cells
voxel	0.214	1.40×10^{-6}	3.1×10^6
smoothed	0.207	0.89×10^{-6}	5.1×10^6
difference	-3.3%	-36.6%	64.5%

the chosen settings for *snappyHexMesh*. The particular problem in this case are so called skewed faces. This means that the intersection between a straight line of two centre points of neighbouring cells and the corresponding cell face lies far away from the centre point of this face, see Figure 4.12.

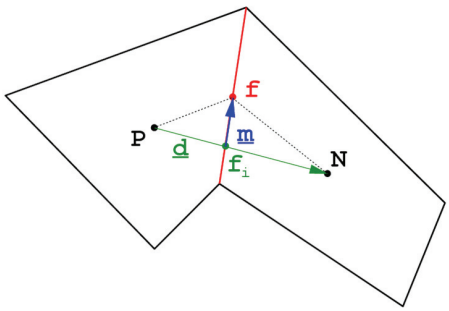

Figure 4.12: Description of skewness. The centre point of the shared face **f** deviates from the point $\mathbf{f_i}$ obtained by the intersection between this shared face and a straight line between the two centre points **P** and **N** of the cell [41].

The implication of this is, that the calculation of face integrals requires the value of the variable in the middle of the face (point **f** in Figure 4.12):

$$\int_f \mathrm{d}\boldsymbol{S}\phi = \boldsymbol{S}\phi_f. \tag{4.3}$$

The face value ϕ_f is calculated by linear interpolation between the points **P** and **N**. This actually gives the value of ϕ at the point $\mathbf{f_i}$ [41], for which reason the interpolation of the convection term introduces a diffusion-like error. This error will be smaller compared to the numerical diffusion from the convection differencing scheme on meshes with reasonable good

quality ($|\boldsymbol{m}| < |\boldsymbol{d}|$ in Figure 4.12). On highly distorted meshes the influence of this term can be significant. Nevertheless, this problem can be handled with appropriate settings of the discretisation schemes. Namely the usage of a least-square gradient scheme in *OpenFOAM* is recommended [42, 43].

4.5 Artificial geometry

The complexity of the microstructures often does not allow the comparison of simulation results with simple analytic solutions. It was therefore tried to create artificial microstructures with pre-defined geometric features, which could be used for a validation of the simulation results. Here, a *python* program is designed which is capable of producing a picture stack (similar to what would be the input from X-ray tomography) from simple tubes or spheres.

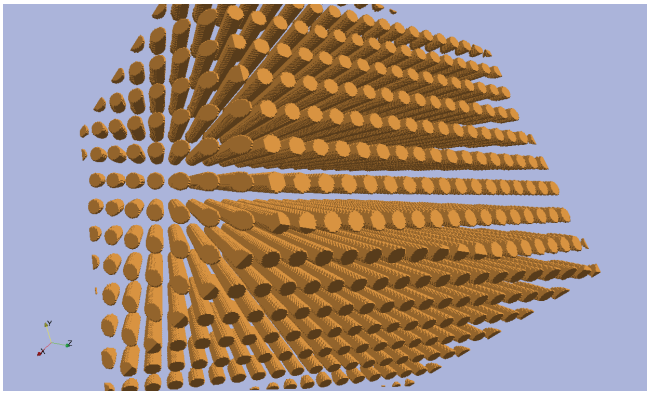

Figure 4.13: Simple artificial microstructure consisting of small tubes with a diameter of 10 µm and a normal distance of 20 µm. The overall size of the geometry is 222 µm × 286 µm × 213 µm. All faces on opposite walls are periodic. Note: The pores on the left-hand side look slightly distorted due to the perspective.

One example artificial microstructure is shown in Figure 4.13. It consists of straight tubes with a diameter of 10 µm and a normal distance of the centre points of 20 µm. In addition to these values, the user is able to define the direction vector of the pores. With vector analysis the size of the cube is determined where the boundaries in all three dimensions are periodic. This is needed to prove the applicability of periodic boundary conditions in microstructural computations. The heart of the algorithm for pore location determination is summarised in Listing 4.1

Listing 4.1: Code snippet from the python program: Determination of tube positions and colouring of picture

```
for i in range(nx):
        for j in range(ny):
            for k in range(nz):

                # the point is rotated to a plane orthogonal to the direction vector

                di,dj,dk=drehMatrix([i,j,k])

                # Now the cross section of the tube is a circle and
                # the actual position is calculated with respect to the
                # distance between the tubes

                dy=np.mod(dj+distance/2.,distance)-distance/2.
                dz=np.mod(dk+distanceZ/2.,distanceZ)-distanceZ/2.

                # if the length of the y,z position is within the tube
                # radius then the position is marked black(False in matrix)

                length=np.sqrt(pow(abs(dy),2)+pow(abs(dz),2))

                if length<=radius:
                    data[i,j,k]=False

    return data
```

A 3-dimensional boolean matrix is set up which resembles our picture stack, and is initialised with *True* which would equal to white. Every point of this matrix is now rotated with a rotation matrix in a plane which is orthogonal to the direction vector of the tubes. Thus the cross sections of the tubes are circles. The distance of the points from the centre points of the tubes are calculated with a *modulo*-function. If this distance is smaller than the defined diameter, the point lies within the tube and is marked black (*False*) in the original position. The result is a black and white picture-stack showing the cross-section of the pores for individual slices (see Figure 4.14). The exported pictures can then easily be converted to computational geometries using the reconstruction algorithm (see Section 4.2).

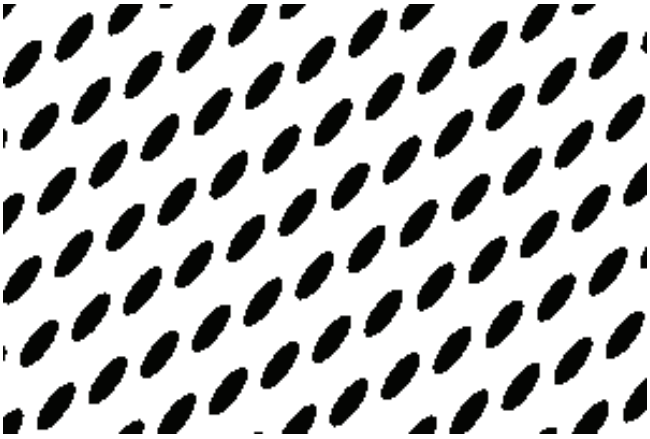

Figure 4.14: One generated slice which represents the cross-section of tubes with a pre-defined direction. The circular sections of the tubes are presented as ellipses.

Chapter 5

Simulation and modelling

5.1 Corrosion simulation

In this chapter the main focus lies on the development of a corrosion model that is capable of determining the oxide growth and the change of the porous volume in the metallic support. The main ideas of the model have already been presented in [77] and will not be referenced each time.

5.1.1 Simulation approach

Various researchers focused on the development of algorithms and models to describe corrosion. They analysed the species concentration of the metal-ions in the oxide, while the growth of the oxide was more or less a boundary condition [37, 67–69, 75]. In this work however, it is abstained from determining the oxide composition, as the focus is laid on the change of the porous volume due to the oxide growth.

Before coming to the actual model equations it is worthwhile having a short excursus in understanding the finite volume discretisation in *OpenFOAM*. In order to solve partial differential equations the computational domain is subdivided into small volumes. By applying numerical methods the partial differential equations are converted into a system of algebraic equations,

which can be solved using appropriate methods. *OpenFOAM* uses two distinct kind of fields (arrays) where all values of the discretized geometry are stored: Firstly, volume fields, where the values (e.g. pressure, temperature, velocity, concentration, porosity, ...) are defined at the cell centres of the volumes. Secondly, surface fields, like for example the mass flux, are stored at the face centres. In the corrosion model the oxide thickness, as well as the metal-retraction, are stored at the face centres, while the porosity change caused by corrosion ϵ_{corr} is treated as a volume field.

In order to resolve the growing of the oxide a very fine mesh would be required at the metal-gas interface. Furthermore, the growth of the oxide and thus the decrease of the open pore space would require the re-meshing of the computational geometry. Both, a large number of computational cells and the re-meshing of the geometry consume a large amount of computer resources, which in turn would result in long computation times. In order to avoid the re-meshing, the growth of the oxide is taken into account as an additional porosity ϵ_{corr} which effects the mass-diffusion through the pores. Thus, the amount of computational cells can be significantly reduced and the re-meshing avoided resulting in fast computations.

The calculations are carried out on a metallic support described in Chapter 2.2, which is reconstructed into a computational voxel geometry (see Chapter 4.2). It is assumed in the corrosion model that only the least noble element forms the oxide, which is, in the case of the metallic support, chromium. The oxide film is considered to be perfectly adherent and does not show any cracks or holes. Furthermore, it is assumed that the film does not spall.

The oxide growth is described in the initial regime by an integrated and enhanced form of the linear growth law Equation 3.9:

$$x_{corr}(t + \Delta t) = x_{corr}(t) + \frac{k_l \Delta t}{n} \kappa \qquad t \leq t_p, \tag{5.1}$$

where k_l is the linear rate constant, n is the number of corroding faces that belong to one corresponding source face, κ is the geometry correction factor and t_p is the time at which the linear rate is switched to the parabolic rate. Here, the integrated form of Equation (3.6) is

implemented with the improvement of limiting the growth by n and the geometry correction κ:

$$x_{corr}^{new}(t+\Delta t) = \sqrt{\left(x_{corr}^{old}(t)\right)^2 + \frac{k_p \Delta t}{n}\kappa} \qquad t > t_p. \tag{5.2}$$

A principal sketch of the basic mechanism is depicted in Figure 5.1 and the meaning of n and κ will be explained below. At the beginning the corroding and the source (retracting) face (green in Figure 5.1(a)) are identical. The thickness of the oxide, as well as the retraction, are stored as surface fields. As the oxide grows the porosity in the cell (stored as volume field) will change (light red in Figure 5.1(b)). At a certain point the first cell will be entirely filled, and the algorithm will determine the new faces where the corrosion can continue (dark red in Figure 5.1(c)).

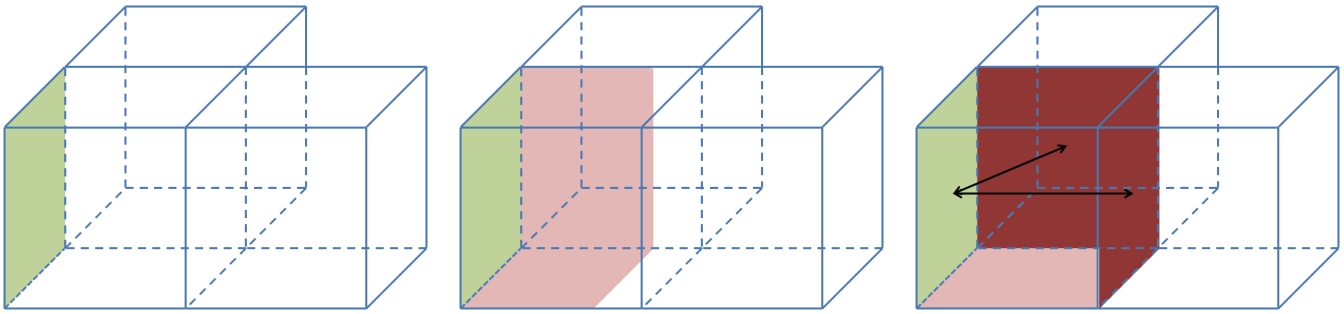

Figure 5.1: Basic principle of corrosion model implementation: (a) Initial corroding and corresponding source (retracting) face are the same (green face). (b) The oxide starts to grow and continuously fills the volume of the cell (red), taking the retraction of the boundary into consideration. (c) After the cell is completely filled potential faces to neighbouring cells are the new corroding faces (dark red). The distance to the initial source face (green) is calculated, including its retraction. Now two corroding faces obtain the Cr-ions from one source face $\rightarrow n = 2$ and the growth is limited, to ensure mass conservation of the Cr-ions [77].

The new oxide thickness is determined by vector analysis between the centre points of the new corroding faces and its corresponding source face, including its retraction. The number of corroding faces (dark red) that obtain their Cr-ions from one source face (green) is determined. As shown in Figure 5.1(c), the ratio between corroding faces to source faces is $n = 2$, and the growth on these faces is limited, so that the mass of Cr-ions is conserved.

The complementary case would be a computational cell, which corrodes from more than one side. This cell would be filled twice as fast (if it has two corroding surfaces) than a cell corroding only from one side. Figure 5.2(a) shows the voxel representation (thick black line) of a straight

line (green). This would be the worst case scenario, where the computational cells are not aligned with the surface, but rotated by 45°. The wrong surface interpretation of the voxel geometry has already been addressed in Chapter 4.4.

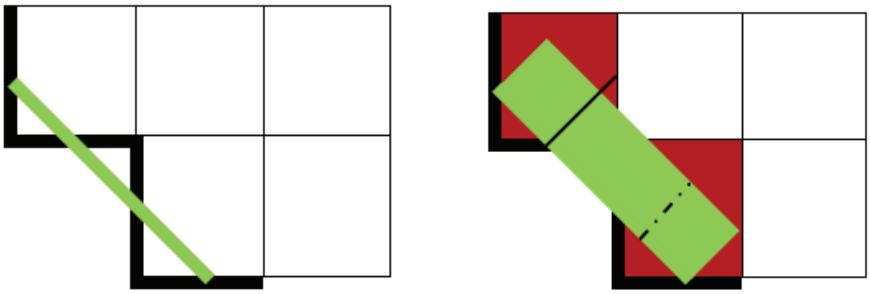

Figure 5.2: Sketch showing the influence of the voxel geometry on the growth and the need for a geometry correction factor. The initial surface (green line) is approximated by voxel (thick black line). Cells that are corroding from more than one side are filled earlier, resulting in an overestimation of the oxide growth.

In general a computational cell will be full if the oxide thickness x_{corr} satisfies:

$$x_{corr}\kappa = \frac{l}{F_c} + r, \tag{5.3}$$

where κ is the proposed correction factor, l is the edge length of the voxel (equals the length of the square in Figure 5.2), r is the retraction and F_c is the number of corroding faces per cell. Figure 5.2(b) shows the state after the first cell layer is entirely filled (red squares). Compare the continuous black line with the dashed line which would equal the oxide thickness of an 1-D growth and is lower than the oxide thickness in the voxel case. The introduction of the growth correction factor κ aims at limiting this grid influence.

After one cell layer is filled, new corroding faces in the voxel geometry are determined as the interface between oxide and pores and the actual oxide thickness is computed by vector analysis between the face centre points of the new corroding faces and the shortest distance to the source boundary faces, including their retraction. This equals the diagonal of the cube (see continuous black line in Figure 5.2(b):

$$x_{corr} = l\sqrt{\frac{1}{G}} + r, \tag{5.4}$$

where G is a growth parameter defined as:

$$G = \begin{cases} 1 & \text{for } F_c = 1 \\ 2 & \text{for } F_c \geqq 2 \end{cases} \tag{5.5}$$

In the case of Figure 5.2 the number of faces per corroding cell F would be 2 and neglecting the retraction $r = 0$ in this thought experiment, the cell will be filled twice as fast compared to a cell corroding only from one side. The new oxide thickness will then jump from $l/2$ to $l/\sqrt{2}$, which would correspond to the nearest distance to the source surface. Each time a new cell layer will be filled the oxide will jump again and the growth will be overestimated.

The Pilling-Bedworth ratio for Chromium is 2.02 [44], and the metal-retraction r can be estimated:

$$r \cong \frac{1}{2} x_{corr}. \tag{5.6}$$

Inserting Equation (5.6) in Equations (5.3) and (5.4) and solving for κ yields a growth correction factor for Chromium:

$$\kappa = \sqrt{\frac{G}{4F_c^2}} + \frac{1}{2}. \tag{5.7}$$

Once the oxide thickness growth $\Delta x_{corr}^{t \to t+\Delta t}$ during the time step Δt is determined, an enhanced form of the proposed mass balance by [37] can be used to calculate the metal-retraction:

$$\Delta r^{t \to t+\Delta t} = -V_m \frac{z_{ox} \rho_{ox}}{M_{ox}} \Delta x_{corr}^{t \to t+\Delta t} \frac{A_{corr}}{A_{source}}. \tag{5.8}$$

Equation (5.8) is the combination of Equations (3.11) and (3.12) presented in Chapter 3.1.1, expanded by the ratio between the corroding area A_{corr} and the retracting or source area A_{source}. This term is important if the calculations are carried out on unstructured grids, where the face areas may be different. On structured grids A_{corr}/A_{source} equals 1.

With the knowledge of the oxide thickness and the metal-retraction the change of the pore volume V_{diff} can now be estimated:

$$V_{diff} = A_{corr} \left(\Delta x_{corr} - \Delta r \right). \tag{5.9}$$

This leads directly to the evaluation of the local porosity ϵ_{corr} of each computational cell:

$$\epsilon_{corr} = 1 - \frac{V_{diff}}{V_{cell}}, \tag{5.10}$$

where V_{cell} is the volume of a computational cell. A porosity of 1 indicates regions without oxide, while a porosity of 0 means that this domain is entirely corroded.

The basic work-flow of the corrosion algorithm is summarised in Listing 5.1. During the time loop the algorithm calculates the oxide thickness either according to the linear or parabolic rate law. The additional oxide calculated within a time step is used to determine the Cr-ion flux and thus the retraction of the metal. With the new location of the oxide interface the porosity can be updated.

As soon as one computational cell is entirely filled with oxide the method *handleFilledCells* is called. Here, the storage and coupling of the corroding and source (retracting) faces is updated. In the first step, each face of the volume cell is identified and it is checked, whether the neighbouring cell is already filled or not. If it is not filled, the oxide can grow in this direction. Then the shortest distance to all possible source faces is calculated using vector analysis, taking into account their actual retraction. It is assumed that the corroding face obtains its Cr-ions from the closest source face. This pair of faces is stored in a hash-table. The old corroding faces are deleted from this list. In a final step it is checked, how many corroding faces belong to one source face (corresponds to the value n) and this information is stored in a separate hash-table.

Listing 5.1: Basic functionality of the corrosion algorithm

```
// function that maps the corresponding corroding
// and source faces and stores it in a hashTable
faceTofaceMapping corrFaces <- boundaryFaces[corrosion]

while corrFaces.length()>0 do:
   // solution of the rate law
   forAll ith faces from corrFaces
      if(t<=tp)
         solve Equation (5.1)
      else
         solve Equation (5.2)
   end
   // calculation of the metal-retraction
   forAll ith faces from corrFaces
      solve Equation (3.12)
   end

   // calculation of local porosity
   forAll ith corrodingCells
      solve Equation (5.10)
   end

   if eps_corr>fillingLimit
      // handle filled cells
      1. find faces to neighbouring cells that are not entirely filled --> insert in corrFaces
      2. determine the shortest distance to source faces and subtract retraction -->
          x_corr_full; add boundary face as corresponding face
      3. delete current corroding face from corrFaces
   end
end
```

A concise explanation on how the oxide thickness, the weight gain and the porosity is evaluated shall be given. During the corrosion it can occur that one computational cell has more corroding faces with different oxide thicknesses. This is depicted in Figure 5.1(c), where the distance between the two dark red faces to the green face differs. The average oxide thickness is determined by looping over all currently corroding cells and determining the average oxide thickness.

The evaluation of the mass gain defined as $\mathrm{kg\,m^{-2}}$ comprises the difficulty to which surface the additional mass should be related to. The additional weight Δm_{ox} can be easily determined by summing over the incremental oxide volume:

$$\Delta m_{ox} = \sum_{i=1}^{n} \Delta x_{corr} A_{corr} \rho_{ox}, \tag{5.11}$$

where $\Delta x_{corr} A_{corr}$ is the additional oxide volume. The surface area will change during the oxide growth depending on the curvature of the geometry. In a convex geometry (growing outward) the surface area will decrease, while in a concave geometry (growing inward) the surface area

will increase. A more detailed discussion, as well as a figure, can be found in Chapter 6.1.

Due to this change of the surface area it seemed to be best practice to use the initial surface area A_{init} for the calculation of the mass gain w_{ox}:

$$w_{ox} = \frac{\sum_{t=0}^{t_{end}} \Delta m_{ox}}{A_{init}}. \tag{5.12}$$

A detailed validation of the corrosion algorithm is presented in Chapter 6.1 and computational results on real metallic support microstructures are summarised in Chapter 7.3.

5.2 Porosity distribution and geometric evaluation

The measurement techniques presented in Chapter 4.1 provide a deep insight into the complex metallic support microstructure. In order to get the most out of it, the effort was taken to program a *MATLAB*-algorithm that is capable of evaluating the porosity distribution, the mean pore diameter, number of the pores, etc. which is also presented in [78]. The input-data are the positions of the centre points of the computational volume cells, including various additional information e.g. concentration, pressure, mass-flux and oxide at these points. In a first step the 3-D position information of the cell centres is sorted along a chosen coordinate axis. If, for example, the z-coordinate is selected for evaluation, the cells are sorted along the z-axis and for each height a binary matrix is created. The elements of the matrix represent scalar values at cell centres of the computational geometry at this z-position ($0 \rightarrow$ metal, $1 \rightarrow$ pore).

These matrices can be processed with the *Image Processing Toolbox* namely the *bwlabel*-function, which evaluates connected components and labels them. Figure 5.3 shows the geometry with its slices and one evaluated sample slice of the geometry. Connected pores are labelled and highlighted in different colours.

The obtained geometric information of the slices can now be used to determine various microstructural parameters. The knowledge of the individual pore areas in each slice can be used to

calculate an equivalent pore diameter (diameter of a circular shaped pore with the same area). Also the number of pores can easily be retrieved, by summing up the individual pores per slice. The porosity distribution can be evaluated by determining the porosity of each slice. This yields a more significant information of the microstructure, as its homogeneity can be assessed, or regions with different porosities can be discerned.

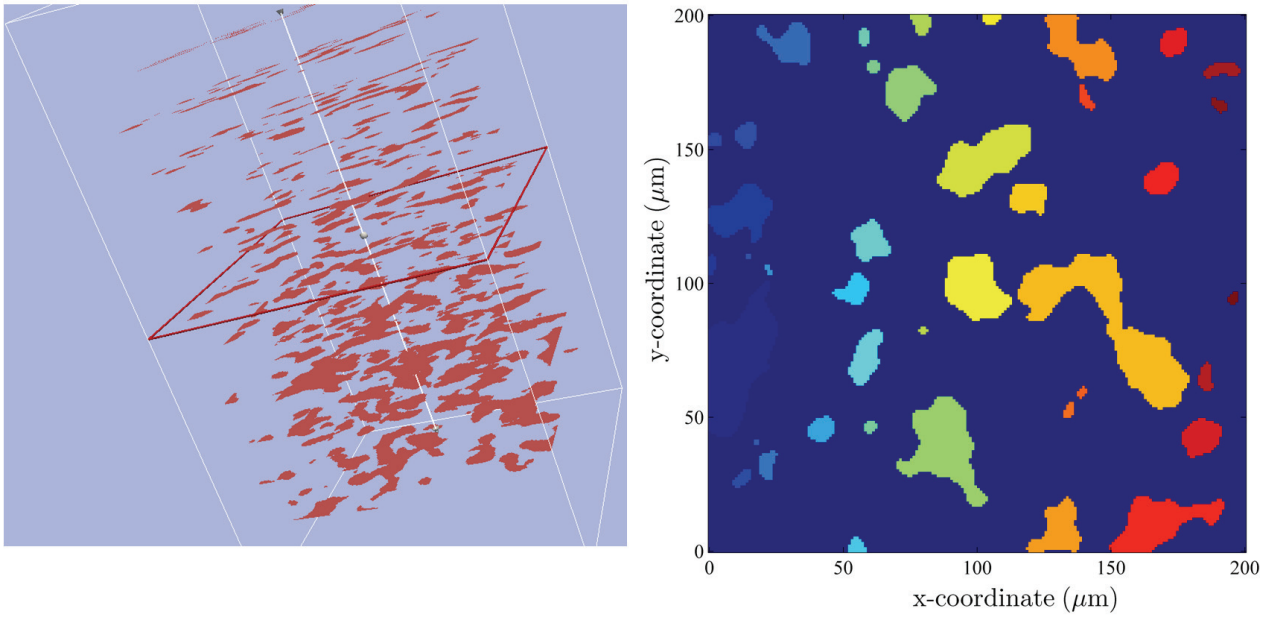

Figure 5.3: Evaluated sample slice of the microstructure. Connected pores are highlighted in different colours [78].

Similarly to the determination of the porosity distribution, also the concentration or the pressure distribution along one coordinate axis can be evaluated. This gives a more profound picture of the microstructure, as well as the species distribution, and may highlight potential for improvement.

5.3 Mass-transport simulation

5.3.1 Flow simulation

In general, the flow through a porous medium in macroscopic simulations can be described with the volume-averaged Navier-Stokes equations [4]. Assuming steady-state conditions, Stokes flow

(small Reynolds number) and homogeneous porosity these equations can be reduced to Darcy's law (Equation (3.20)) [70]. In microstructural modelling, however, the porous structure is known and the flow is simulated only in the pores, while the solid acts as an obstacle and the Navier-Stokes equations can be applied [6]:

$$\rho\frac{\partial \boldsymbol{u}}{\partial t} + (\rho\boldsymbol{u}\cdot\nabla)\,\boldsymbol{u} = -\nabla p + \mu\,\triangle\boldsymbol{u} + (\lambda+\mu)\,\nabla\,(\nabla\cdot\boldsymbol{u}) + \boldsymbol{f}, \tag{5.13}$$

wherein ρ is the density of the fluid, $\boldsymbol{u}$ is the actual velocity in the microstructure, p is the pressure, μ the dynamic viscosity, λ the first Lamé constant defined as $\lambda = -\frac{2}{3}\mu$ and $\boldsymbol{f}$ describes various volume forces such as gravity. Together with the continuity equation for incompressible fluid

$$\nabla\cdot\boldsymbol{u} = 0, \tag{5.14}$$

Equation (5.13) simplifies to:

$$\rho\frac{\partial \boldsymbol{u}}{\partial t} + (\rho\boldsymbol{u}\cdot\nabla)\,\boldsymbol{u} = -\nabla p + \mu\,\triangle\boldsymbol{u} + \boldsymbol{f}. \tag{5.15}$$

In order to solve the momentum equations and to calculate the flow field, standard numeric techniques are applied namely the *SIMPLE*-algorithm (Semi-Implicit Method for Pressure-Linked Equations) [73]. An implementation of this algorithm is provided by the standard *OpenFOAM*-solver *simpleFoam*, which solves the steady-state, incompressible Navier-Stokes equations, for given boundary conditions.

For a correct solution a sufficiently large in- and outlet section has to be added to the porous geometry. The length of the inlet section should ensure the formation of a parabolic flow profile. More care has to be taken at the outlet section, which should be large enough that no back-flow can occur. As the fluid has to flow through the pores, these act as jets at the outlet yielding swirls, which could cause back-flows. A longer outlet section allows the flow to level out and form again a parabolic profile.

In Figure 5.4 two cases with an in- and outlet section at different flow velocities are shown, where the flow direction is from left to wright. The dimensions are: inlet section 200 µm; metallic support 350 µm and outlet section 400 µm. Due to the low velocities and the small pores, creeping flow can be expected and the Reynolds number indicates laminar flow. Nevertheless, the in- and outlet section is too short for a velocity of $0.2\,\mathrm{m\,s^{-1}}$, which can be seen at the distorted streamlines in Figure 5.4(a). The results of such simulations may be influenced by back-flows and are not reliable. On the other hand, Figure 5.4(b) shows straight streamlines which go through the microstructure, and expand in the outlet section without distortions.

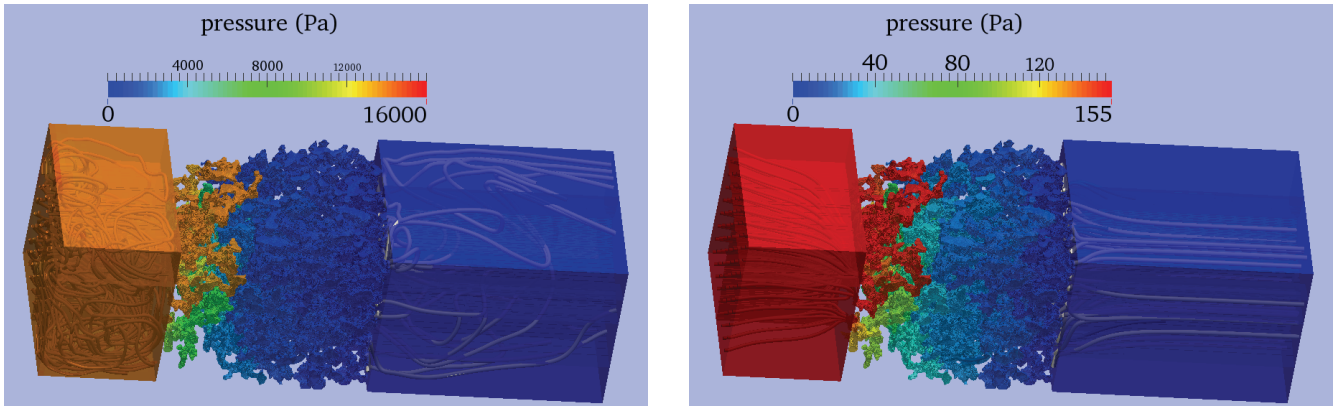

(a) Pressure distribution and streamlines at a superficial velocity of $0.2\,\mathrm{m\,s^{-1}}$

(b) Pressure distribution and streamlines at a superficial velocity of $0.01\,\mathrm{m\,s^{-1}}$.

Figure 5.4: Reconstructed microstructure of the metallic support with an 200 µm long inlet and an 400 µm long outlet section. The inlet section should be long enough to form a parabolic flow profile, while the outlet section should assure that no back-flow occurs. In the case of the higher velocity (a) the inlet, as well as the outlet section is too short and the streamlines indicate back-flow. At lower velocities (b) both sections are sufficiently large and straight streamlines can be observed.

There is no simple rule of thumb to determine the required length of the in- and outlet sections because it depends both on the ratio length/pore-diameter ($^{L}/_{D}$), the flow velocity and the permeability of the microstructure. Samples with very low permeabilities will have higher flow velocities in the microstructure, which will require larger outlet sections. From experience the inlet section can be shorter than the outlet section and a practicable way for microstructures with low porosities is to use an $^{L}/_{D}$-ratio of 20 for the outlet-section.

The results of the computation are the pressure distribution and the flow field in the microstructure. In the calculation periodic boundary conditions were applied (see Chapter 4.2) at the lateral boundaries, which leads to $\frac{\partial p}{\partial x} = \frac{\partial p}{\partial y} = 0$ for a flow in z-direction. Therefore, Darcy's

Equation (3.21) can be simplified to

$$\begin{pmatrix} \langle u_x \rangle \\ \langle u_y \rangle \\ \langle u_z \rangle \end{pmatrix} = \frac{1}{\mu} \begin{pmatrix} k_{xx} & k_{xy} & k_{xz} \\ k_{yx} & k_{yy} & k_{yz} \\ k_{zx} & k_{zy} & k_{zz} \end{pmatrix} \begin{pmatrix} 0 \\ 0 \\ \frac{\partial p}{\partial z} \end{pmatrix}. \tag{5.16}$$

This yields three equations for the three unknown permeability-tensor components:

$$\langle u_x \rangle = \frac{k_{xz}}{\mu} \frac{\Delta p_z}{\Delta L_z} \qquad \langle u_y \rangle = k_{yz} \frac{1}{\mu} \frac{\Delta p_z}{\Delta L_z} \qquad \langle u_z \rangle = \frac{1}{\mu} k_{zz} \frac{\Delta p_z}{\Delta L_z}, \tag{5.17}$$

where $\langle u_i \rangle$ is the superficial velocity in the x, y or z-direction, Δp_z is the pressure drop in z-direction and ΔL_z is the length of the microstructure in this direction.

The pressure drop is evaluated as the difference between the area weighted averages of the pressure at the beginning and the end of the microstructure. The superficial velocities are extracted from the flow field by [4]:

$$\langle u_x \rangle = \epsilon \cdot \begin{pmatrix} u_x \\ u_y \\ u_z \end{pmatrix} \cdot \begin{pmatrix} 1 \\ 0 \\ 0 \end{pmatrix} \qquad \langle u_y \rangle = \epsilon \cdot \begin{pmatrix} u_x \\ u_y \\ u_z \end{pmatrix} \cdot \begin{pmatrix} 0 \\ 1 \\ 0 \end{pmatrix} \qquad \langle u_z \rangle = \epsilon \cdot \begin{pmatrix} u_x \\ u_y \\ u_z \end{pmatrix} \cdot \begin{pmatrix} 0 \\ 0 \\ 1 \end{pmatrix}, \tag{5.18}$$

where ϵ is the porosity. It is noted [4], that in reality sometimes a part of the fluid is immobile, which can occur when adhesion plays a role or when the porous matrix contains a large number of dead-end pores. In this cases it is suggested to define an effective porosity $\epsilon_{eff} < \epsilon$. An exemplary comparison between the superficial velocities of an ideal and a real microstructure and the corresponding implications are discussed in more detail in Chapter 6.2.1.

In order to obtain the entire permeability tensor three calculations, one for each direction (x,y,z) of the same geometry, have to be carried out. Each time the in- and outlet sections have to be long enough and the lateral boundaries have to be periodic in order to simplify the set of equations as shown in Equation (5.16). If the calculated pressure drop shows a non-linear behaviour, the same routine as with Darcy's law can be applied to the Forchheimer

Equation (3.19) to determine the permeability and the Forchheimer term in one calculation.

5.3.2 Evaluation of the scaling factor for the effective diffusion coefficient

The determination of the scaling factor allows a detailed assessment of the mass-transport in the microstructure. The scaling factor defined in Equation (3.71) is used to take the influence of the inhomogeneous microstructure on the diffusional mass-transport into account by scaling the binary diffusion coefficient.

One way to determine the scaling factor is to solve a diffusion equation, either Fick or Maxwell-Stefan for binary gases. Therefore, any numerical method, e.g. Computational Fluid Dynamics (CFD) with the finite volume method, the Lattice Boltzmann Method (LBM) or the finite element method can be applied. The effects of the microstructure are incorporated into the model through the geometry of the pores. Although this is a straightforward approach attention has to be paid to the correct application of the lateral boundary conditions. This should be, as far as possible, periodic boundary conditions to minimise dead-end pores. The pros and cons of this application is discussed in more detail in Chapter 4.2 and its correctness is shown in Chapter 6.2.

Inserting Fick's model (3.42) into the species conservation equation (3.23) yields:

$$\frac{\partial(\rho w_i)}{\partial t} + \nabla \cdot (\rho w_i \boldsymbol{u}) + \boldsymbol{\nabla} \cdot (-\rho \mathscr{D}_{ij} \boldsymbol{\nabla} w_i) = s_{w_i}. \tag{5.19}$$

The aim is to determine the scaling factor for the binary diffusion coefficient, with the following assumptions to be made: only steady-state will be evaluated; no source-terms are anticipated; and no convection occurs. Thus Equation (5.19) simplifies to a Laplacian equation:

$$\boldsymbol{\nabla} \cdot (-\rho \mathscr{D}_{ij} \boldsymbol{\nabla} w_i) = 0. \tag{5.20}$$

Equation (5.20) is solved using the finite volume method implemented in *OpenFOAM*: The

volume integral over the cell volume V_p is converted into a summation over all face areas S_f of the cell volume with the *Gauss*-theorem:

$$\int_{V_p} \boldsymbol{\nabla} \cdot (-\rho \mathscr{D}_{ij} \boldsymbol{\nabla} w_i) \, \mathrm{d}V = \sum_f \boldsymbol{S}_f \, (-\rho \mathscr{D}_{ij} \boldsymbol{\nabla} w_i) = 0. \tag{5.21}$$

The result is the distribution of the mass fraction w_i. With this knowledge, the averaged local flux ϕ across the boundary surface S can be calculated:

$$\int_S \phi \, \mathrm{d}S = \int_S -\rho \mathscr{D}_{ij} \boldsymbol{\nabla} w_i \boldsymbol{n} \mathrm{d}S, \tag{5.22}$$

where $\boldsymbol{n}$ is the normal vector of the faces S and ϕ is the mass flux through the microstructure. This value can be compared to the analytical solution of Fick's diffusion equation (3.64):

$$f = \frac{\int_S -\rho \mathscr{D}_{ij} \boldsymbol{\nabla} w_i \boldsymbol{n} \mathrm{d}S}{-\rho \mathscr{D}_{ij} \frac{\Delta w_i}{L}}. \tag{5.23}$$

Δw_i in the denominator is calculated as the difference of the weighted average of the mass fraction at the top and bottom surfaces, normal to the main diffusion path. Not only the type of the lateral boundary conditions influences the results, but also the boundary conditions (Dirichlet, Neumann) at the top and bottom surfaces. As proposed in [55] the following boundary conditions are applied and a similar tendency is observed and reported in [78]:

- Two fixed mass fractions on the top and bottom boundaries (Dirichlet) result in the lowest tortuosity value.
- Two fixed fluxes on the top and bottom boundaries (Neumann) yield the highest tortuosity value.
- The tortuosity value obtained with a fixed mass fraction on the top and a defined flux on the bottom boundary lies between the above approaches.

The last approach with one fixed mass fraction and a defined flux resembles the physics in the SOFC most adequately, although the first approach is more stable in numerical terms. With

the obtained scaling factor f the tortuosity can be calculated:

$$\tau = \sqrt{\frac{\epsilon}{f}}. \tag{5.24}$$

In order to determine the scaling factor, basically any Laplacian equation can be solved. This could be the Maxwell-Stefan equation, but also an electrostatic equation [46] can be applied, where the gas in the pores is assigned a fictive conduction value, or a simple heat conduction equation could be solved.

5.3.3 Evaluation of the scaling factor with corrosion

The corrosion model presented in Chapter 5.1.1 is capable of determining the change of the porous volume due to growth of the oxide scale. The decreased porosity will influence the mass-diffusion in the microstructure. The corrosion and diffusion mechanisms take place at different time-scales. While the growth of the oxide usually takes several hours, the diffusion occurs in seconds. The aim of the computation should be the determination of the mass-transport after 40 000 h, in which case time-steps in the order of seconds would be inappropriate. It is therefore assumed, that the diffusion is quasi steady-state, while the transient corrosion equations are solved. After a certain time-span, and an quantifiable change of the microstructure, the diffusion equations are solved and a new species concentration is evaluated.

In order to take the changes of the microstructure into account and to determine their effects on the scaling factor some extensions to the previously discussed equations have to be made, which is also presented in [77]. Namely, the additional porosity due to corrosion ϵ_{corr} has to be incorporated in Equation (5.20):

$$\boldsymbol{\nabla} \cdot (-\rho \mathscr{D}_{ij} \epsilon_{corr} \boldsymbol{\nabla} w_i) = 0. \tag{5.25}$$

As a reminder: the corrosion porosity ϵ_{corr} is 0 in regions that are fully corroded and 1 where no oxide is prevailing. This definition induces severe numerical problems as Equation (5.25)

will become zero at certain points. The numerical solution of Equation (5.25) involves the creation of a system of linear algebraic equations which are obtained by numerical methods. These equations are written in matrix formulation and solved using special matrix solvers.

$$\boldsymbol{A}\boldsymbol{x} = \boldsymbol{b}. \tag{5.26}$$

The matrix $\boldsymbol{A}$ contains the diagonal and off-diagonal elements of each volume cell and its neighbours. The vector $\boldsymbol{x}$ would equal the mass-fraction distribution and the vector $\boldsymbol{b}$ contains explicit terms, as well as boundary and initial conditions. As soon as the diagonal elements of the matrix $\boldsymbol{A}$ becomes zero, as in the case of $\epsilon_{corr} = 0$, a division by zero causes a floating point exception. Therefore, special treatment has to be applied to regions where the corrosion porosity equals 0.

In a first step the minimum corrosion porosity value is set to 1×10^{-10} to avoid division by zero. In addition to that, the matrix is manipulated so that previously zero diagonal elements become $\neq 0$. This is done in a way that the solution of the algebraic system still results in a zero mass-fraction in these cells. Furthermore, a special interpolation scheme is used, which interpolates the cell volume values to the faces. The interface between the oxide and the pores is very steep (from 1×10^{-10} to 1 in the worst case). Standard linear interpolation may not represent this effect correctly. Therefore, a harmonic interpolation scheme is used, where the reciprocal of the interpolation of 1/value is returned. Thus the lower value contributes more to the interpolated value.

In addition to Equation (5.25) also the calculation of the mass-diffusion flux is influenced by the corrosion porosity:

$$\int_S \phi \, \mathrm{d}S = \int_S -\rho \mathscr{D}_{ij} \epsilon_{corr} \boldsymbol{\nabla} w_i \boldsymbol{n} \mathrm{d}S, \tag{5.27}$$

and finally the scaling factor can be evaluated by comparing the computed flux in the microstructure with the analytical solution of the Fick equation for binary gases:

$$f = \frac{\int_S -\rho \mathscr{D}_{ij} \epsilon_{corr} \boldsymbol{\nabla} w_i \boldsymbol{n} \mathrm{d}S}{-\rho \mathscr{D}_{ij} \frac{\Delta w_i}{L}}. \tag{5.28}$$

Chapter 6

Validation

In this chapter the validation of the corrosion (Chapter 6.1) and the mass-transport models is presented. The focus is laid on the determination of a permeability tensor (Chapter 6.2.1), the correct implementation of the diffusion equations with the consideration of convective transport (Chapter 6.2.2) and the determination of a scaling factor for an effective diffusion coefficient (Chapter 6.2.3).

6.1 Corrosion model

Several test cases were set up to validate the corrosion model and parts of the results were already published in [77].

6.1.1 One-dimensional growth

The first computation was carried out on a flat plate, where the oxide grows only in one direction. An arbitrarily chosen k_p-value of $2.22 \times 10^{-18}\,\mathrm{m^2\,s^{-1}}$ was used for the calculation, which is in the range of values reported by [3] for the formation of chromia in an oxygen atmosphere at 700 °C.

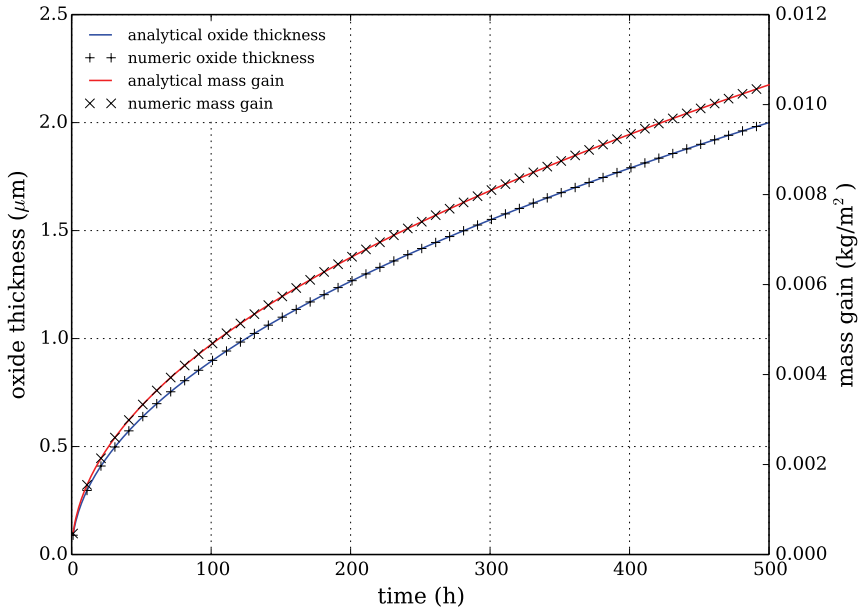

Figure 6.1: The simulated and theoretical oxide thickness and mass gain for a simple test geometry with oxide growth only in one direction [77].

The computed oxide thickness and the mass gain are compared to the 1-D parabolic rate law (Equation (3.4)). In the simple test cases only the parabolic growth was simulated. The results are plotted in Figure 6.1. A perfect agreement between simulation and theory can be seen for both, the oxide thickness and the mass gain, which demonstrates the correct implementation of the model.

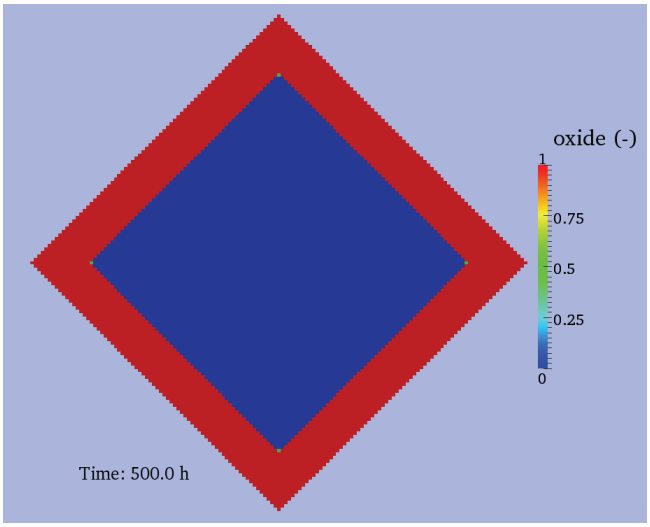

Figure 6.2: Rotated square with an edge length of 10 µm, where the edges are represented by stair steps. The oxide thickness after 500 h is shown.

6.1.2 Growth correction for voxel geometries

In more complex geometries it is unavoidable that the original surfaces are approximated by voxels, which will lead to an overestimation of the surface (see Chapter 4.4) and a faster growth of the oxide if one computational cell is corroding from more than one side. A growth correction factor κ has been introduced in Chapter 5.1.1 that accounts for this higher growth rate. The geometry together with the computed oxide is shown in Figure 6.2, where a cube with an edge length of 10 µm is rotated by 45°, so that the edges are represented as stair-steps.

The computed oxide thickness with and without the growth correction is plotted in Figure 6.3. The voxel length is 0.1 µm and each time one cell layer is filled the oxide jumps. In the case of no growth correction this error sums up and is about 10 %. The growth correction slows down the growth of the oxide so that it balances the jumps and only a small difference (∼1 %) between the computed oxide thickness and the 1-D growth can be discerned.

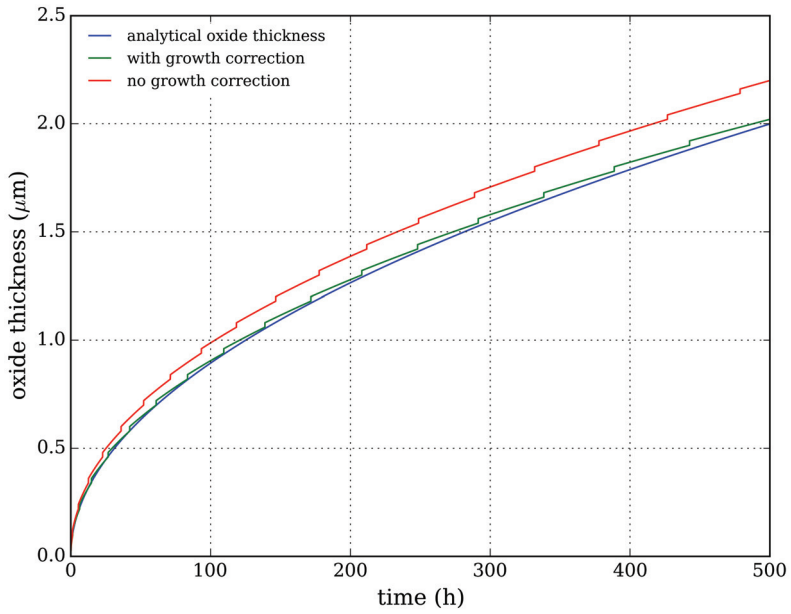

Figure 6.3: Comparison of the oxide thickness for the square geometry shown in Figure 6.3 computed with and without the growth correction and the 1-D growth.

6.1.3 Growth on convex and concave surfaces

In a further step a geometry was created representing a ring with a diameter of 10 µm. Two cases were calculated: Firstly, the convex case, where the oxide grows outward, and secondly, the concave case, where the oxide grows inward. A result of the two test cases with the oxide distribution is shown in Figure 6.4. The parabolic rate constant is the same as in the one dimensional case. The black ring in the middle of the red oxide is the initial surface. Note: the position of this initial surface is not changed during the calculation, but the metal-retraction is stored at the boundary faces. Fully corroded regions are coloured red. In this region no diffusion can occur and the corrosion porosity ϵ_{corr} is zero. In the blue regions no oxide is hindering the mass transport.

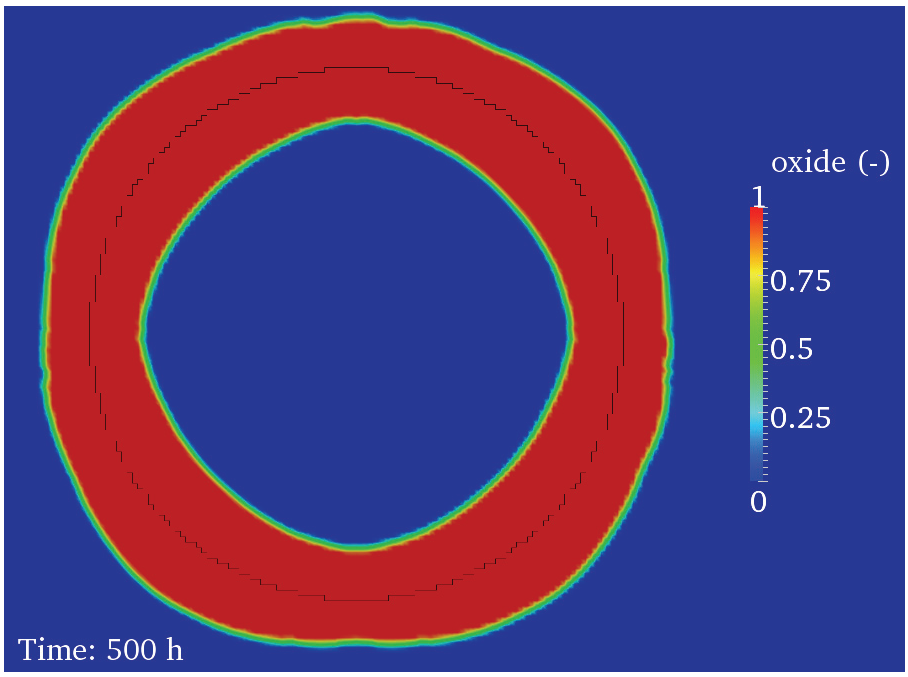

Figure 6.4: Oxide growth on a simple geometry representing a ring with a diameter of 10 µm, which is discretized using equidistant voxel with a volume of 1×10^{-21} m^3. Fully corroded areas are coloured red, while in the blue regions no oxide is prevailing. The inner part of the ring is referred to as concave, while the outer part is convex. Note: The metal-retraction is only calculated and stored at the boundary faces (in this case the initial ring (black)), with no change of the initial geometry [77].

The comparison between the average thickness computed by the corrosion algorithm and the 1-D parabolic thickness is shown in Figure 6.5. Several conclusions can be drawn from this result: Firstly, the oxide thickness in the concave case is slightly higher compared to the convex. This means, that the oxide grows slightly faster inward than outward because the diffusion paths of

the Cr-ions are shorter in the concave (inward) case and therefore the oxide can grow faster. Secondly, the results show a good agreement with the 1-D parabolic rate law.

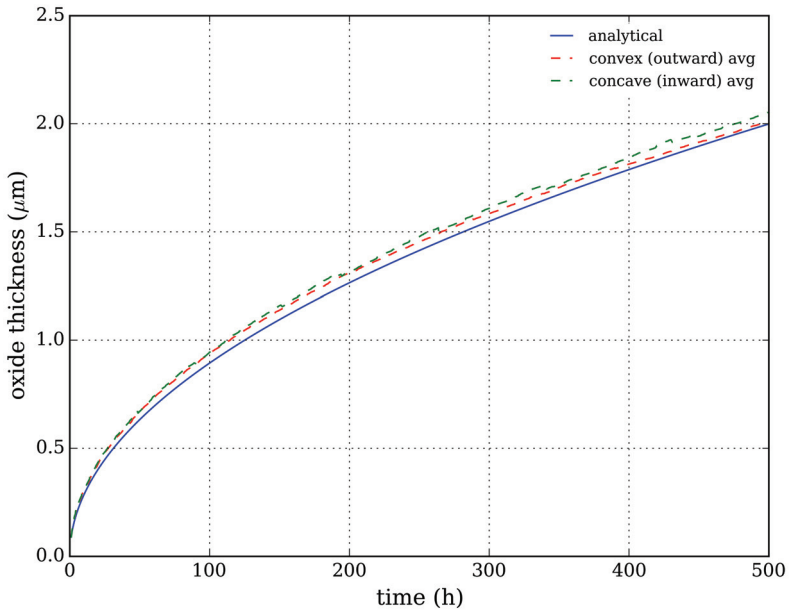

Figure 6.5: Comparison of the oxide thickness between a concave (inward) and a convex (outward) geometry. Only a slight difference of the average oxide layer thicknesses between the concave and convex curvature can be discerned and a good agreement with the 1-D parabolic rate law is achieved [77].

In order to illustrate the influence of the growth limitation and correction described and presented in Chapter 5.1.1, the corrosion on the same geometries was recalculated with the same algorithm, but without the limitation and growth correction. That means, that the oxide can grow unaffected of geometric features. The result in Figure 6.6 shows that in the case without the limitation the oxide thickness in both geometries is highly overestimated compared to the 1-D solution.

Clearly, in a geometry with edges, where the oxide can grow from several directions the oxide will form more rapidly than expected. This deviation originates in the implementation of the corrosion model, which is reported here again for an easier understanding:

$$x_{corr}^{new} = \sqrt{\left(x_{corr}^{old}\right)^2 + \frac{k_p \Delta t}{n}\kappa}. \tag{6.1}$$

The additional thickness of the oxide $k_p \Delta t$ is limited by the factor n, which is the number of corroding faces that get their Cr-ions from one retracting face. An example sketch is shown in

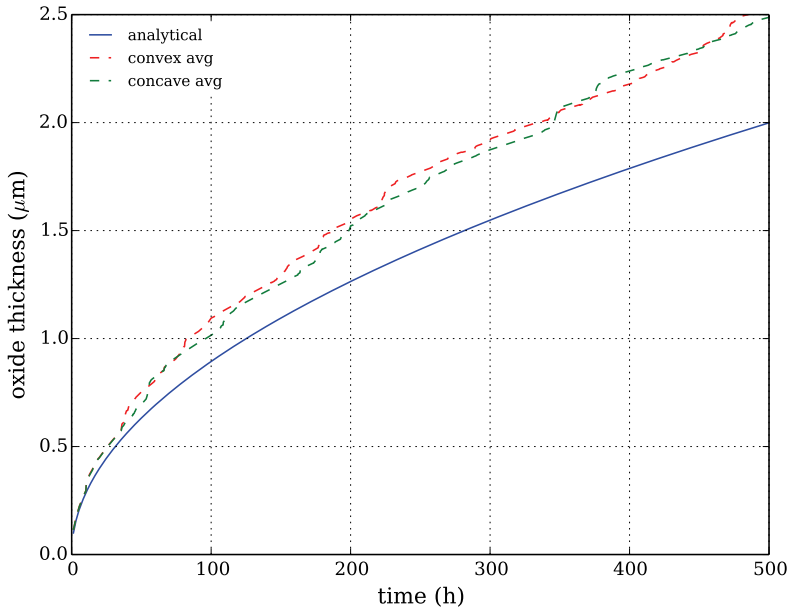

Figure 6.6: Calculated oxide thickness of the concave (inward) and convex (outward) geometry without the growth limitation. Both cases overestimate the analytical oxide thickness.

Figure 5.1(c), where two corroding faces (dark red) are linked to one retracting face (green). In order to conserve the flux of Cr-ions, the growth of the oxide is evenly distributed amongst the corroding faces. This leads to a slower oxide growth in geometries with many edges. However, this effect is overlapped by the fact that many computational cells corrode from more than one side which increases the growth rate. To account for these effects the growth correction factor κ was introduced.

The mass gain due to corrosion is determined by summing up the local oxide growth and relating this mass to the initial surface. The result is plotted in Figure 6.7 and one interesting finding is the difference between the mass gain in the concave (inward) and convex (outward) geometry. This can be explained by the fact that the additional mass in both cases is related to the same initial surface area (see Equation (5.12)). During the growth of the oxide the current available surface for the corrosion increases in the convex (outward) case and decreases in the concave (inward) case. And although the oxide thickness is smaller in the convex case (see Figure 6.5), a larger volume has to be filled and the mass gain has to be higher. As expected, the 1-D parabolic mass-gain lies in between the convex and concave growth, as shown in Figure 6.6.

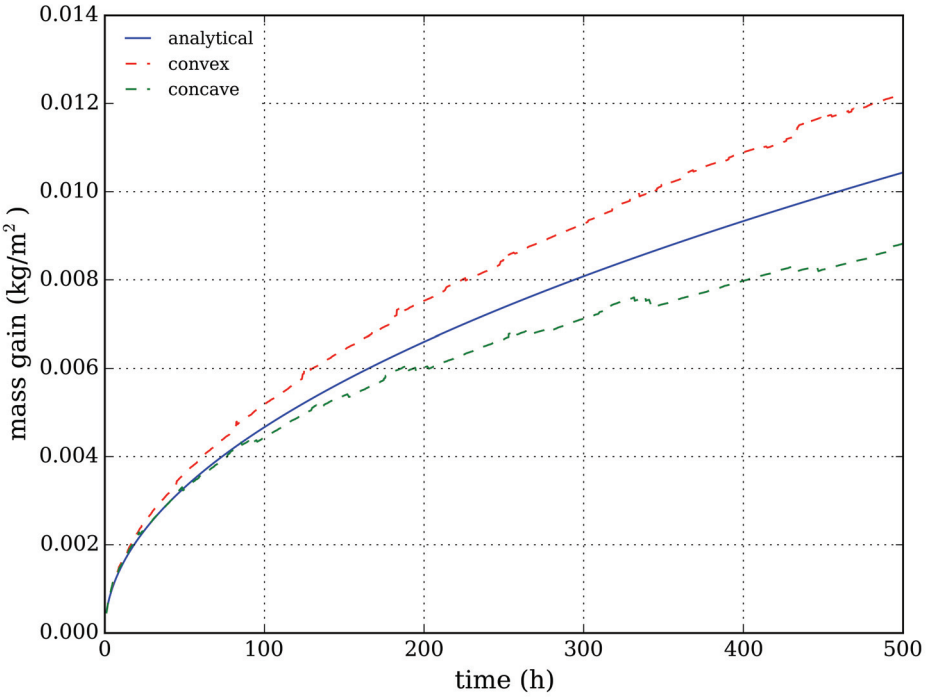

Figure 6.7: Computed and theoretical mass gain of the concave (inward) and convex (outward) geometry [77].

6.1.4 Comparison to micro-graphs

So far the principle functionality of the corrosion algorithm, e.g. correct determination of the mass gain, could be validated on simple geometries. The focus now shifts to the question, whether the algorithm is capable of distributing the oxide correctly. For this purpose corroded metallic supports were analysed by SEM (special thanks to Åsa Persson from DTU Copenhagen for the measurements). One micro-graph of the metallic support after 500 h at 850 °C in simulated anode outlet gas (an $Ar/H_2/H_2O$ atmosphere with $p_{H_2O}/p_{H_2} = 9$) is shown in Figure 6.8(a), where the light grey areas show the metal, the dark grey areas indicate the oxide and the black areas are the remaining open pore space. In order to achieve a direct comparison between measurement and simulation the micro-graph was used as input for the reconstruction algorithm described in Chapter 4.2, and a 2-D computational geometry was created. The simulated corroded metallic support in Figure 6.8(b) shows the oxide in red and the pores in blue. The oxide is evenly distributed in the simulation, and on average a good agreement between measured and computed oxide thickness can be seen.

However, two differences are apparent. Firstly, in the middle left pore in Figure 6.8(a) a much thinner oxide can be discerned. This may indicate spallation of the oxide, or comes from the polishing prior to the measurement where the oxide may be damaged. In any case, effects like spallation are not included in the corrosion model because of the lack of an appropriate model to determine the spallation, and the fact that as soon as spallation occurs the corrosion is so far advanced that the functionality of the fuel cell is questionable.

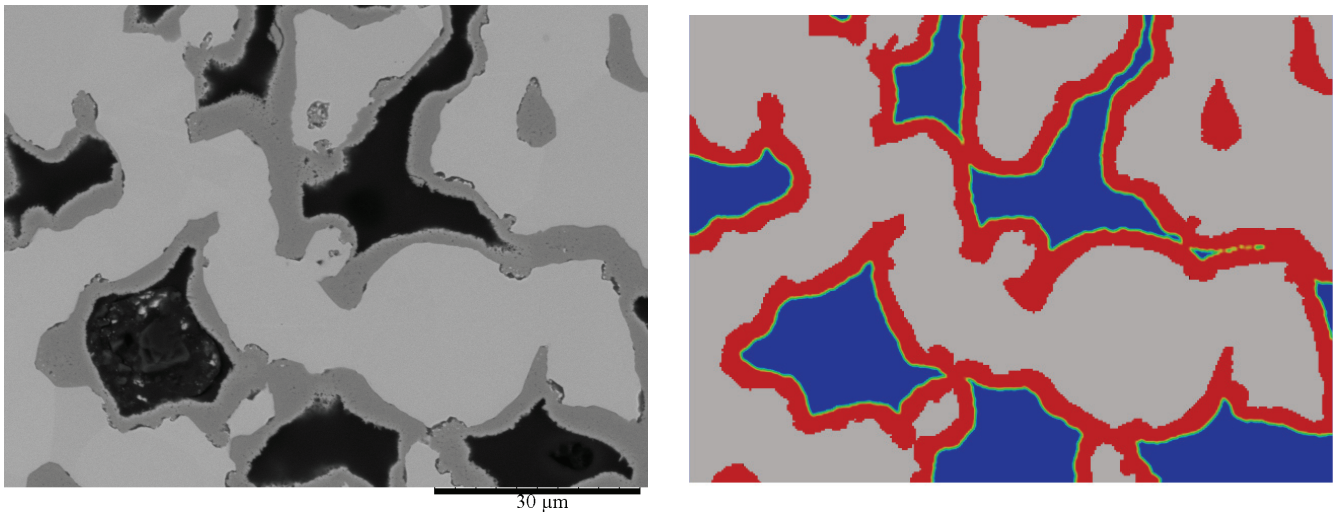

(a) SEM picture of corroded metallic support

(b) Corresponding reconstruction and computed corrosion

Figure 6.8: Comparison between the corrosive scale of a metallic support SEM and the computational result thereof. The dark grey and the red areas indicate the measured and the computed oxide [77].

The second difference becomes obvious at regions that have a much thicker oxide. This deviation can be explained by the fact that the measurement resembles the corrosion in 3-D, while the simulation is based only on a 2-D geometry. Therefore, effects from the curved geometry in the third dimension are not taken into account in the simulation. However, the algorithm is capable of determining different thick oxides provided that the geometry is 3-D. Figure 6.9 shows a 2-D slice of a full 3-D reconstructed metallic support. Here only the pores are depicted, where dark blue regions correspond to the open pore volume and red regions are fully corroded. The colour bar indicates the oxide: 1 (red) $\rightarrow$ fully corroded; 0 (dark blue) $\rightarrow$ no oxide. It is evident that the oxide thickness varies, as it was seen before in the SEM micro-graph. The correct distribution of the oxide is thus validated.

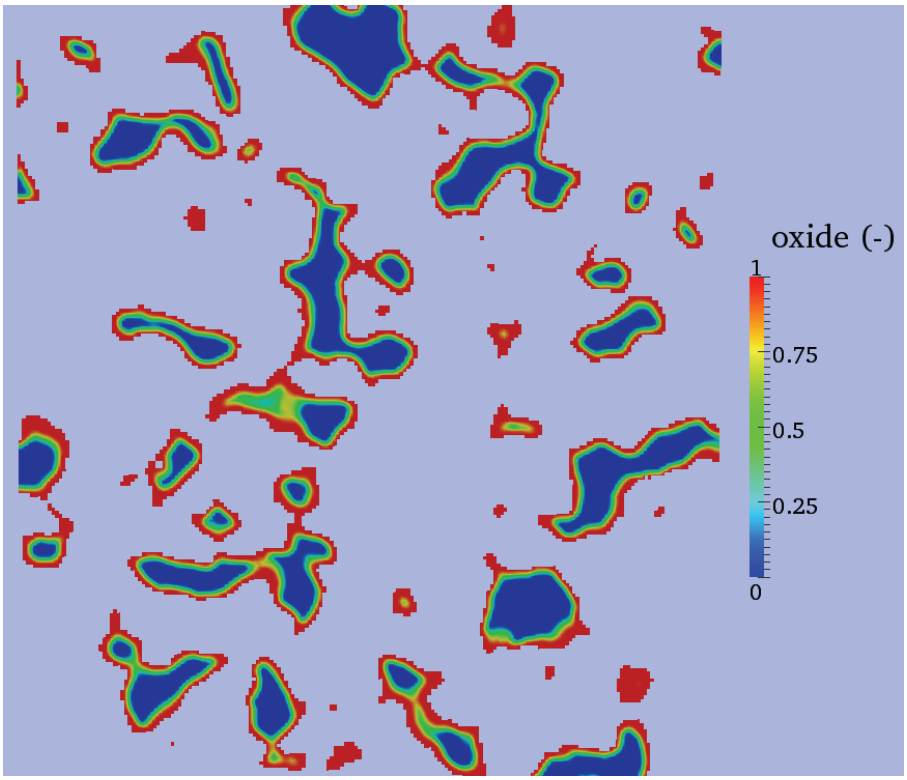

Figure 6.9: 2-D slice showing the computed oxide of a full 3-D metallic support after 40 000 h at 850 °C in simulated anode gas with $p_{H_2O}/p_{H_2} = 9$. Here only the pores are shown. Red indicates fully corroded areas, while blue areas have got no oxide [77].

6.1.5 Comparison to mass-gain measurement of metal-support

In a final step the computed mass gain of the reconstructed metallic supports is compared to the measured mass gain of the actual corroded samples. The measured mass gain data of two samples in 650 °C is used. A least-square fit was implemented in a *python* program using the package *SciPy* [80]. The fitted parabolic rate constant $k_{p,e}$ was determined to be $1.61 \times 10^{-21}\,\mathrm{m^2\,s^{-1}}$. $k_{p,e}$ denotes the parabolic rate constant, if only parabolic kinetics are assumed. As explained in Chapter 3.1.1 the corrosion in the initial step often follows linear kinetics. This can also be observed in Figure 6.10 where the red lines show the mass gain of measured samples. In the initial regime, clearly linear kinetics can be observed, why the data is split into a linear and a parabolic set. Due to the coarse measurement (every 250 h) the transition between the linear and the parabolic regime was set to 300 h. Each data-set is fitted to the corresponding 1-D model and the rate constants are as follows: a linear rate constant k_l $=8.83 \times 10^{-14}\,\mathrm{m\,s^{-1}}$ for the fast initial corrosion and a parabolic rate constant k_p $=1.30 \times 10^{-21}\,\mathrm{m^2\,s^{-1}}$ for the subsequent slower corrosion.

These values are used as input parameters in the corrosion model and the comparison between the measurement data and the different model approaches is shown in Figure 6.10. The pure parabolic approach with the rate constant $k_{p,e}$ shows a poor agreement in the beginning and only after 3000 h a convergence can be observed. Nevertheless, the slope seems to be too steep so that the corrosion may be overestimated at later time steps. On the contrary, the more elaborated model with a linear start and subsequent parabolic kinetics shows very good agreement with the measurement and a reliable validation is obtained.

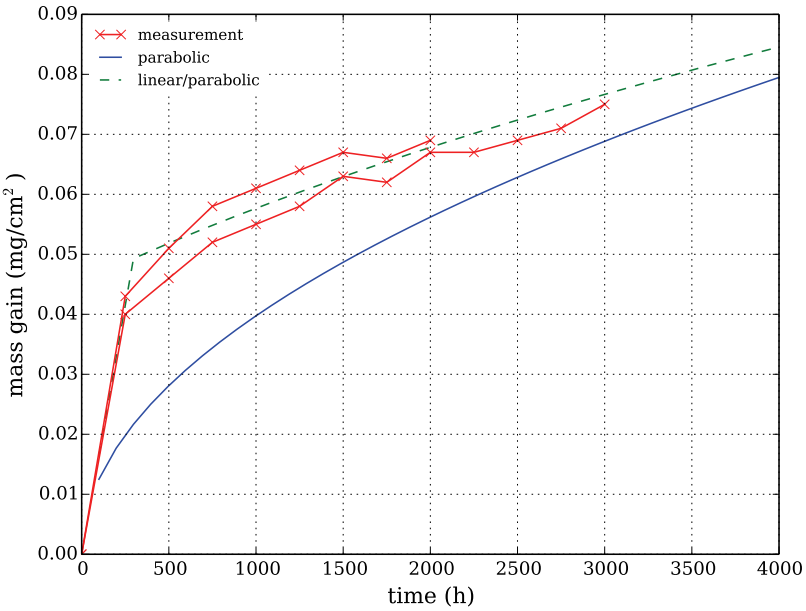

Figure 6.10: Measured and computed mass gain of a metallic support at 650 °C. The linear combined with the parabolic approach shows a very good agreement, while the sole parabolic approach underestimates the mass gain in the beginning and shows a faster growth in the end.

In conclusion, the corrosion model was validated with simple geometries, as well as on real reconstructed microstructures. The agreement of overall parameters like the mass gain was satisfying and also the distribution of the oxide corresponds to measurements. However, the limitations of the models lie in the assumption that the oxide is perfectly adherent and does not spall. Thermal stresses during thermal cycling might cause cracks in the oxide, which will increase the oxidation. Nevertheless, a reliable tool was developed which is capable of predicting the microstructural changes due to corrosion and assess its influence on the mass transport.

6.2 Mass transport

6.2.1 Permeability

The first interesting question that has to be answered when determining the permeability tensor is how to compute the superficial velocities in the microstructure. The result of the solution of the Navier-Stokes equations (5.13) is the actual velocity in the microstructure. It was shown in [4] that the relation between the superficial velocity $\langle \boldsymbol{u} \rangle$ and the actual velocity $\boldsymbol{u}$ is related via the porosity ϵ:

$$\langle \boldsymbol{u} \rangle = \epsilon \boldsymbol{u}. \tag{6.2}$$

It was reported in [66] that Equation (6.2) holds only true if the effective porosity is used, which excludes all isolated pores. This important fact can be observed in Figure 6.11, where the superficial velocity in a real microstructure is plotted over the bulk velocity. The bulk velocity equals the velocity in the inlet section and the superficial velocity is calculated from the actual velocity in the microstructure according to Equation (6.2). In the ideal case the bulk and the superficial velocities should be the same (continuous line). In reality, deviations can be observed that are higher at higher velocities (dashed line). It is therefore advisable to limit the evaluation to a velocity range, where the deviations are negligible.

The measurements carried out at DTU (special thanks to Peter Blennow) were done on a different, slightly more open metallic support than the reconstructed metallic support used in this study. Although not completely comparable the range of permeabilities is reported here to have at least a rough estimation: $k_{measured} = 1 \times 10^{-13}\,\mathrm{m}^2$. Due to the denser structure of the investigated metallic support the permeability along the main diffusion path is assumed to be in the range of $2 \times 10^{-13}\,\mathrm{m}^2$ to $2 \times 10^{-14}\,\mathrm{m}^2$ [8]. The computed permeability in the same direction is $3.2 \times 10^{-14}\,\mathrm{m}^2$ and within the expected range. Nevertheless, the permeability tensor of the

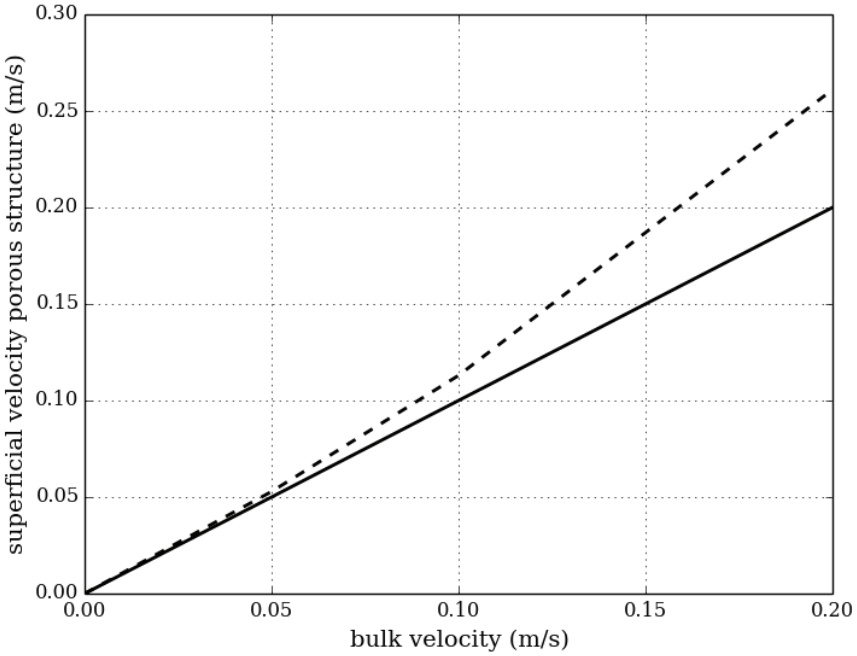

Figure 6.11: Comparison between the bulk and the superficial velocity in the microstructure. In an ideal microstructure both velocities are the same, but in real microstructure deviations can be observed.

real metallic support microstructure was not symmetric:

$$\boldsymbol{k}_{ij} = \begin{pmatrix} 5.52 \times 10^{-14} & -4.69 \times 10^{-15} & -1.20 \times 10^{-15} \\ -9.04 \times 10^{-16} & 4.56 \times 10^{-14} & 1.69 \times 10^{-15} \\ -2.28 \times 10^{-15} & 5.30 \times 10^{-15} & 3.18 \times 10^{-14} \end{pmatrix} \tag{6.3}$$

It was assumed that this deviation may come from the fact that only ∼17 % of the lateral boundary are periodic (see Chapter 4.2) and this factor varies depending on the main flow in x, y or z direction. Note: In order to calculate a full permeability tensor three individual calculations in three directions have to be carried out (see Chapter 5.3.1).

The verification of this assumption was carried out on an artificial geometry. It consists of straight pores with defined diameter and distance between the pores. Here, it is possible to obtain 100 % periodic boundaries in all three directions. The creation of the geometry is described in more detail in Chapter 4.5. The overall dimensions of the artificial geometry are 222 µm × 286 µm × 213 µm, with a pore diameter of 10 µm and a distance of 20 µm. The inclination vector of the pores is $(-0.8, -0.6, 1)$ and a porosity of 0.261 is determined. The

pressure drop is calculated for all three directions with three individual calculations and the computed permeability tensor $\boldsymbol{k_{ij}}$ has the form:

$$\boldsymbol{k}_{ij} = \begin{pmatrix} 2.45 \times 10^{-10} & 1.81 \times 10^{-10} & -3.01 \times 10^{-10} \\ 1.81 \times 10^{-10} & 1.37 \times 10^{-10} & -2.25 \times 10^{-10} \\ -3.01 \times 10^{-10} & -2.26 \times 10^{-10} & 3.80 \times 10^{-10} \end{pmatrix}. \tag{6.4}$$

The difference of the off-diagonal elements is less than 0.2 %, and the tensor is symmetric as expected in theory. Using the linear algebra package that comes with *SciPy* the eigenvectors and eigenvalues can be calculated:

$$\text{eigenvectors} : \begin{pmatrix} -0.566 & -0.683 & -0.347 \\ -0.423 & -0.241 & 0.901 \\ 0.707 & -0.690 & 0.261 \end{pmatrix} \qquad \text{eigenvalues} : \begin{pmatrix} 7.56 \times 10^{-10} \\ 4.25 \times 10^{-12} \\ 2.22 \times 10^{-12} \end{pmatrix} \tag{6.5}$$

The eigenvectors define a new, rotated coordinate system in the principal direction of the flow. Calculating the normalised inclination vector, which was the input for the creation of the artificial geometry, yields:

$$\begin{pmatrix} -0.566 \\ -0.424 \\ 0.707 \end{pmatrix}, \tag{6.6}$$

which is equal to the first column eigenvector in Equation (6.5). Thus, one direction of the rotated coordinate system is equal to the defined inclination vector, and the others are orthogonal to this direction. The permeabilities in this new coordinate system are defined by the corresponding eigenvalues in Equation (6.5). Interestingly, the permeability in this new x-direction is by two orders of magnitude higher compared to the other directions, which is obvious as the x-direction of the rotated coordinate system is parallel to the pores and thus the convective flow is less hindered. The result of one computation on the artificial geometry is shown in Figure 6.12, where the pressure drop is depicted together with a vector plot of the velocity. The inlet velocity was $0.1\,\mathrm{m\,s^{-1}}$ and the in- and outlet section was 100 µm each.

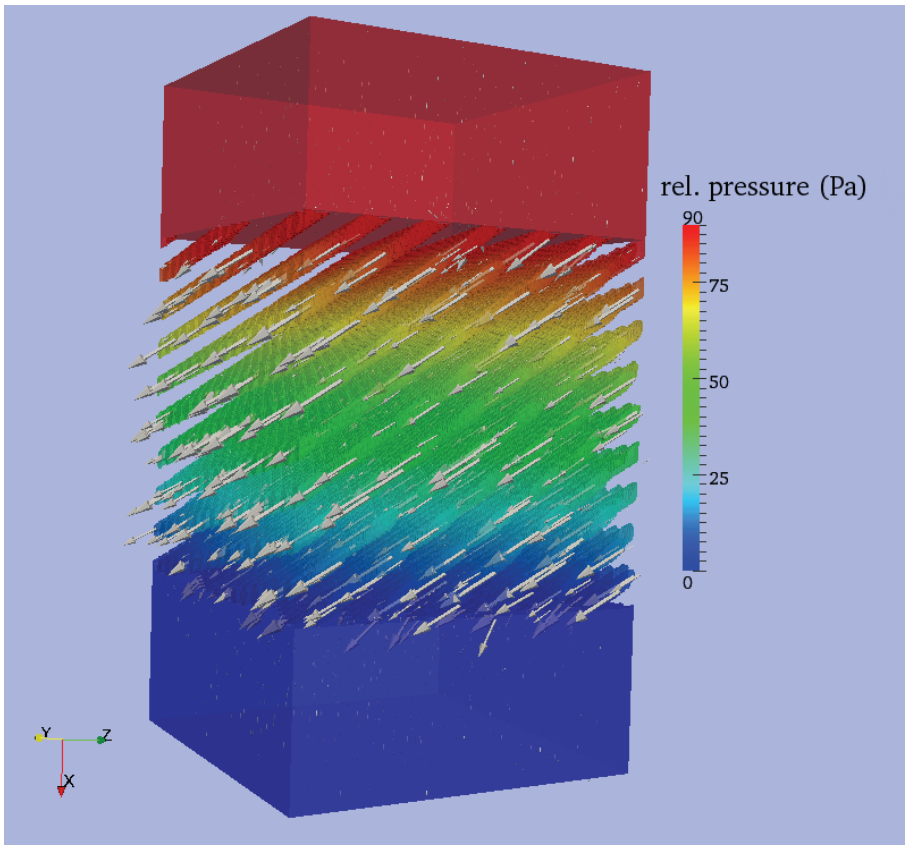

Figure 6.12: Pressure drop in the artificial geometry together with a vector plot of the velocity. The dimensions of the microstructure are 222 µm × 286 µm × 213 µm, with a 100 µm long in- and outlet section.

The deviation of the off-diagonal elements of the permeability tensor calculated for the real microstructure originates from the fact that in reality the microstructure will never be 100 % periodic. In this case only an average periodicity of 17 % could be achieved. This means that the effective area, where the fluid can leave and enter the geometry, varies in the three computations. While the fluid can access the entire area in the flow direction because of the in- and outlet section, only the periodic areas are available for the flow at the lateral boundaries. As the in- and outlet sections change in the three required calculations, also the available areas change and thus the superficial velocities, which explains the different off-diagonal elements in the permeability tensor in Equation (6.3).

6.2.2 Diffusion

The importance of the correct implementation of the Maxwell-Stefan model including the influence of the pressure drop shall be discussed here. The basic theory is given in Chapter 3.2.2.2.

The validation focused on the concentration over-potential caused by diffusion in the microstructure, why an entire, coupled SOFC model for the whole SOFC was not necessary. To simplify the analysis further only binary $H_2 - H_2O$ diffusion was assumed. The molar fraction of hydrogen was fixed to 0.6 at the gas-channel metallic support interface and a periodic boundary condition is applied at the lateral walls (parallel to the diffusion path). The interface boundary between the metallic support and the anode-functional-layer (AFL) is a fixed gradient condition, which depends on the required molar flux of hydrogen N_{H_2} defined by Faraday's law:

$$N_{H_2} = \frac{i}{2F}, \tag{6.7}$$

where i is the current density and F is Faraday's constant.

A higher current density will lead to a higher hydrogen consumption which in turn will lower the molar fraction of hydrogen at the metallic support AFL interface.

The concentration over-potential defined in Equation (2.6) is calculated with and without the pressure driven molar fluxes for different current densities and is plotted in Figure 6.13. As expected, the differences increase with higher current densities due to the higher molar fluxes which induce a larger pressure gradient. This in turn decreases the concentration at the anode and increases the concentration over-potential. Therefore, the influence of the diffusion on the overall cell performance is underestimated if the pressure gradient is neglected.

6.2.3 Effective diffusion coefficient

This section summarises the validation of the evaluation model to determine the effective diffusion coefficient by analysing the results on simple geometries and comparing the computed values of the real microstructure to measurements.

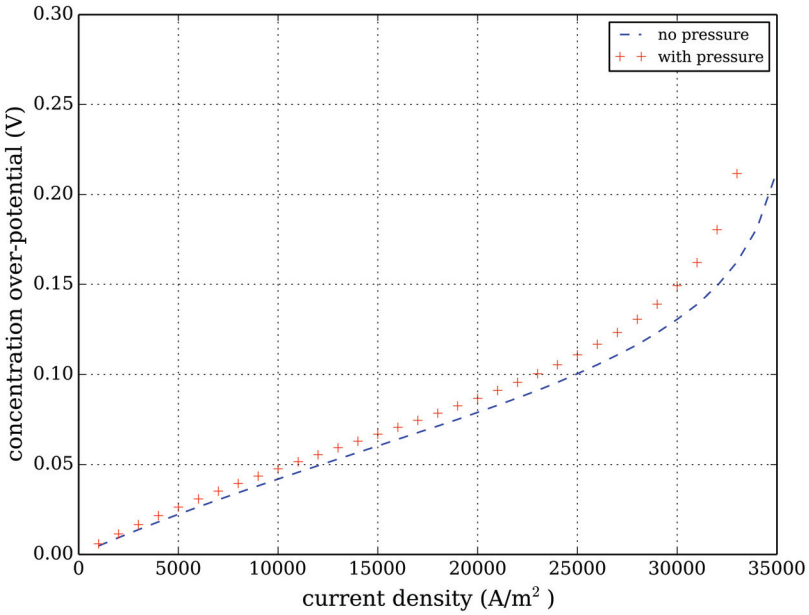

Figure 6.13: Influence of the pressure gradient on the concentration over-potential for the Maxwell-Stefan model.

6.2.3.1 Validation on artificial geometry

Firstly, the results on an artificial geometry are presented. It is the same geometry which was used for the validation of the determination of the permeability tensor described in Chapter 6.2.1. The advantage of such a simple geometry is, that the porosity, as well as the geometrical tortuosity are known. In Equation (3.63) the tortuosity is defined as ratio between the actual pore length and the geometrically shortest length. The latter is determined by the size of the geometry and the actual length L_{eff} can be calculated as the inclination vector is known $\boldsymbol{g}_{in} = (-0.556 \; -0.424 \; 0.707)$ and only straight pores are considered. The pore length in z-direction is:

$$L_{eff} = \frac{L}{g_{in_z}}, \tag{6.8}$$

where g_{in_z} is the z-component of the inclination vector and L is the shortest distance in z-direction (equals the z-length of the geometry). The tortuosity is thus:

$$\tau = \frac{L_{eff}}{L} = \frac{1}{g_{in_z}} = 1.414. \tag{6.9}$$

Table 6.1 summarises the results of various computations with different boundary conditions on the patches. A principal sketch with annotations of the patches and the applied boundary conditions can be found in Figure 6.14, where the main diffusion path is from top to bottom. The lateral walls are either considered to be periodic or symmetry. Symmetry boundaries basically act as walls where no mass flux can occur, while periodic boundaries allow a mass flow out of the geometry which is balanced by a mass flux on the opposite wall. The top and bottom walls, that means the interface between the gas-channel and the metallic support and the interface between the metallic support and the anode-functional-layer, are either set to a fixed value (fixed concentration) or to a fixed gradient (fixed mass flux). The calculated porosity of the artificial geometry is 0.261. The computed scaling factor is the ratio between the binary and the effective diffusion coefficient and is defined in Equation (3.71).

Table 6.1: Comparison between the computed and analytical results of the artificial geometry with different boundary conditions. A sketch explaining the application of the boundary conditions at the different patches is provided in Figure 6.14. The calculated porosity value is 0.261.

top/bottom/lateral patches	scaling factor f	tortuosity factor τ^2	tortuosity τ
fixedValue/fixedValue/periodic	1.14×10^{-1}	2.296	1.515
fixedValue/fixedGrad/periodic	1.15×10^{-1}	2.269	1.506
fixedGrad/fixedGrad/periodic	1.16×10^{-1}	2.241	1.497
fixedValue/fixedValue/symmetry	5.57×10^{-3}	46.890	6.848
fixedValue/fixedGrad/symmetry	9.15×10^{-3}	28.536	5.342
fixedGrad/fixedGrad/symmetry	2.01×10^{-2}	13.016	3.708

Several conclusions can be drawn from the computational results: The most obvious fact is the high deviation between the scaling factor calculated with the periodic and symmetry boundary conditions at the lateral walls. Since a symmetry condition basically blocks the lateral walls, the mass flow through the artificial geometry is much smaller compared to the more accurate periodic approach, for which reason also the scaling factor is smaller. In order to obtain

meaningful results with this approach, the computational geometry has to be large enough to allow enough continuous pores from the top to the bottom. In doing so, the influence of the boundary condition decreases.

The second interesting finding is the influence of the top and bottom boundary conditions on the results. Here the deviations are much smaller compared to the lateral walls and it can be seen that the tortuosity calculated with the two fixed gradients approach is closest to the geometric tortuosity (see Equation (6.9)) with a deviation of ∼5.5 %. The remaining difference may be due to discretisation errors, or due to the voxel representation of the real geometry.

Thirdly, that the correct form of the scaling factor is

$$f = \frac{\epsilon}{\tau^2}, \tag{6.10}$$

contrary to $f = \epsilon/\tau$ as often used in SOFC modelling. This result validates the theoretical derivation of [24] presented in Chapter 3.2.4, and hopefully will guide the way to correct implementations of the effective diffusion coefficient in simulation studies of other researches in the future.

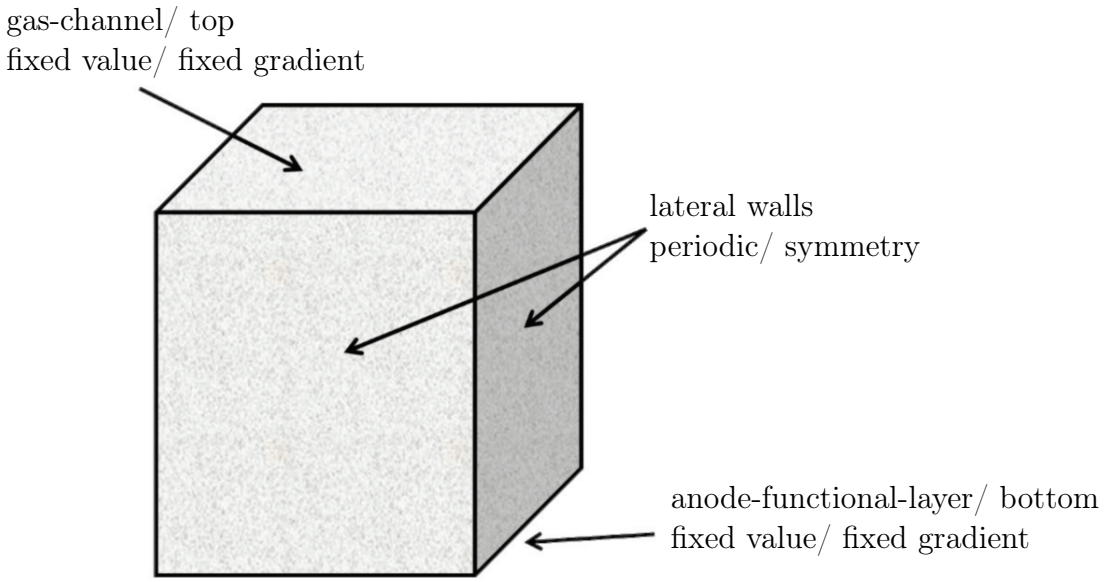

Figure 6.14: Description of the annotation of the patches and applied boundary conditions in the simulation.

6.2.3.2 Validation on real 3-D model

The validation of the evaluation model on a real metallic support microstructure was presented in a concise form in [78] and will now be described in more detail.

One common tool to understand and analyse the complex electrochemical system of an SOFC is the Electrochemical Impedance Spectroscopy (EIS). The measured impedance spectra is fitted to a model that represents an equivalent circuit, including all the resistances and losses of a real SOFC. The main problem is the identification and set-up of this model. In order to identify an appropriate model the impedance response is analysed by the Distribution function of Relaxation Times (DRTs), where various parameters e.g. temperature, fuel composition, oxygen partial pressure, etc. are varied independently. Their influence on the measured impedance gives information on the contribution of different loss mechanisms, which can be included in the equivalent circuit [57]. It is thus possible to decompose the entire impedance response of the SOFC into the individual contributions e.g. gas diffusion limitations, H_2 electro-oxidation, O^{2-} diffusion, e^- conduction, etc.

Unfortunately, it was not possible to perform this measurement on the metallic supported SOFC, whose microstructure is analysed in this study, due to the limited stability of the SOFC at higher temperatures. These higher temperatures are needed to identify the contribution of the mass-diffusion on the entire measured impedance. Therefore, published data of a similar cell design is used. The metallic support microstructure of the tested cell is slightly different in terms of porosity and pore-size distribution compared to the reconstructed and simulated one. Nevertheless, the two microstructures are still comparable.

The measurement data is presented in [9]. DRT was used to identify the individual loss mechanisms and a process at low frequencies was found to account for the gas diffusion in the metallic support. An appropriate model to relate the impedance resistance $R_{D(\text{anode})}$ to the diffusion is presented in [57]:

$$R_{D(\text{anode})} = \left(\frac{RT}{2F}\right)^2 l_{MS} \frac{1}{D_{H_2,H_2O} f} \left(\frac{1}{p_{H_2(anode)}} + \frac{1}{p_{H_2O(anode)}}\right) \times \left(1.0133 \times 10^5 \frac{\text{Pa}}{\text{atm}}\right)^{-1}, \quad (6.11)$$

where l_{MS} is the length of the metallic support (390 µm), D_{H_2,H_2O} is the binary diffusion coefficient for a mixture of water and hydrogen, f is the scaling factor, defined as $f = \epsilon/\tau^2$, $p_{H_2(anode)}$ and $p_{H_2O(anode)}$ denote the partial pressure of hydrogen and water vapour of the anode gas, respectively. The binary diffusion coefficient was calculated according to the Chapman-Enskog theory for 750 °C and was found to be D_{H_2,H_2O}=6.96 × 10^{-4} $m^2\,s^{-1}$ [74].

The measurement results, together with the fitted function are plotted in Figure 6.15, where the ASR is the area specific resistance, extracted with DRTs from the EIS.

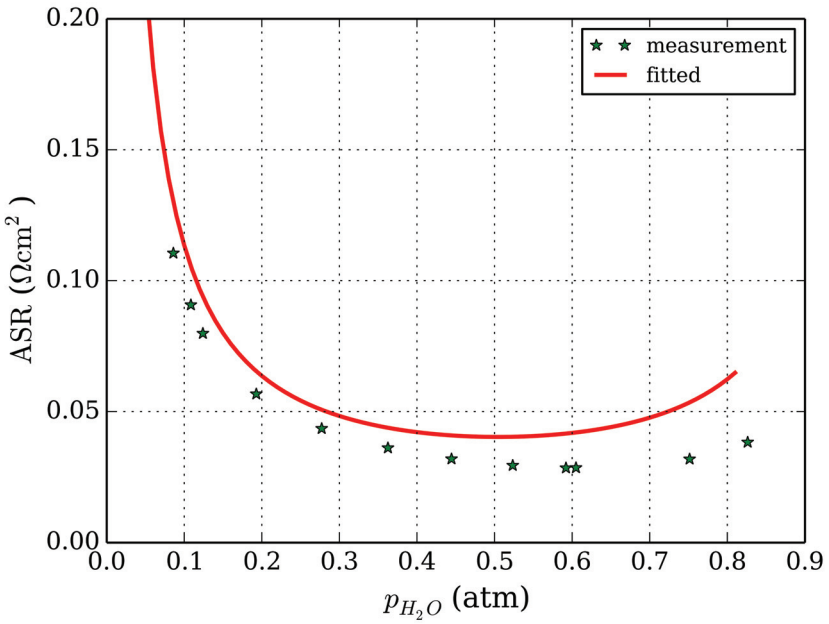

Figure 6.15: p_{H_2O} dependency of the diffusion related processes in the anode (measurement data according to [9]).

The target of the fitting is the evaluation of the scaling factor f in Equation (6.11). The measurement, together with the calculated resistance in Equation (6.11) form an over-determined system of linear equations:

$$\boldsymbol{A}\boldsymbol{x} = \boldsymbol{b}, \tag{6.12}$$

where $\boldsymbol{A}$ is in this case not a matrix, but a vector containing the results of Equation (6.11), $\boldsymbol{x}$ reduces to the scaling factor f and $\boldsymbol{b}$ lists the measurement data. By applying the least-squares method the scaling factor can be evaluated [52]:

$$f = \left(\boldsymbol{A}^T\boldsymbol{A}\right)^{-1}\boldsymbol{A}^T\boldsymbol{b}. \tag{6.13}$$

The measured/fitted scaling factor equals 1.32×10^{-2}. The agreement between the fitted and measured data is satisfying for low p_{H_2O}-values, but gets poorer for higher values. This may be due to the fact that the measurement includes the influences of the metallic support as well as the anode-functional-layer (AFL). In the porous AFL with its smaller pore diameters, Knudsen diffusion is taking place, which is not comprised in the fitting model (see Equation (6.11)). However, the AFL is not considered in this study, why this deviation is not important and the fitted scaling factor can be used for a comparison to the simulated results.

Table 6.2 summarises the validation of the evaluation model with different boundary conditions and surface representations (voxel vs. smooth). The computations on the voxel geometries where carried out on five different geometries with a base area of $200\,\mu m \times 200\,\mu m$ and a thickness of $350\,\mu m$. The approach with fixed values on the gas-channel metallic support interface, as well as the metallic support AFL interface was chosen, although this didn't show the best agreement in the artificial geometry validation case, but it is the most stable set of boundary conditions from a numerical point of view. The positions of the five geometries were chosen in a way that they don't overlap each other and kept some distance to the edges of the sample (see Figure 4.7). This should ensure that influences of the mechanical treatment (cutting) of the cell are not affecting the investigated microstructure. The five geometries are identical for the two sets of computations except for the boundary conditions which are either symmetry or partially periodic (up to 17 %).

Table 6.2: Comparison of the mean values and standard deviations of scaling factors for different boundary conditions calculated on the same five computational voxel geometries to the value obtained from impedance measurements which is 1.32×10^{-2}. The base area is in all cases $200\,\mu m \times 200\,\mu m$ and the height is $350\,\mu m$.

	scaling factor($\times 10^{-2}$)		
boundary condition	mean value	standard deviation	diff (%)
measurement	1.32		
periodic	1.19	0.477	10.9
symmetry	0.81	0.41	63.0

In Table 6.2 the superiority of the proposed application of periodic over zero gradient boundary conditions can be seen. The difference between the measurement and the computation with periodic BCs is roughly 11 %, while the symmetry approach deviates by more than 60 %.

A look at the values of the standard deviations of the scaling factors in Table 6.2 might give an explanation for this huge difference. The rather high standard deviations are an evidence for the very inhomogeneous nature of the metallic support. It was tried to increase the volume of the investigated microstructure stepwise till the scaling factor and the porosity converges and the inhomogeneity does no longer influence the result. One position on the metallic support was chosen and an initial geometry with a base area of 50 µm × 50 µm and a fixed thickness of 350 µm was reconstructed. The porosity and the scaling factor was evaluated. Then the base area of the geometry was increased by 50 µm in each direction, till a maximum base area of 350 µm × 350 µm was reached.

Table 6.3: Porosity values, scaling factor and number of computational cells for a geometry height of 350 µm and increasing base area. The geometry with a base area of 50 µm × 50 µm has not got a continuous pore from the gas-channel to the anode functional layer interface [78].

area (μm^2)	porosity (-)	scaling factor (-) ($x10^{-2}$)	number of computational cells
50 × 50	0.193	–	0.2×10^6
100 × 100	0.196	2.11	0.7×10^6
150 × 150	0.206	1.90	1.6×10^6
200 × 200	0.206	1.99	2.9×10^6
250 × 250	0.192	1.69	4.2×10^6
300 × 300	0.193	1.35	6.1×10^6
350 × 350	0.209	1.73	9.0×10^6

Table 6.3 summarises the results of the windowing analysis of the microstructure. Although the computational limits of the reconstruction algorithm are reached, the obtained porosity values and the scaling factor do not converge. This finding is in accordance to the results found with the *python* program presented in Chapter 4.3, where the porosity values of the metallic support

don't converge till a volume of 500 µm × 500 µm × 350 µm is reached.

Therefore, it is proposed to use several smaller geometries, which require less computational resources, and average the calculated values. This approach has two significant advantages over one larger volume. Firstly, the calculation times of smaller geometries with less computational cells are much shorter, and more important secondly, evaluating the inhomogeneous microstructure of the metallic support at several positions will increase the reliability of the result.

In a further step the influence of the surface representation (voxel vs. smoothed) is assessed. The circumstantial smoothing procedure was carried out on one larger 300 µm × 300 µm × 350 µm geometry. Unfortunately, it was not possible to obtain periodic boundaries in this case with the state-of-the-art procedures offered by *OpenFOAM*. An application will be programmed in the future to determine periodic pores. For the time being, only symmetry boundary conditions can be applied in smoothed geometries. The results are summarised in Table 6.4, where the scaling factor together with the porosity is reported. Again the periodic approach shows a better agreement to the measured scaling factor. And also the results obtained with symmetry boundary conditions on the smoothed surface show a better agreement, although the difference between the smoothed and stair-step approach is roughly 4 %. This means that the solution of the Laplacian equation is not very sensitive on the geometry boundary surface although there is a surface overestimation of ∼37 %. The slightly smaller porosity can be explained by loss of information during the smoothing procedure.

Table 6.4: Comparison of the scaling factor and porosity values of the same geometry in voxel and smoothed surface representation. The volume of the geometry is 300 µm × 300 µm × 350 µm and for the voxel case the influence of the periodic and symmetry boundary condition is analysed.

boundary condition	scaling factor($\times 10^{-2}$)	porosity (-)
periodic (voxel)	1.33	0.1925
symmetry (voxel)	1.17	0.1925
symmetry (smoothed)	1.22	0.1871

Chapter 7

Results

After the validation of the mass-transport (evaluation) and the corrosion model showed their correctness and reliability, this chapter focuses on the applicability and the knowledge gain based on the results of these models. Some of the results in this chapter have already been published, especially the parts concerning geometric evaluation of the microstructure, the determination of the scaling factor [78] and the results of the corrosion model [77].

7.1 Geometric evaluation

The *MATLAB* program presented in Chapter 5.2 is capable of determining the porosity distribution in the microstructure, as well as the average pore diameter, number of pores, etc.

Figure 7.1 shows the porosity distribution of a 350 µm × 350 µm × 350 µm reconstructed geometry. The z-direction corresponds to the diffusion path from the gas-channel to the anode-functional-layer (AFL), while the other two directions are parallel to the gas-channel. In general, the microstructure shows a rather inhomogeneous porosity, varying around 0.20, but especially in the first 100 µm of the diffusion path a much denser microstructure is prevailing, compared to the rest of the metallic support.

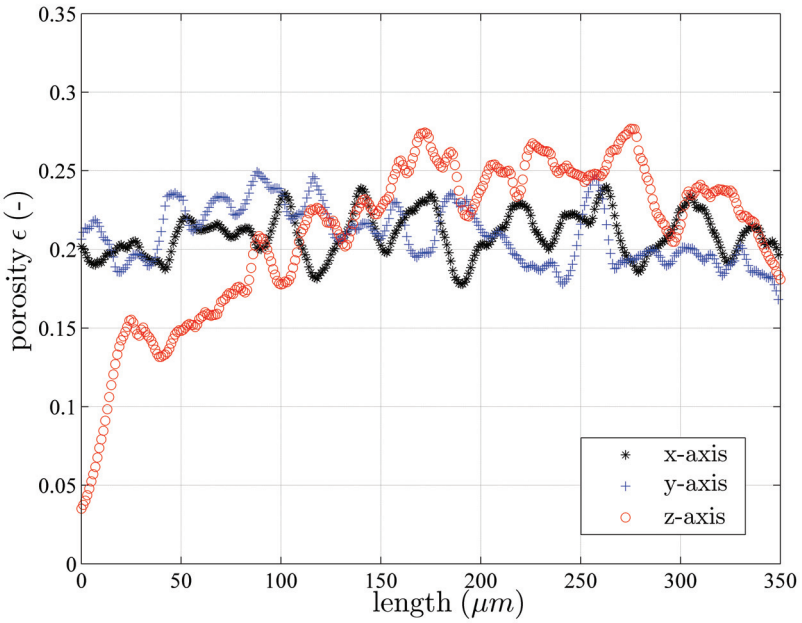

Figure 7.1: Porosity distribution along the three coordinate axes for the windowing geometry with a base area of 350 µm × 350 µm. The z-direction is the diffusion path from the gas-channel to the anode functional layer. While the directions parallel to the gas-channel show an homogeneous porosity distribution, the diffusion path orthogonal to the gas channel has a much lower porosity in the first 100 µm compared to the rest of the electrode. The gas-channel interface is located at 0 µm and the interface to the anode functional layer at 350 µm [78].

The denser region might be caused by the sintering process, where a longer exposure time in a hotter environment may lead to a higher densification. This is an important feedback for the cell production process, where actions can be taken to minimise these effects.

Another interesting property of the microstructure is the average pore diameter because it indicates if the flow can still be considered as a continuum or if other modelling approaches have to be undertaken. In Chapter 3.2.2.3 the *Knudsen* number was presented which is the ratio between the free path of the molecules and a characteristic length (e.g. pore diameter). If the *Knudsen* number is below 0.01 the continuum approach with the application of partial differential equations is valid. *Knudsen* numbers in the range or larger than 1 indicate that the interaction between the gas molecules and the walls are more dominant than the interaction amongst the molecules. In this case the continuum models fail and a statistical modelling approach has to be applied.

In order to determine the *Knudsen* number the algorithm is capable of discerning individual pores along the diffusion path and calculates their equivalent diameter, that corresponds to the

diameter of a circle with the same cross-sectional area as the pore.

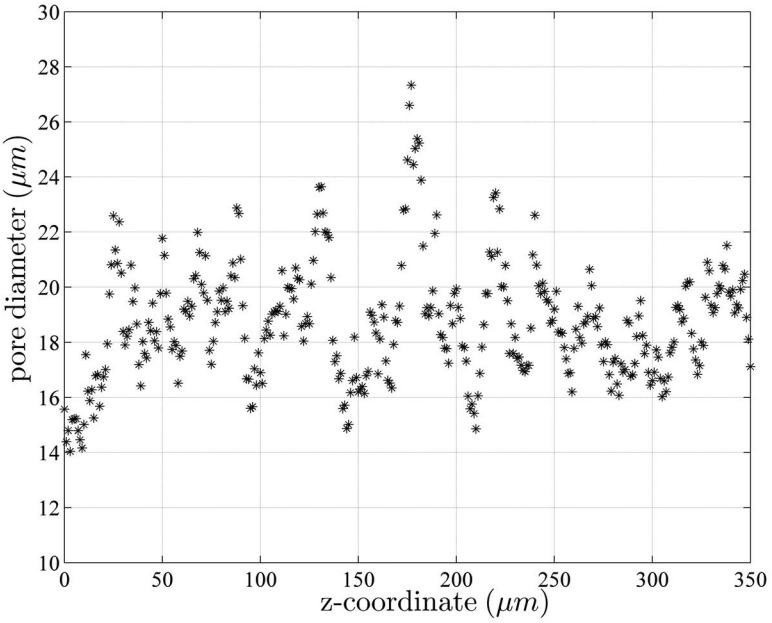

Figure 7.2: Mean pore diameter distribution along the diffusion path. The gas-channel interface is at 0 µm and the interface to the anode functional layer at 350 µm [78].

Figure 7.2 shows the equivalent pore diameter distribution along the diffusion path. Each point in the graph is the average equivalent pore diameter at this height level. The gas-channel metallic support interface is located at 0 µm and the interface between the metallic support and the anode-functional-layer lies at 350 µm. The average pore diameter of the five sample positions is 18.1 µm. The mean free path length of hydrogen λ_{H_2} according to Equation (3.54) is ∼700 nm and thus the calculation of the *Knudsen* number yields:

$$K_n = \frac{\lambda_{H_2}}{d_p} = \frac{0.7}{18.1} = 0.039, \tag{7.1}$$

which is slightly higher than 0.01, but sufficiently below 1 so that the continuum approach is still applicable.

Another result of the geometric evaluation algorithm is the determination of the number of individual pores along the diffusion path shown in Figure 7.3. Here again a similar finding can be seen as the porosity distribution in Figure 7.1. In the first 50 µm at the gas-channel metallic support interface only half as much pores can be identified compared to the rest of

the metallic support. This also points to a too high densification of the material due to the sintering process.

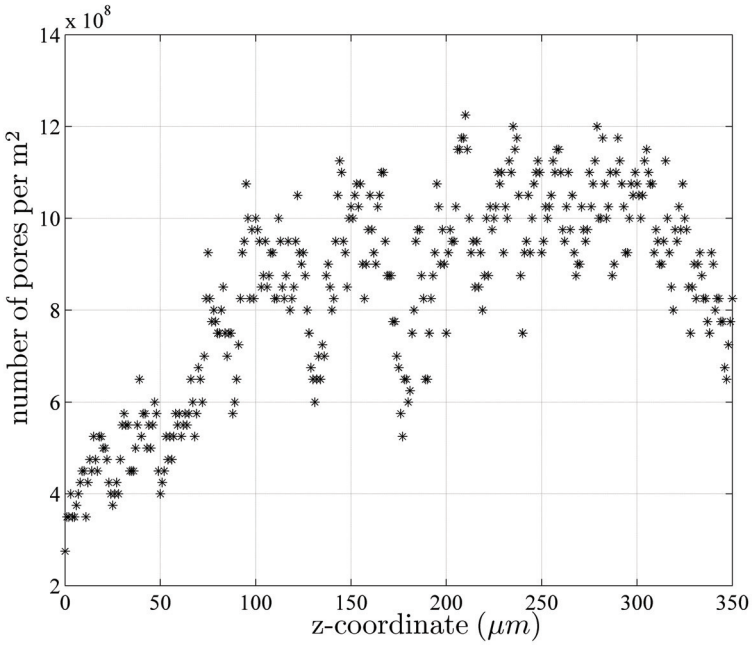

Figure 7.3: Number of pores per m^2 along the diffusion path. In the first 100 µm there are less pores compared to the rest of the metallic support. The gas-channel interface will be at 0 µm and the interface to the anode functional layer at 350 µm. The base area is 200 µm × 200 µm [78].

7.2 Mass-transport model

7.2.1 Permeability

It was shown in Chapter 6.2.1 that the determination of a symmetric permeability tensor in the real microstructure is not possible, with the state-of-the-art boundary conditions. This is due to the fact that the boundary areas are not 100 % periodic and the available boundary area for the flow differs along the three coordinate axes. Nevertheless, it is at least possible to retrieve the permeabilities in the main directions. To do so the pressure drop for different superficial velocities is computed in the three coordinate directions (three individual calculations for each superficial velocity). The results are fitted with the Forchheimer equation using a non-linear

least-square fit. The Forchheimer equation is repeated here for the readers convenience:

$$\Delta p = a_1 U_x + a_2 U_x^2. \tag{7.2}$$

It relates the pressure drop Δp to the superficial velocity U_x. The coefficient in the linear term $a_1 = \frac{\mu \Delta l}{k_{ii}}$ represents the Darcy effects, while the squared term $a_2 = \frac{\rho \Delta l}{s_{ii}}$ accounts for the non-linear effects caused by inertial forces. The pressure drop in the microstructure for different velocities in x-direction (parallel to the gas-channel) and the fitted function is plotted in Figure 7.4.

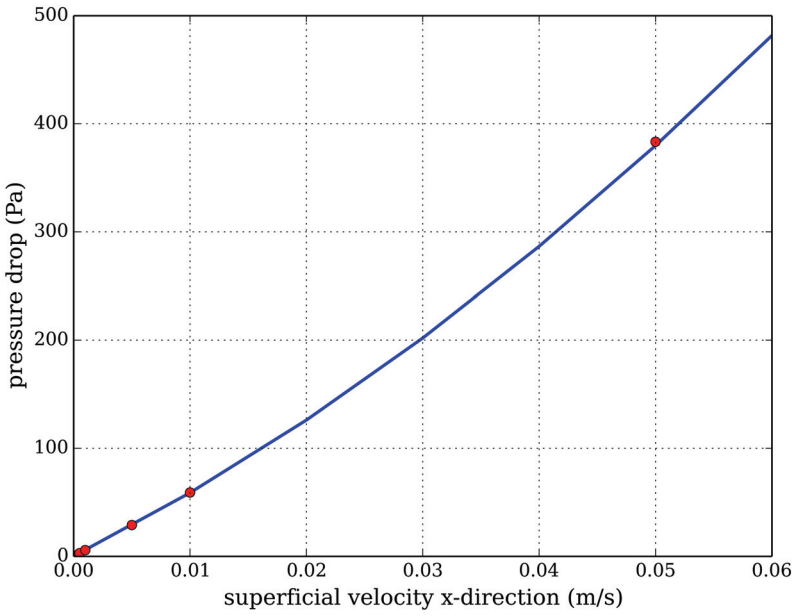

Figure 7.4: Calculated pressure drop in the microstructure for different superficial velocities (red dots) and fitted function.

The calculated Darcy permeabilities are:

$$k_{xx} = 5.52 \times 10^{-14}\,\mathrm{m}^2 \quad k_{yy} = 4.56 \times 10^{-14}\,\mathrm{m}^2 \quad k_{zz} = 3.18 \times 10^{-14}\,\mathrm{m}^2, \tag{7.3}$$

and the corresponding Forchheimer terms are:

$$s_{xx} = 6.94 \times 10^{-9}\,\mathrm{m} \quad s_{yy} = 4.83 \times 10^{-9}\,\mathrm{m} \quad s_{zz} = 2.19 \times 10^{-9}\,\mathrm{m}. \tag{7.4}$$

The z-direction corresponds to the main diffusion path through the metallic support from the gas-channel to the anode-functional-layer. The Darcy permeability in this direction is the smallest $k_{zz} = 3.18 \times 10^{-14}\,\mathrm{m}^2$ and a low permeability means less mass flow at a given pressure gradient.

A plot showing the pressure distribution within the microstructure together with the streamlines is presented in Figure 7.5. Here the flow direction is from left to right along the main diffusion path. Only few continuous pores are present in this geometry, indicated by the streamlines which go through the entire geometry. This may be caused by the dense interface between the gas-channel and the metallic support identified with the geometric evaluation algorithm.

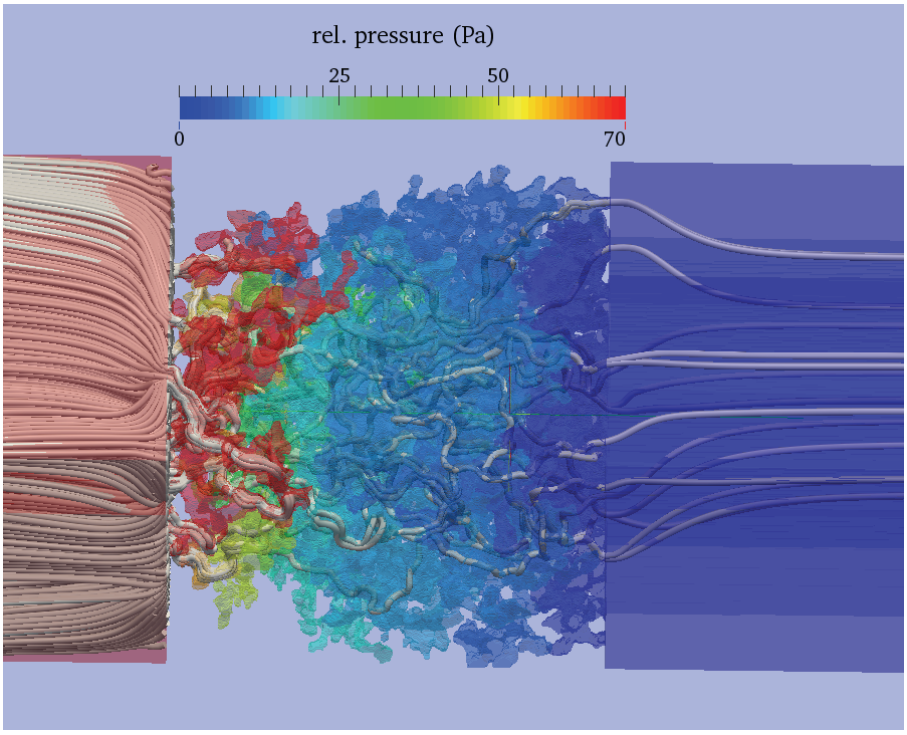

Figure 7.5: Calculated relative pressure drop in the reconstructed metallic support. Flow direction is from left (gas-channel interface) to right (anode-functional-layer interface). The superficial velocity is $5 \times 10^{-3}\,\mathrm{m\,s^{-1}}$. The streamlines (depicted as tubes) indicate that only some continuous pores are present, due to dense interface between the gas-channel and the metallic support.

The influence of the applied lateral boundary conditions, as well as the surface representation (voxel vs. smooth) is assessed by comparing the computed pressure drop of the same geometry with different settings. The results for a superficial velocity of $0.05\,\mathrm{m\,s^{-1}}$ are summarised in Table 7.1.

Table 7.1: Comparison of the influence of the surface representation and the boundary conditions on the pressure drop for a superficial velocity of $0.05\,\mathrm{m\,s^{-1}}$.

	periodic	symmetry
voxel	372.2 Pa	1287.6 Pa
smoothed	-	1185.2 Pa

From this finding it can be concluded that the application of symmetry boundary conditions yields a much higher ($\sim$ factor 3.5) pressure drop because dead-end pores are created by this boundary condition. The geometry with the smoothed surface has a $\sim$8 % lower pressure drop compared to the voxel surface. Actually, it was anticipated that this difference would be much higher because the surface area has a huge influence on the flow resistance. But due to the low velocity, the flow creeps and the effect of the surface area diminishes. It is expected that the lowest pressure drop will be calculated with periodic boundary conditions on a smoothed surface. Unfortunately, the state-of-the-art procedures in *OpenFOAM* don't support this approach.

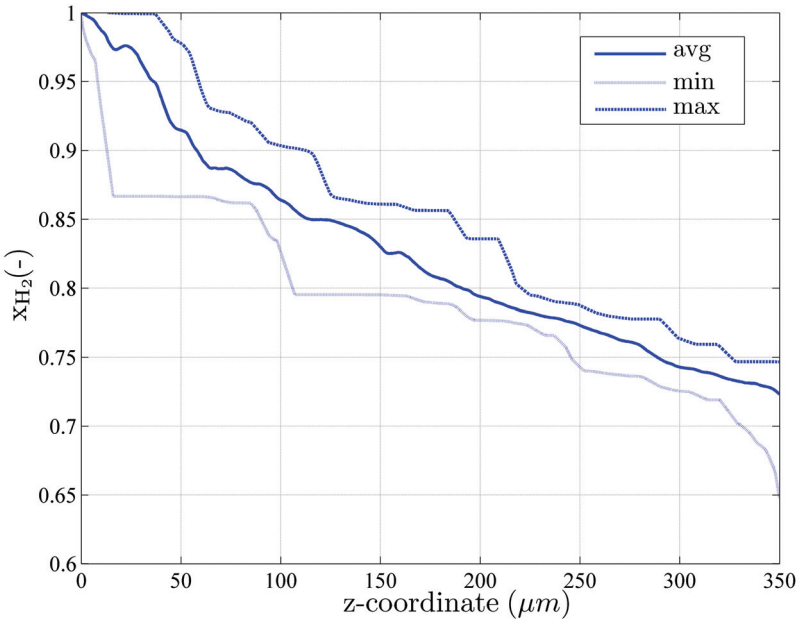

Figure 7.6: Computed concentration gradient of hydrogen in one reconstructed microstructure. The interface between the gas-channel and the metallic support is at 0 µm and the interface between the metallic support and the anode-functional-layer lies at 350 µm.

7.2.2 Effective diffusion coefficient

The determination of the effective diffusion coefficient was carried out on five independent reconstructed geometries with a volume of 200 µm × 200 µm × 350 µm per geometry. The boundary conditions perpendicular to the main diffusion path (e.g. gas-channel; anode-functional-layer) were set to fixed value, while the lateral walls (parallel to the diffusion path) were set to periodic, wherever possible (∼17 % periodic; rest symmetry). The geometric evaluation algorithm identified two different dense regions in the microstructure.

A closer look at the concentration gradient within the microstructure illustrates this finding. The concentration gradient plotted in Figure 7.6 is much steeper in the first 100 µm compared to the rest of the microstructure.

This behaviour cannot be reproduced in cell-simulations with only one effective diffusion coefficient. Therefore, the microstructure is subdivided into two parts: One describing the denser first 100 µm of the metallic support, and the other the more porous rest of the support. A principal sketch can be seen in Figure 7.7.

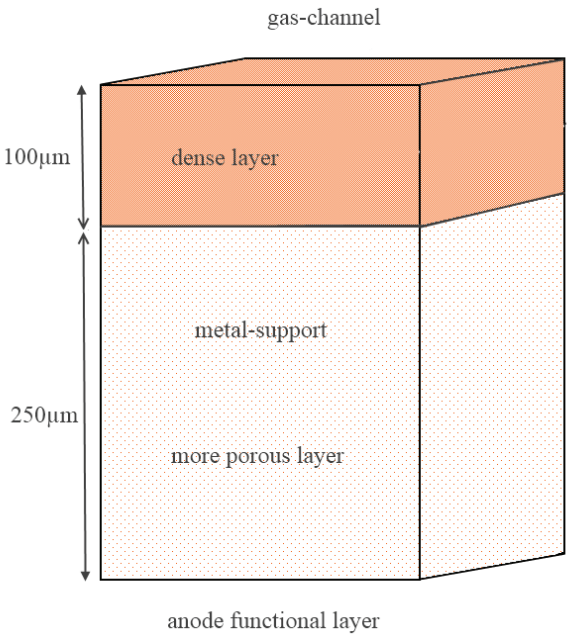

Figure 7.7: Principal depiction of the metallic support with the 100 µm thick dense upper layer (referred to as *dense*) and the more porous 250 µm of the remaining metallic support (referred to as *porous*). Homogenised parameters (referred to as *hom*) are calculated for the entire height of 350 µm [78].

The porosity, tortuosity and scaling factor were evaluated for each section and the results are summarised together with the homogenised value for the entire metallic support in Table 7.2. The tortuosities were calculated with the correct formulation derived in Equation (5.24) which is $\tau = \sqrt{\epsilon/f}$. It was discussed in Chapter 5.3.2 and it is stressed again here, that the calculated tortuosities do not reflect the geometric interpretation of the microstructure, but they also include effects like orifices, stagnant pockets and dead-end pores.

Table 7.2: Comparison of microstructural parameters, obtained from 3-D reconstruction/modelling, averaged from five different computational geometries, with a base area size of 200 µm × 200 µm. The subscript *hom* refers to the overall homogenised parameter calculated with a height of 350 µm. The *dense*-parameters are evaluated only in the first 100 µm, where a significant lower porosity was found (see Figure 7.1). Parameters with the subscript *porous* are computed in the remaining region (from 100 to 350 µm). The principal positions of the geometries are shown in Figure 4.7, and Figure 7.7 depicts the positions of the different layers [78].

	mean value	standard deviation
ϵ_{hom}	0.200	0.009
scaling factor f_{hom}	1.19×10^{-2}	4.8×10^{-3}
τ_{hom}	4.3	0.81
ϵ_{dense}	0.147	0.006
scaling factor f_{dense}	0.84×10^{-2}	4.03×10^{-3}
τ_{hom}	4.1	0.59
ϵ_{porous}	0.219	0.013
scaling factor f_{porous}	1.94×10^{-2}	5.7×10^{-3}
τ_{hom}	3.9	0.86

As expected the porosity and also the scaling factor is much lower for the denser region compared to the more porous region. However, the obtained values for the scaling factor are by a factor of 20 smaller than those usually obtained by fitting of the material parameters to experiments [5, 18, 38, 84, 88, 98]. Admittedly, those experiments where either carried out on anodes or cathodes with considerably different microstructures, so a direct comparison may be misleading. However, it seems that the metallic support with its large pore diameter has a considerable amount of dead-end pores which account for these low scaling factors.

7.3 Corrosion

The presented corrosion model is able to determine the porosity and the scaling factor as a function of time, depending on the oxide growth in the microstructure. The required input parameters for the corrosion model are the linear k_l and parabolic rate constants k_p.

Table 7.3: Linear and parabolic rate constants for the corrosion simulations at different temperatures. The values of k_l and k_p are obtained by splitting the measured weight gain into an initial, faster regime and a slower regime, and fitting the data to the corresponding linear or parabolic growth law. The rate constant $k_{p,e}$ was determined by fitting the entire measurement data to the parabolic growth law [77].

temperature (°C)	k_l ($\mathrm{m\,s^{-1}}$)	k_p ($\mathrm{m^2\,s^{-1}}$)	$k_{p,e}$ ($\mathrm{m^2\,s^{-1}}$)
650	8.83×10^{-14}	1.30×10^{-21}	1.61×10^{-21}
750	2.98×10^{-13}	2.40×10^{-20}	3.28×10^{-20}
850	5.30×10^{-13}	7.07×10^{-20}	1.15×10^{-19}

These values can be either obtained from literature or more preferably from measurements. The values for the rate constants presented in Table 7.3 were extracted from corrosion experiments carried out by Åsa Persson from DTU at 650 °C, 750 °C and 850 °C in simulated anode outlet gas ($Ar/H_2/H_2O$-atmosphere with $p_{H_2O}/p_{H_2} = 9$). The measurement data was fitted to either a linear or parabolic function to obtain the corrosion rate constants for the simulation. $k_{p,e}$ is the parabolic rate constant if the entire corrosion is considered to obey parabolic kinetics.

The change of the average porosity due to corrosion for different temperatures is depicted in Figure 7.8. In the corrosion computations both the linear and the parabolic kinetics were considered. A higher porosity decrease can be seen in the first few hours, during the faster linear growth. After this the growth of the oxide layer slows down and the porosity decreases more slowly. While the porosity change for 750 °C and 850 °C is certainly too high, it is ∼10 % after 40 000 h at 650 °C. If this value is still tolerable cannot be assessed by an average porosity value alone, having in mind the inhomogeneous porosity distribution in the metallic support.

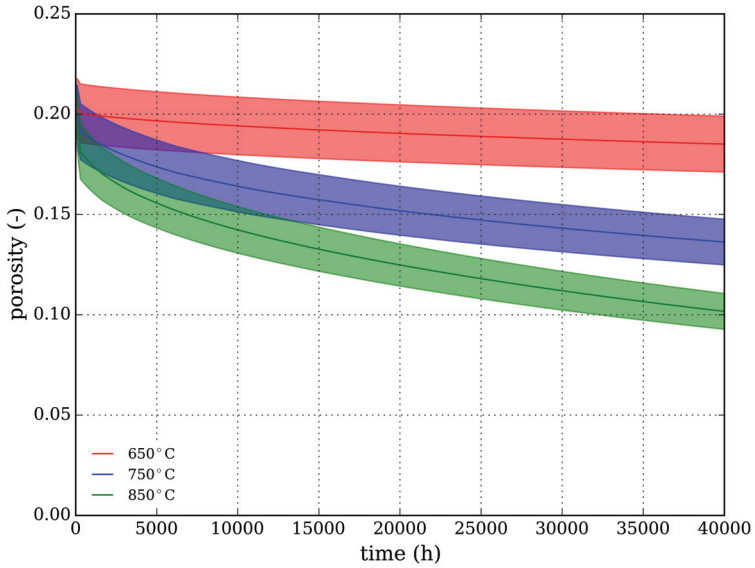

Figure 7.8: Computed averaged porosity of five different sample geometries. The volume of each reconstructed geometry is 200 µm × 200 µm × 350 µm. With ongoing corrosion the porosity is decreasing [77].

A closer look at the change of the porosity distribution due to the corrosion at different temperatures is given in Figure 7.9. The porosity distribution after 40 000 h is calculated on a representative 200 µm × 200 µm × 350 µm geometry and compared to the initial distribution. The microstructure becomes denser at higher temperatures, due to increased corrosion rates, and the porosity distribution gets smoothed, with a reduced standard deviation.

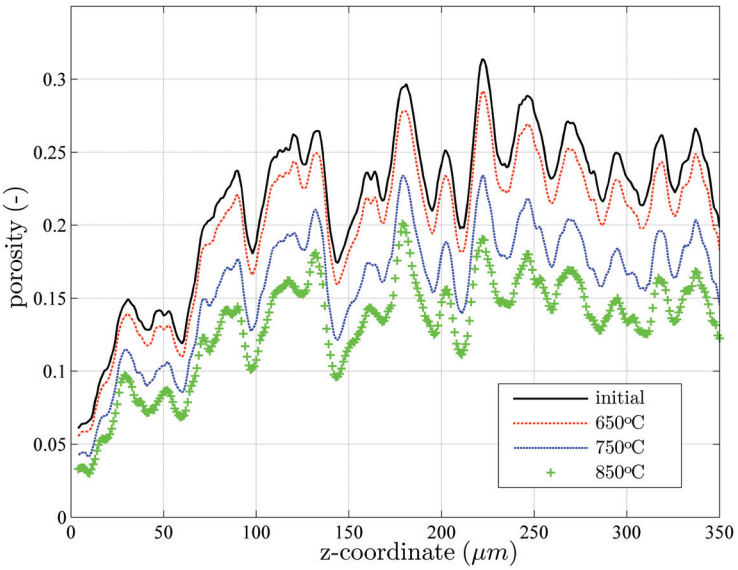

Figure 7.9: Initial porosity distribution along the diffusion path of one representative geometry (200 µm × 200 µm × 350 µm) compared to the porosity after 40 000 h corrosion at different temperatures. The interface to the gas-channel is at 0 µm and the interface to the anode functional layer at 350 µm [77].

However, the applicability of the metallic support in SOFCs does not so much depend on the porosity, but more on its ability to ensure a sufficient supply of fuel gas to the anode functional layer. Therefore, also the homogenised scaling factor f is evaluated at different times for the three temperatures (650 °C, 750 °C and 850 °C). Note: The effective diffusion coefficient is defined as $\mathscr{D}_{ij}^{e} = f\mathscr{D}_{ij}$. The percentage difference to the evaluated scaling factor $f = 1.19 \times 10^{-2}$ without corrosion is plotted in Figure 7.10. A tremendous decrease of the scaling factor can be observed at 750 °C and 850 °C after 40 000 h. The difference is −65.9 % and −88.0 % respectively, which means that the mass diffusion at 850 °C is by a factor of ∼8 smaller than the initial mass diffusion. At 650 °C the decrease of the scaling factor is 15.3 %.

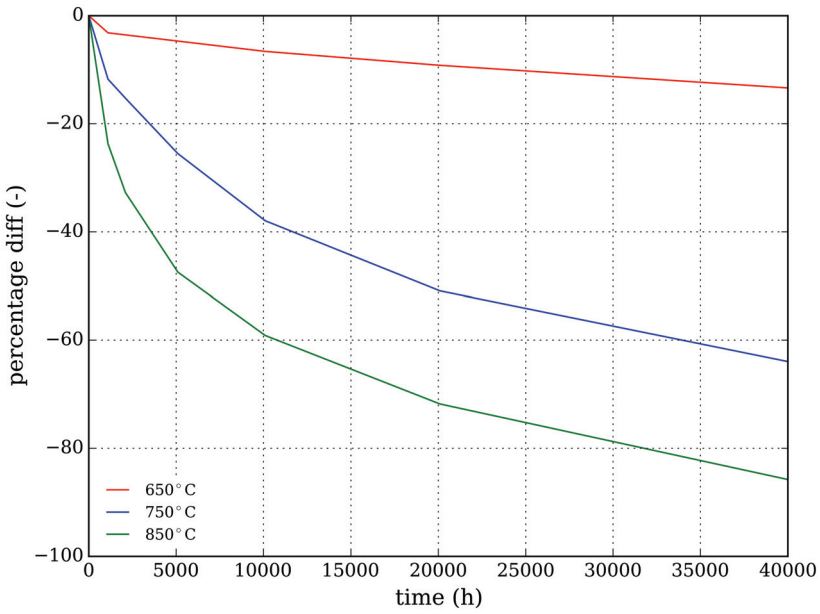

Figure 7.10: Calculated averaged scaling factor difference for five independent reconstructed geometries. The geometry size is 200 µm × 200 µm × 350 µm and the change of the microstructure due to corrosion was computed at 650 °C, 750 °C and 850 °C. The averaged scaling factor f for a non-corroded sample is 1.19×10^{-2}. Note: The scaling factor is the ratio between the binary and the effective diffusion coefficient [77].

In order to assess the influence of the decreased scaling factor on the concentration over-potential the Nernst Equation (2.6) is used. It relates the difference of the partial pressures in the gas-channel to the partial pressures in the anode-functional layer. The hydrogen partial pressure in the metal-support can be computed with the models presented in Chapter 3.2.2. The required binary diffusion coefficients for the temperatures 650 °C, 750 °C and 850 °C are calculated with the Chapman-Enskog model (see Chapter 3.2.3). The molar fraction of hydrogen in the gas-

channel interface is fixed to 0.9, while the hydrogen flux ϕ_{H_2} at the anode-functional-layer interface is defined by Faraday's law:

$$\phi_{H_2} = \frac{j}{2F}, \tag{7.5}$$

where j is the current density and F Faraday's constant. A current density of $1\,\mathrm{A\,cm^{-2}}$ is assumed for the simulations.

The computed averaged concentration over-potential for five independent reconstructed geometries is summarised in Table 7.4. The change of the concentration over-potential over time at 650 °C is not dramatic and may be tolerable. However, the oxide growth after 40 000 h at 850 °C proceeded so fast that the mass-transport of hydrogen is limited to an extend that not enough fuel can be supplied to the anode-functional-layer at this current density.

Table 7.4: The computed averaged concentration over-potential for five independent reconstructed geometries. The presumed current density was $1\,\mathrm{A\,cm^{-2}}$ and the molar fraction of hydrogen in the gas-channel was 0.9. The change of the pore volume after 40 000 h at 850 °C was so high that the supply of the anode with hydrogen was not sufficient, which indicates the blocking of some pores (according to [77]).

temperature	concentration over-potential η_{conc} (V)					
°C	1000 h	2000 h	5000 h	10 000 h	20 000 h	40 000 h
650	0.056	0.056	0.056	0.057	0.058	0.060
750	0.062	0.064	0.070	0.080	0.094	0.119
850	0.072	0.079	0.094	0.113	0.154	-

In Figure 7.11 the concentration distributions along the main diffusion path of one geometry for different temperatures after 20 000 h are plotted. The molar fraction of hydrogen is fixed to 0.9 mol at the gas-channel metallic support interface, while a fixed gradient boundary condition is applied at the metallic support anode-functional-layer interface. The huge differences in the molar fraction of hydrogen at the AFL interface are an evidence for the blocking of some pores, a decreased mass-diffusion and a required higher gradient to supply enough hydrogen.

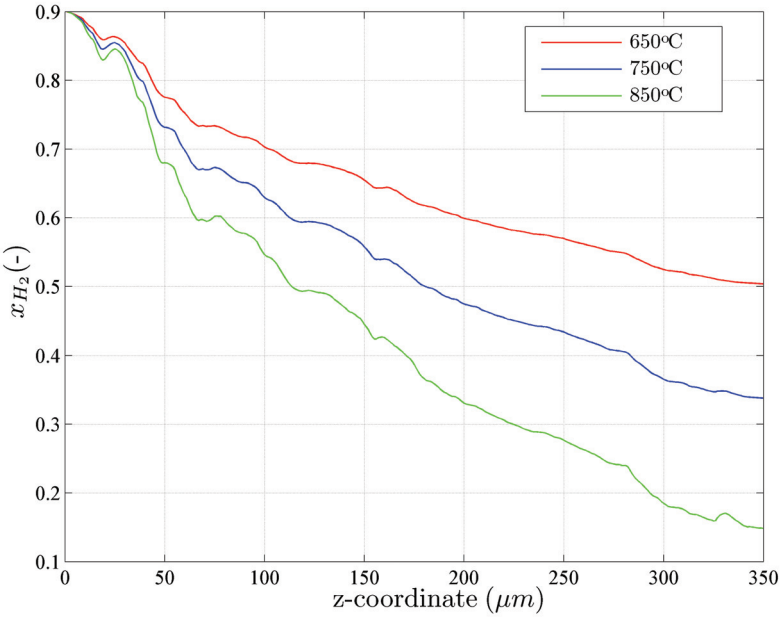

Figure 7.11: Averaged mass fraction distribution along the diffusion path after 20 000 h for different temperatures in a volume of 200 µm × 200 µm × 350 µm. The molar fraction of hydrogen is fixed to 0.9 at the interface between the gas-channel and the metallic support, while a fixed gradient (a fixed flux of hydrogen) is applied on the metallic support anode-functional-layer interface. The lateral boundaries are partly periodic and symmetry [77].

The computed oxide growth and its influence on the mass-diffusion through the metallic support, with the measured corrosion rate constants, is sufficiently low for 650 °C, so that a satisfactory amount of hydrogen can be supplied to the anode-functional-layer throughout the lifetime of the SOFC. On the other hand, the application of this type of metallic support at higher temperatures is not feasible because of the high decrease of the effective diffusion coefficient and the increase of the concentration over-potential.

The huge advantage of the proposed corrosion model is its dependency on parameters which can be retrieved rather easily by measurements. Nevertheless, the obtained results have to be interpreted with care because the assumption that no spallation occurs may not hold true, especially during thermal cycles, which would increase the corrosion rate.

Chapter 8

Conclusions

A thorough modelling study of the mass-transport in the porous metallic support microstructure has been presented in this thesis, in order to obtain a deeper knowledge and understand the implications of mass-diffusion on the overall cell performance. The proposed approach made steps beyond the state-of-the-art by firstly improving the results by applying periodic boundary conditions and secondly by developing a corrosion model, that is capable of determining the change of the porous structure due to oxide growth and hence its impact on the mass transport.

8.1 Mass-transport modelling

The determination of homogenised microstructural parameters of SOFC anodes and cathodes is state-of-the-art. The proposed approach was pursued in this study and applied on the metallic support. However, the usage of symmetry boundary conditions for the lateral walls seemed to introduce a lot of additional dead-end pores in the microstructure. Therefore, the state-of-the-art approach was improved by applying periodic boundary conditions at the lateral walls, wherever possible. In the case of the investigated metallic support $\sim$17 % of the lateral walls are periodic, while the rest is still symmetry. By this new treatment of the boundaries it was possible to obtain a computed scaling factor that is only 11 % smaller than the measurement value, compared to a 60 % deviation in case of the state-of-the-art approach.

Furthermore, it could be shown that the implementation of the Maxwell-Stefan diffusion model needs special attention. Its incorporation into the species conservation equation requires the addition of a pressure term in order to ensure consistency in the chosen reference frames. Disregarding this effect leads to an underestimation of the concentration over-potential which becomes significant even at low current densities.

A detailed investigation of the porosity distribution within the microstructure revealed the inhomogeneous nature of the metallic support. Especially the first 100 µm along the diffusion path are much denser compared to the rest of the microstructure. This dense layer might be caused during the sintering and is an important feedback for cell production. Even apart from this denser layer the porosity of the entire microstructure is rather inhomogeneous which is caused by the larger particle size of the sinter material, resulting in average pore diameters of ∼18 µm. These diameters are much larger compared to the state-of-the-art anodes and cathodes. However, the scaling factor is smaller, which indicates that several dead-end pores are prevailing in the microstructure. This could be visualised by plotting streamlines of the velocity field, where only few pores are continuous from the gas-channel to the anode-functional-layer.

8.2 Corrosion modelling

One significant step beyond the state-of-the-art in determining homogenised material parameters was taken, and a corrosion model was developed that is capable of describing the change of the microstructure caused by oxide volume expansion. So far it was only possible to compute the scaling factor, or the effective diffusion coefficient of the measured microstructure. This microstructure will be prone to changes during the process and the informative value of the obtained scaling factor decreases over time because it describes a completely different microstructure. With the developed and validated corrosion model the growth of the oxide and the corresponding change of the microstructure can be predicted. This offers the opportunity to compute the scaling factor as a function of time and an estimation of the degradation due to

corrosion is possible. One great advantage is that the model requires only parameters which are accessible by measurements, which makes it an applicable and reliable tool.

8.3 Applications

With state-of-the-art measurement technologies like FIB-SEM or X-ray CT the microstructure of SOFCs can be scanned and the obtained results are converted into computational geometries. The developed models offer a deep insight into the physical phenomena taking place inside the metallic support and deliver important information on them. Firstly, the determination of the porosity distribution is an significant feedback for the cell fabrication process and the sintering parameters. Secondly, the evaluated scaling factor is a fundamental parameter in cell- and stack-modelling which would otherwise be solely a fitting parameter without a physical meaning. It is thus possible to improve the models further and make the results more reliable. Thirdly, the corrosion model can substitute costly, long term corrosion measurements, and will help to assess the applicability of different metal materials for metallic-supported SOFCs.

8.4 Future Work

Improvements to existing approaches and new models have been developed, and as it always is the case:

> Nothing is as simple as it seems at first,
> or as hopeless as it seems in the middle,
> or as finished as it seems in the end.

quoted from an *unknown* source, there is still room for further improvement. Two main aspects are the improvement of the lateral boundary conditions and the enhancement of the corrosion solver.

The application of partially periodic boundaries (∼17 %) shows a significant improvement of the obtained results. Nevertheless, the deviation to the measurements is 10 % and a full periodic approach will probably yield even more accurate results. To this end, all computational faces belonging to individual pores should be identified. Then the entire mass flux of each face should be mapped to the other side, allowing a flow through the entire pore area and not only through the periodic faces. This approach should also solve the problem with the asymmetric permeability tensor.

For the time being the corrosion solver is capable of computing the change of the porous microstructure due to corrosion, but relies completely on the corrosion rate constants. A further improvement would be the implementation of a more sophisticated corrosion model which describes the growth of the oxide and takes the ion diffusion in the oxide layer into consideration.

List of Tables

3.1 Diffusion fluxes and constraints [86] 30

4.1 Comparison of reconstructed microstructures with different voxel-sizes. 50

4.2 Geometric features of voxel and smoothed microstructure. 55

6.1 Comparison between the computed and analytical results of the artificial geometry with different boundary conditions. A sketch explaining the application of the boundary conditions at the different patches is provided in Figure 6.14. The calculated porosity value is 0.261. 90

6.2 Comparison of the mean values and standard deviations of scaling factors for different boundary conditions calculated on the same five computational voxel geometries to the value obtained from impedance measurements which is 1.32×10^{-2}. The base area is in all cases $200\,\mu m \times 200\,\mu m$ and the height is $350\,\mu m$. 94

6.3 Porosity values, scaling factor and number of computational cells for a geometry height of $350\,\mu m$ and increasing base area. The geometry with a base area of $50\,\mu m \times 50\,\mu m$ has not got a continuous pore from the gas-channel to the anode functional layer interface [78]. 95

6.4 Comparison of the scaling factor and porosity values of the same geometry in voxel and smoothed surface representation. The volume of the geometry is 300 µm × 300 µm × 350 µm and for the voxel case the influence of the periodic and symmetry boundary condition is analysed. 96

7.1 Comparison of the influence of the surface representation and the boundary conditions on the pressure drop for a superficial velocity of $0.05\,\mathrm{m\,s^{-1}}$. 103

7.2 Comparison of microstructural parameters, obtained from 3-D reconstruction/-modelling, averaged from five different computational geometries, with a base area size of 200 µm × 200 µm. The subscript *hom* refers to the overall homogenised parameter calculated with a height of 350 µm. The *dense*-parameters are evaluated only in the first 100 µm, where a significant lower porosity was found (see Figure 7.1). Parameters with the subscript *porous* are computed in the remaining region (from 100 to 350 µm). The principal positions of the geometries are shown in Figure 4.7, and Figure 7.7 depicts the positions of the different layers [78]. 105

7.3 Linear and parabolic rate constants for the corrosion simulations at different temperatures. The values of k_l and k_p are obtained by splitting the measured weight gain into an initial, faster regime and a slower regime, and fitting the data to the corresponding linear or parabolic growth law. The rate constant $k_{p,e}$ was determined by fitting the entire measurement data to the parabolic growth law [77]. 106

7.4 The computed averaged concentration over-potential for five independent reconstructed geometries. The presumed current density was $1\,\mathrm{A\,cm^{-2}}$ and the molar fraction of hydrogen in the gas-channel was 0.9. The change of the pore volume after 40 000 h at 850 °C was so high that the supply of the anode with hydrogen was not sufficient, which indicates the blocking of some pores (according to [77]). 109

List of Figures

2.1 Principal sketch of the individual components of a single SOFC, including their functions (according to [58]). 10

2.2 Ideal and actual fuel cell voltage-current characteristics according to [48]. 12

2.3 Cross-section of a sintered planar metallic supported half cell, without infiltration and screen-printed cathode. The dense electrolyte is shown to the left, followed by the cermet layer (anode) and the metallic support [9]. 13

3.1 Richardson Ellingham diagram of free energy versus temperature for oxidation of metals [44] 15

3.2 Formation of an oxide film during high-temperature metal oxidation [44]. 16

3.3 Processes occurring in three types of oxide surface scale during high-temperature oxidation [44]. 18

3.4 Growth rate of an oxide film as a function of its thickness, calculated with the theory of Cabrera and Mott when thin ($x_{corr} < X_1$) and of Wagner when thick ($x_{corr} > L_D$). The parameters used are appropriate to a film of NiO growing by lattice diffusion at 500 °C according to [3]. 19

3.5 Schematic classification of flow through porous media according to [4] 24

3.6 Schematic representation of experimental relationship between the superficial velocity and the pressure gradient according to [4]. 25

3.7 Shortest and tortuous path between two points. 38

3.8 Dead-end pores, stagnant pockets and bottlenecks will effect the diffusion in the microstructure according to [4]. 40

4.1 Schematic assembly of a FIB-SEM [102]. 42

4.2 Schematic assembly of an X-ray nano CT system: X-ray optics are utilised to focus the incident and transmitted beam, enabling high-resolution 3D X-ray CT imaging [81]. 43

4.3 Left-hand side shows a single 2-D image representing a slice through the obtained 3-D microstructure with X-ray CT-scans. The digitalised binary image is shown on the right-hand side (white → material, black → pores) [78]. 44

4.4 Reconstruction of a computational geometry out of an image-stack data-set obtained with X-ray CT [78]. 45

4.5 Computational geometry with lateral boundaries shown in dark blue → symmetry and red → periodic boundary. The diffusion path is from top to bottom. Approximately 17 % of the lateral boundary area can be defined to be periodic boundaries. The size of the geometry is 300 µm × 300 µm × 350 µm [78]. 46

4.6 Algorithm to determine a representative volume of the metallic support. The porosity is evaluated for increasingly larger volumes till a constant porosity is reached. The minimum representative volume lies in the range of 0.1 mm^3 which corresponds a cube with approx. 500 µm × 500 µm × 350 µm. 47

4.7 Top view of the metallic support with positions of the arbitrarily chosen samples. It is ensured that the sample positions don't overlap and a certain distance is kept to the edges [78]. One continuous square represents an area of 100 µm × 100 µm. 48

4.8 Reconstruction of the same geometry with varying voxel volumes from left to right 1 µm^3, 8 µm^3 and 27 µm^3. The circles indicate regions where the pores are not resolved properly and information is lost, compared to the 1 µm^3 case. . . . 49

4.9 Comparison between the original rough voxel-surface (left-hand-side) and the smoothed surface (with *Meshlab*) (right-hand-side). 52

4.10 Comparison of the final smoothed volume meshes generated by the snapping of the original stair-step surface (left-hand-side) and the pre-smoothed surface (right-hand-side). While the stair-step nature can still be seen on the left-hand-side, the pre-smoothed surface can be converted in a smoothed volume mesh. . . 53

4.11 Comparison between the stair-step surface mesh and the final volume meshes for different parameter settings in *snappyHexMesh* for an arbitrarily chosen slice position of the geometry. The black lines represent the original stair-step surface, which is smoothed and then snapped. The red areas show the volume mesh with a lower refinement, while the green areas are obtained with a higher refinement. The higher the refinement the better the reconstruction of the initial geometry gets. 54

4.12 Description of skewness. The centre point of the shared face **f** deviates from the point $\mathbf{f_i}$ obtained by the intersection between this shared face and a straight line between the two centre points **P** and **N** of the cell [41]. 55

4.13 Simple artificial microstructure consisting of small tubes with a diameter of 10 µm and a normal distance of 20 µm. The overall size of the geometry is 222 µm × 286 µm × 213 µm. All faces on opposite walls are periodic. Note: The pores on the left-hand side look slightly distorted due to the perspective. 56

4.14 One generated slice which represents the cross-section of tubes with a pre-defined direction. The circular sections of the tubes are presented as ellipses. 57

5.1 Basic principle of corrosion model implementation: (a) Initial corroding and corresponding source (retracting) face are the same (green face). (b) The oxide starts to grow and continuously fills the volume of the cell (red), taking the retraction of the boundary into consideration. (c) After the cell is completely filled potential faces to neighbouring cells are the new corroding faces (dark red). The distance to the initial source face (green) is calculated, including its retraction. Now two corroding faces obtain the Cr-ions from one source face $\rightarrow n = 2$ and the growth is limited, to ensure mass conservation of the Cr-ions [77]. 60

5.2 Sketch showing the influence of the voxel geometry on the growth and the need for a geometry correction factor. The initial surface (green line) is approximated by voxel (thick black line). Cells that are corroding from more than one side are filled earlier, resulting in an overestimation of the oxide growth. 61

5.3 Evaluated sample slice of the microstructure. Connected pores are highlighted in different colours [78]. 66

5.4 Reconstructed microstructure of the metallic support with an 200 µm long inlet and an 400 µm long outlet section. The inlet section should be long enough to form a parabolic flow profile, while the outlet section should assure that no back-flow occurs. In the case of the higher velocity (a) the inlet, as well as the outlet section is too short and the streamlines indicate back-flow. At lower velocities (b) both sections are sufficiently large and straight streamlines can be observed. 68

6.1 The simulated and theoretical oxide thickness and mass gain for a simple test geometry with oxide growth only in one direction [77]. 75

6.2 Rotated square with an edge length of 10 µm, where the edges are represented by stair steps. The oxide thickness after 500 h is shown. 75

6.3 Comparison of the oxide thickness for the square geometry shown in Figure 6.3 computed with and without the growth correction and the 1-D growth. 76

6.4 Oxide growth on a simple geometry representing a ring with a diameter of 10 µm, which is discretized using equidistant voxel with a volume of $1 \times 10^{-21}\,\mathrm{m}^3$. Fully corroded areas are coloured red, while in the blue regions no oxide is prevailing. The inner part of the ring is referred to as concave, while the outer part is convex. Note: The metal-retraction is only calculated and stored at the boundary faces (in this case the initial ring (black)), with no change of the initial geometry [77]. 77

6.5 Comparison of the oxide thickness between a concave (inward) and a convex (outward) geometry. Only a slight difference of the average oxide layer thicknesses between the concave and convex curvature can be discerned and a good agreement with the 1-D parabolic rate law is achieved [77]. 78

6.6 Calculated oxide thickness of the concave (inward) and convex (outward) geometry without the growth limitation. Both cases overestimate the analytical oxide thickness. 79

6.7 Computed and theoretical mass gain of the concave (inward) and convex (outward) geometry [77]. 80

6.8 Comparison between the corrosive scale of a metallic support SEM and the computational result thereof. The dark grey and the red areas indicate the measured and the computed oxide [77]. 81

6.9 2-D slice showing the computed oxide of a full 3-D metallic support after 40 000 h at 850 °C in simulated anode gas with $p_{H_2O}/p_{H_2} = 9$. Here only the pores are shown. Red indicates fully corroded areas, while blue areas have got no oxide [77]. 82

6.10 Measured and computed mass gain of a metallic support at 650 °C. The linear combined with the parabolic approach shows a very good agreement, while the sole parabolic approach underestimates the mass gain in the beginning and shows a faster growth in the end. 83

6.11 Comparison between the bulk and the superficial velocity in the microstructure. In an ideal microstructure both velocities are the same, but in real microstructure deviations can be observed. 85

6.12 Pressure drop in the artificial geometry together with a vector plot of the velocity. The dimensions of the microstructure are 222 µm × 286 µm × 213 µm, with a 100 µm long in- and outlet section. 87

6.13 Influence of the pressure gradient on the concentration over-potential for the Maxwell-Stefan model. 89

6.14 Description of the annotation of the patches and applied boundary conditions in the simulation. 91

6.15 p_{H_2O} dependency of the diffusion related processes in the anode (measurement data according to [9]). 93

7.1 Porosity distribution along the three coordinate axes for the windowing geometry with a base area of 350 µm × 350 µm. The z-direction is the diffusion path from the gas-channel to the anode functional layer. While the directions parallel to the gas-channel show an homogeneous porosity distribution, the diffusion path orthogonal to the gas channel has a much lower porosity in the first 100 µm compared to the rest of the electrode. The gas-channel interface is located at 0 µm and the interface to the anode functional layer at 350 µm [78]. 98

7.2 Mean pore diameter distribution along the diffusion path. The gas-channel interface is at 0 µm and the interface to the anode functional layer at 350 µm [78]. 99

7.3 Number of pores per m^2 along the diffusion path. In the first 100 µm there are less pores compared to the rest of the metallic support. The gas-channel interface will be at 0 µm and the interface to the anode functional layer at 350 µm. The base area is 200 µm × 200 µm [78]. 100

7.4 Calculated pressure drop in the microstructure for different superficial velocities (red dots) and fitted function. 101

7.5 Calculated relative pressure drop in the reconstructed metallic support. Flow direction is from left (gas-channel interface) to right (anode-functional-layer interface). The superficial velocity is $5 \times 10^{-3}\,\mathrm{m\,s^{-1}}$. The streamlines (depicted as tubes) indicate that only some continuous pores are present, due to dense interface between the gas-channel and the metallic support. 102

7.6 Computed concentration gradient of hydrogen in one reconstructed microstructure. The interface between the gas-channel and the metallic support is at 0 µm and the interface between the metallic support and the anode-functional-layer lies at 350 µm. 103

7.7 Principal depiction of the metallic support with the 100 µm thick dense upper layer (referred to as *dense*) and the more porous 250 µm of the remaining metallic support (referred to as *porous*). Homogenised parameters (referred to as *hom*) are calculated for the entire height of 350 µm [78]. 104

7.8 Computed averaged porosity of five different sample geometries. The volume of each reconstructed geometry is 200 µm × 200 µm × 350 µm. With ongoing corrosion the porosity is decreasing [77]. 107

7.9 Initial porosity distribution along the diffusion path of one representative geometry (200 µm × 200 µm × 350 µm) compared to the porosity after 40 000 h corrosion at different temperatures. The interface to the gas-channel is at 0 µm and the interface to the anode functional layer at 350 µm [77]. 107

7.10 Calculated averaged scaling factor difference for five independent reconstructed geometries. The geometry size is 200 µm × 200 µm × 350 µm and the change of the microstructure due to corrosion was computed at 650 °C, 750 °C and 850 °C. The averaged scaling factor f for a non-corroded sample is 1.19×10^{-2}. Note: The scaling factor is the ratio between the binary and the effective diffusion coefficient [77]. 108

7.11 Averaged mass fraction distribution along the diffusion path after 20 000 h for different temperatures in a volume of 200 µm × 200 µm × 350 µm. The molar fraction of hydrogen is fixed to 0.9 at the interface between the gas-channel and the metallic support, while a fixed gradient (a fixed flux of hydrogen) is applied on the metallic support anode-functional-layer interface. The lateral boundaries are partly periodic and symmetry [77]. 110

Bibliography

[1] Martin Andersson, Jinliang Yuan and Bengt Sunden. "Review on modeling development for multiscale chemical reactions coupled transport phenomena in solid oxide fuel cells". In: *Applied Energy*, vol. 87, no. 5 (2010), pp. 1461–1476.

[2] R. Arbter, J. M. Beraud, C. Binetruy, L. Bizet, J. Bréard, S. Comas-Cardona, C. Demaria, A. Endruweit, P. Ermanni, F. Gommer, S. Hasanovic, P. Henrat, F. Klunker, B. Laine, S. Lavanchy, S. V. Lomov, A. Long, V. Michaud, G. Morren, E. Ruiz, H. Sol, F. Trochu, B. Verleye, M. Wietgrefe, W. Wu and G. Ziegmann. "Experimental determination of the permeability of textiles: A benchmark exercise". In: *Composites Part A: Applied Science and Manufacturing*, vol. 42, no. 9 (2011), pp. 1157–1168.

[3] A Atkinson. "Transport processes during the growth of oxide films at elevated temperature". In: *Reviews of Modern Physics*, vol. 57, no. 2 (1985), pp. 437–469.

[4] Jacob Bear. *Dynamics of fluids in porous media*. New York: Dover, 1988.

[5] Wolfgang G. Bessler, Stefan Gewies and Marcel Vogler. "A new framework for physically based modeling of solid oxide fuel cells". In: *Electrochimica Acta*, vol. 53, no. 4 (2007), pp. 1782–1800.

[6] R. Byron Bird, Warren E. Stewart and Edwin N. Lightfoot. *Transport Phenomena*. John Wiley & Sons, 2007.

[7] P. Blennow, J. Hjelm, T. Klemenso, A. H. Persson, S. Ramousse and M. Mogensen. "Planar Metal-Supported SOFC with Novel Cermet Anode". In: *Fuel Cells*, vol. 11, no. 5 (2011), 661–668.

[8] Peter Blennow. *Gas permeability data on metal-supports*. e-mail. 2013.

[9] Peter Blennow, Johan Hjelm, Trine Klemenso, Severine Ramousse, Alexander Kromp, Andre Leonide and Andre Weber. "Manufacturing and characterization of metal-supported solid oxide fuel cells". In: *Journal of Power Sources*, vol. 196, no. 17 (2011). 9th European SOFC Forum, Lucerne, Switzerland, 2010, 7117–7125.

[10] Bloom Energy. URL: `http://www.bloomenergy.com/` (visited on 01/12/2014).

[11] Gunilla Borgefors and Ingela Nyström. "Efficient shape representation by minimizing the set of centres of maximal discs/spheres". In: *Pattern Recognition Letters*, vol. 18, no. 5 (1997), pp. 465–471.

[12] R. Bove and S. Ubertini. *Modeling Solid Oxide Fuel Cells: Methods, Procedures and Techniques*. Springer, 2008. ISBN: 978-1-4020-6995-6.

[13] Robert Brodkey. *The Phenomena Of Fluid Motions*. New York: Dover, 1995.

[14] Thorsten M Buzug. *Computed tomography from photon statistics to modern cone-beam CT*. Berlin: Springer, 2008.

[15] N. Cabrera and N. F. Mott. "Theory of the oxidation of metals". In: *Reports on Progress in Physics*, vol. 12, no. 1 (1949).

[16] Fatma N. Cayan, Suryanarayana R. Pakalapati, Francisco Elizalde-Blancas and Ismail Celik. "On modeling multi-component diffusion inside the porous anode of solid oxide fuel cells using Fick's model". In: *Journal of Power Sources*, vol. 192, no. 2 (2009), pp. 467–474.

[17] Ceres Power. URL: `http://www.cerespower.com/` (visited on 01/12/2014).

[18] S. H. Chan, K. A. Khor and Z. T. Xia. "A complete polarization model of a solid oxide fuel cell and its sensitivity to the change of cell component thickness". In: *Journal of Power Sources*, vol. 93, no. 1-2 (2001), pp. 130–140.

[19] Wai-Pak Choi, Kin-Man Lam and Wan-Chi Siu. "Extraction of the Euclidean skeleton based on a connectivity criterion". In: *Pattern Recognition*, vol. 36, no. 3 (2003), pp. 721–729.

[20] Daniel P. Combest, Andrew Jackson and Eugene de Villers. "Advanced pre-processing and meshing with snappyHexMesh". In: 8th OpenFOAM Workshop. South Korea, Jeju, 2013. URL: http://sourceforge.net/projects/openfoam-extend/files/OpenFOAM_Workshops/OFW8_2013_Jeju/Tue/ (visited on 25/09/2014).

[21] P. Costamagna, A. Selimovic, M. Del Borghi and G. Agnew. "Electrochemical model of the integrated planar solid oxide fuel cell (IP-SOFC)". In: *Chemical Engineering Journal*, vol. 102, no. 1 (2004), pp. 61–69.

[22] Henry Darcy. *Les fontaines publiques de la ville de Dijon : exposition et application des principes suivre et des formules employer dans les questions de distribution d'eau*. V. Dalmont (Paris), 1856.

[23] elcore GmbH. URL: http://www.elcore.com/de/home.html (visited on 01/12/2014).

[24] Norman Epstein. "On tortuosity and the tortuosity factor in flow and diffusion through porous media". In: *Chemical Engineering Science*, vol. 44, no. 3 (1989), pp. 777–779.

[25] A. Faes, A. Hessler-Wyser, D. Presvytes, C. G. Vayenas and J. Van Herle. "Nickel-Zirconia Anode Degradation and Triple Phase Boundary Quantification from Microstructural Analysis". In: *Fuel Cells*, vol. 10, no. 2 (2010), pp. 325–325.

[26] Fibics Incorporated. *Introduction: Focused Ion Beam Systems*. URL: http://www.fibics.com/fib/tutorials/introduction-focused-ion-beam-systems/4/ (visited on 22/09/2014).

[27] Philipp Forchheimer. "Wasserbewegung durch boden". In: *Z. Ver. Deutsch. Ing*, vol. 45, no. 1782 (1901), p. 1788.

[28] Thomas Franco, Markus Haydn, Robert Mücke, André Weber, Matthias Rüttinger, Oliver Büchler, Sven Uhlenbruck, N. H. Menzler, Andreas Venskutonis and Lorenz S. Sigl. "Development of Metal-Supported Solid Oxide Fuel Cells". In: *ECS Transactions*, vol. 35, no. 1 (2011), pp. 343–349.

[29] Thomas Franco, Markus Haydn, Andre Weber, Wolfgang Schafbauer, Ludger Blum, Ute Packbier, Daniel Roehrens, Norbert H. Menzler, Juergen Rechberger, Andreas Venskutonis,

Lorenz S. Sigl and Hans Peter Buchkremer. “The Status of Metal-Supported SOFC Development and Industrialization at Plansee”. In: *ECS Transactions*, vol. 57, no. 1 (2013), pp. 471–480.

[30] Thomas Franco, R. Mücke, A. Weber, M. Haydn, M. Rüttinger, N. H. Menzler, A. Venskutonis, L. S. Sigl and H. P. Buchkremer. “Development and Industrialization of Metal-Supported Solid Oxide Fuel Cells”. In: *Proceedings of the 10th European Solid Oxide Fuel Cell Forum*. Ed. by F. Lefebbvre-Joud and Lefe. Lucerne, Switzerland, 2012,

[31] M. Garcia-Camprubi and N. Fueyo. “Mass transfer in hydrogen-fed anode-supported SOFCs”. In: *International Journal of Hydrogen Energy*, vol. 35, no. 20 (2010), pp. 11551–11560.

[32] Rafael C. Gonzalez and Richard E. Woods. *Digital Image Processing*. 3 edition. Upper Saddle River, N.J: Prentice Hall, 2007. 976 pp.

[33] D. Gostovic, J. R. Smith, D. P. Kundinger, K. S. Jones and E. D. Wachsman. “Three-Dimensional Reconstruction of Porous LSCF Cathodes”. In: *Electrochemical and Solid-State Letters*, vol. 10, no. 12 (2007), B214–B217.

[34] Kyle N. Grew, Aldo A. Peracchio, Abhijit S. Joshi, John R. Izzo Jr. and Wilson K.S. Chiu. “Characterization and analysis methods for the examination of the heterogeneous solid oxide fuel cell electrode microstructure. Part 1: Volumetric measurements of the heterogeneous structure”. In: *Journal of Power Sources*, vol. 195, no. 24 (2010), pp. 7930–7942.

[35] Naga Siva Kumar Gunda and Sushanta K. Mitra. “Direct Simulation of Transport Properties from Three-Dimensional (3D) Reconstructed Solid-Oxide Fuel-Cell (SOFC) Electrode Microstructures”. In: *Journal of Physics: Conference Series*, vol. 362, no. 1 (2012).

[36] B.A. Haberman and J.B. Young. “Three-dimensional simulation of chemically reacting gas flows in the porous support structure of an integrated-planar solid oxide fuel cell”. In: *International Journal of Heat and Mass Transfer*, vol. 47, no. 17–18 (2004), pp. 3617–3629.

[37] Anette N. Hansson, Jesper H. Hattel, Kristian V. Dahl and Marcel A. J. Somers. "Modelling Cr depletion under a growing Cr2O3 layer on austenitic stainless steel: the influence of grain boundary diffusion". In: *Modelling and Simulation in Materials Science and Engineering*, vol. 17, no. 3 (2009).

[38] Thinh X. Ho, Pawel Kosinski, Alex C. Hoffmann and Arild Vik. "Numerical modeling of solid oxide fuel cells". In: *Chemical Engineering Science*, vol. 63, no. 21 (2008), pp. 5356–5365.

[39] ISTI-CNR. *Meshlab*. URL: `http://meshlab.sourceforge.net/` (visited on 28/01/2014).

[40] John R. Izzo, Abhijit S. Joshi, Kyle N. Grew, Wilson K. S. Chiu, Andrei Tkachuk, Siew H. Wang and Wenbing Yun. "Nondestructive Reconstruction and Analysis of SOFC Anodes Using X-ray Computed Tomography at Sub-50 nm Resolution". In: *Journal of The Electrochemical Society*, vol. 155, no. 5 (2008), B504.

[41] Hrovje Jasak. "Error Analysis and Estimation for the Finite Volume Method with Applications to Fluid Flows". PhD thesis. Imperial College, 1996.

[42] Hrovje Jasak. "Finite Volume Discretisation in OpenFOAM: Best Practice Guidelines". Eighth OpenFOAM Workshop, Jeju, Korea University, 2013. URL: `www.cfluid.com/bbs/attachment.php?aid=25586` (visited on 30/01/2014).

[43] Hrovje Jasak. "Hands-On Training with OpenFOAM External Aerodynamics: Ahmed Body". Cyprus Advanced HPC Workshop, 2012. URL: `http://www.linksceem.eu/ls2/images/stories/Hands-On_Training_with_OpenFOAM_-_External_Aerodynamics_-_Ahmed_Body.pdf` (visited on 30/01/2014).

[44] Denny A. Jones. *Principles and Prevention of Corrosion*. Prentice Hall, 1996.

[45] Jochen Joos, Thomas Carraro, André Weber and Ellen Ivers-Tiffée. "Reconstruction of porous electrodes by FIB/SEM for detailed microstructure modeling". In: *Journal of Power Sources*, vol. 196, no. 17 (2011), pp. 7302–7307.

[46] Jochen Joos, Moses Ender, Thomas Carraro, André Weber and Ellen Ivers-Tiffée. "Representative volume element size for accurate solid oxide fuel cell cathode reconstructions from focused ion beam tomography data". In: *Electrochimica Acta*, vol. 82 (2012), pp. 268–276.

[47] P.S. Jorgensen, K.V. Hansen, R. Larsen and J.R. Bowen. "High accuracy interface characterization of three phase material systems in three dimensions". In: *Journal of Power Sources*, vol. 195, no. 24 (2010), pp. 8168–8176.

[48] Sadik Kakac, Anchasa Pramuanjaroenkij and Xiang Yang Zhou. "A review of numerical modeling of solid oxide fuel cells". In: *International Journal of Hydrogen Energy*, vol. 32, no. 7 (2007), pp. 761–786.

[49] Willi Kalender. *Computed tomography: fundamentals, system technology, image quality, applications*. Erlangen: Publicis Corporate Pub., 2011.

[50] Kitware Inc. *ParaView*. URL: `http://www.paraview.org/` (visited on 20/01/2014).

[51] L. J. Klinkenberg. "The Permeability Of Porous Media To Liquids And Gases". In: *Drilling and Production Practice* (1941).

[52] A. Kräuter. *Matrixalgebra*. Lecture notes. 2013.

[53] R. Krishna and J. A. Wesselingh. "Review article number 50 - The Maxwell-Stefan approach to mass transfer". In: *Chemical Engineering Science*, vol. 52, no. 6 (1997), pp. 861–911.

[54] K. Kwok, P. S. Jorgenson and H. L. Frandsen. "Micromechanical Modeling of Solid Oxide Fuel Cell Anode Supports based on Three-dimensional Reconstructions". In: European Fuel Cell Forum. Switzerland, Luzern, 2014.

[55] J. Laurencin, R. Quey, G. Delette, H. Suhonen, P. Cloetens and P. Bleuet. "Characterisation of Solid Oxide Fuel Cell Ni-8YSZ substrate by synchrotron X-ray nano-tomography: from 3D reconstruction to microstructure quantification". In: *Journal of Power Sources*, vol. 198 (2012), pp. 182–189.

[56] J. Leixnering, B. Gschaider, W. Brandstätter and R. Bouwman. “A Multiscale Simulation Approach for Diesel Particulate Filter Design Based on OpenFOAM and DexaSIM”. In: *OpenFOAM International Conference*. Old Windsor, UK., 2007.

[57] A. Leonide, V. Sonn, A. Weber and E. Ivers-Tiffée. “Evaluation and Modeling of the Cell Resistance in Anode-Supported Solid Oxide Fuel Cells”. In: *Journal of The Electrochemical Society*, vol. 155, no. 1 (2008), B36–B41.

[58] Thomas Malkow. “SOFC in Brief”. In: *Modeling solid oxide fuel cells: methods, procedures and techniques*. Ed. by R. Bove and S. Ubertini. Springer, 2008. Chap. 1.

[59] Yuriy B. Matus, Lutgard C. De Jonghe, Craig P. Jacobson and Steven J. Visco. “Metal-supported solid oxide fuel cell membranes for rapid thermal cycling”. In: *Solid State Ionics*, vol. 176, no. 5–6 (2005), pp. 443–449.

[60] S. Molin, M. Gazda and P. Jasinski. “Coatings for improvement of high temperature corrosion resistance of porous alloys”. In: *Journal of the European Ceramic Society*, vol. 31, no. 14 (2011), pp. 2707–2710.

[61] S. Molin, M. Gazda, B. Kusz and P. Jasinski. “Evaluation of 316 L porous stainless steel for SOFC support”. In: *Journal of the European Ceramic Society*, vol. 29, no. 4 (2009), pp. 757–762.

[62] Sebastian Molin, Maria Gazda and Piotr Jasinski. “High temperature oxidation of porous alloys for solid oxide fuel cell applications”. In: *Solid State Ionics*, vol. 181, no. 25-26 (2010), pp. 1214–1220.

[63] Sebastian Molin, Boguslaw Kusz, Maria Gazda and Piotr Jasinski. “Evaluation of porous 430L stainless steel for SOFC operation at intermediate temperatures”. In: *Journal of Power Sources*, vol. 181, no. 1 (2008), pp. 31–37.

[64] Aydin Nabovati, Edward W. Llewellin and Antonio C. M. Sousa. “A general model for the permeability of fibrous porous media based on fluid flow simulations using the lattice Boltzmann method”. In: *Composites Part A: Applied Science and Manufacturing*, vol. 40, no. 6 (2009), pp. 860–869.

[65] George J. Nelson, William M. Harris, Jeffrey J. Lombardo, John R. Izzo Jr., Wilson K.S. Chiu, Pietro Tanasini, Marco Cantoni, Jan Van herle, Christos Comninellis, Joy C. Andrews, Yijin Liu, Piero Pianetta and Yong S. Chu. "Comparison of SOFC cathode microstructure quantified using X-ray nanotomography and focused ion beam–scanning electron microscopy". In: *Electrochemistry Communications*, vol. 13, no. 6 (2011), pp. 586–589.

[66] S. P. Neuman. "Theoretical derivation of Darcy's law". In: *Acta Mechanica*, vol. 25, no. 3 (1977), pp. 153–170.

[67] T. J. Nijdam, L. P. H. Jeurgens and W. G. Sloof. "Modelling the thermal oxidation of ternary alloys—compositional changes in the alloy and the development of oxide phases". In: *Acta Materialia*, vol. 51, no. 18 (2003), pp. 5295–5307.

[68] T. J. Nijdam and W. G. Sloof. "Effect of reactive element oxide inclusions on the growth kinetics of protective oxide scales". In: *Acta Materialia*, vol. 55, no. 17 (2007), pp. 5980–5987.

[69] T. J. Nijdam and W. G. Sloof. "Modelling of composition and phase changes in multiphase alloys due to growth of an oxide layer". In: *Acta Materialia*, vol. 56, no. 18 (2008), pp. 4972–4983.

[70] Valerio Novaresio, Maria Garcia-Camprubi, Salvador Izquierdo, Pietro Asinari and Norberto Fueyo. "An open-source library for the numerical modeling of mass-transfer in solid oxide fuel cells". In: *Computer Physics Communications*, vol. 183, no. 1 (2012), pp. 125–146.

[71] openCV. *Open-source computer vision*. URL: `http://opencv.org/` (visited on 22/09/2014).

[72] OpenFOAM Foundation. *OpenFOAM. The open source CFD toolbox. User Guide. Version 2.2.2*. URL: `http://foam.sourceforge.net/docs/Guides-a4/UserGuide.pdf` (visited on 21/01/2014).

[73] Suhas Patankar. *Numerical Heat Transfer and Fluid Flow*. CRC Press, 1980.

[74] Bruce E. Poling, John M. Prausnitz and John P. O'Connell. *The Properties of Gases and Liquids*. Auflage: 5 Sub. New York: Mcgraw-Hill Professional, 2000.

[75] W M Pragnell and H E Evans. "A finite-difference model to predict 2D depletion profiles arising from high temperature oxidation of alloys". In: *Modelling and Simulation in Materials Science and Engineering*, vol. 14, no. 4 (2006), pp. 733–740.

[76] python. URL: `https://www.python.org/` (visited on 22/09/2014).

[77] Georg Reiss, Henrik L. Frandsen, Christian Weiß and Wilhelm Brandstätter. "Numerical Evaluation of the Oxide Growth in Metal-supported Solid Oxide Fuel Cells and its Influence on Mass Transport". In: *Journal of Power Sources* (2015). (submitted).

[78] Georg Reiss, Henrik Lund Frandsen, Wilhelm Brandstätter and André Weber. "Numerical evaluation of micro-structural parameters of porous supports in metal-supported solid oxide fuel cells". In: *Journal of Power Sources*, vol. 273 (2015), pp. 1006–1015.

[79] Adrian E. Scheidegger. *The physics of flow through porous media*. University of Toronto Press, 1974.

[80] SciPy.org. URL: `https://www.scipy.org/` (visited on 03/11/2014).

[81] P.R. Shearing, J. Gelb and N.P. Brandon. "X-ray nano computerised tomography of SOFC electrodes using a focused ion beam sample-preparation technique". In: *Journal of the European Ceramic Society*, vol. 30, no. 8 (2010), pp. 1809–1814.

[82] Lihua Shen and Zhangxin Chen. "Critical review of the impact of tortuosity on diffusion". In: *Chemical Engineering Science*, vol. 62, no. 14 (2007), pp. 3748–3755.

[83] T. G. Sherwood, R. L. Pigford and C. R. Wilke. "Diffusion in porous material". In: *Mass Transfer*. Ed. by B.J Clark and J.W. Maisel. McGraw-Hill Inc., 1975, pp. 39–43.

[84] R. Suwanwarangkul, E. Croiset, M. W. Fowler, P. L. Douglas, E. Entchev and M. A. Douglas. "Performance comparison of Fick's, dusty-gas and Stefan-Maxwell models to predict the concentration overpotential of a SOFC anode". In: *Journal of Power Sources*, vol. 122, no. 1 (2003), pp. 9–18.

[85] G. Taubin. "Curve and surface smoothing without shrinkage". In: IEEE Comput. Soc. Press, 1995, pp. 852–857.

[86] Ross Taylor and R. Krishna. *Multicomponent Mass Transfer*. John Wiley & Sons, 1993.

[87] Chih-Long Tsai and V. Hugo Schmidt. "Tortuosity in anode-supported proton conductive solid oxide fuel cell found from current flow rates and dusty-gas model". In: *Journal of Power Sources*, vol. 196, no. 2 (2011), pp. 692–699.

[88] K. Tseronis, I. K. Kookos and C. Theodoropoulos. "Modelling mass transport in solid oxide fuel cell anodes: a case for a multidimensional dusty gas-based model". In: *Chemical Engineering Science*, vol. 63, no. 23 (2008), pp. 5626–5638.

[89] H. Y. Tu and U. Stimming. "Advances, aging mechanisms and lifetime in solid-oxide fuel cells". In: *Journal of Power Sources*, vol. 127, no. 1 (2004), pp. 284–293.

[90] Michael C. Tucker. "Progress in metal-supported solid oxide fuel cells: A review". In: *Journal of Power Sources*, vol. 195, no. 15 (2010), pp. 4570–4582.

[91] Michael C. Tucker, Grace Y. Lau, Craig P. Jacobson, Lutgard C. DeJonghe and Steven J. Visco. "Performance of metal-supported SOFCs with infiltrated electrodes". In: *Journal of Power Sources*, vol. 171, no. 2 (2007), pp. 477–482.

[92] Michael C. Tucker, Grace Y. Lau, Craig P. Jacobson, Lutgard C. DeJonghe and Steven J. Visco. "Stability and robustness of metal-supported SOFCs". In: *Journal of Power Sources*, vol. 175, no. 1 (2008), pp. 447–451.

[93] N. Vernet, E. Ruiz, S. Advani, J. B. Alms, M. Aubert, M. Barburski, B. Barari, J. M. Beraud, D. C. Berg, N. Correia, M. Danzi, T. Delavière, M. Dickert, C. Di Fratta, A. Endruweit, P. Ermanni, G. Francucci, J. A. Garcia, A. George, C. Hahn, F. Klunker, S. V. Lomov, A. Long, B. Louis, J. Maldonado, R. Meier, V. Michaud, H. Perrin, K. Pillai, E. Rodriguez, F. Trochu, S. Verheyden, M. Wietgrefe, W. Xiong, S. Zaremba and G. Ziegmann. "Experimental determination of the permeability of engineering textiles: Benchmark II". In: *Composites Part A: Applied Science and Manufacturing*, vol. 61 (2014), pp. 172–184.

[94] N. Vivet, S. Chupin, E. Estrade, T. Piquero, P.L. Pommier, D. Rochais and E. Bruneton. "3D Microstructural characterization of a solid oxide fuel cell anode reconstructed by focused ion beam tomography". In: *Journal of Power Sources*, vol. 196, no. 18 (2011), pp. 7541–7549.

[95] Yasemin Vural, Lin Ma, Derek B. Ingham and Mohamed Pourkashanian. "Comparison of the multicomponent mass transfer models for the prediction of the concentration overpotential for solid oxide fuel cell anodes". In: *Journal of Power Sources*, vol. 195, no. 15 (2010), pp. 4893–4904.

[96] Carl Wagner. "Fehlordnungserscheinungen in kristallisierten polaren Verbindungen als Grundlage für Elektronen- und Ionen-Leitung". In: *Zeitschrift für Elektrochemie und angewandte physikalische Chemie*, vol. 39, no. 7b (1933), pp. 543–545.

[97] Jun Wang and Ying Tan. "Efficient Euclidean distance transform algorithm of binary images in arbitrary dimensions". In: *Pattern Recognition*, vol. 46, no. 1 (2013), pp. 230–242.

[98] Shuping Wang, William M. Worek and W. J. Minkowycz. "Performance comparison of the mass transfer models with internal reforming for solid oxide fuel cell anodes". In: *International Journal of Heat and Mass Transfer*, vol. 55, no. 15-16 (2012), pp. 3933–3945.

[99] Zhijie Xu, Kevin M. Rosso and Stephen Bruemmer. "Metal oxidation kinetics and the transition from thin to thick films". In: *Physical Chemistry Chemical Physics*, vol. 14, no. 42 (2012), pp. 14534–14539.

[100] C. L. Y. Yeong and S. Torquato. "Reconstructing random media". In: *Physical Review E*, vol. 57, no. 1 (1998), pp. 495–506.

[101] Harumi Yokokawa, Hengyong Tu, Boris Iwanschitz and Andreas Mai. "Fundamental mechanisms limiting solid oxide fuel cell durability". In: *Journal of Power Sources*, vol. 182, no. 2 (2008), pp. 400–412.

[102] ZEISS. *Electron Microscopes for Life Sciences*. URL: `http://applications.zeiss.com/C125792900358A3F/0/F64E45CDE7BFA130C1257C1F003562B3/$FILE/EN_41_010_021_EM-for-LifeSciences.pdf` (visited on 14/01/2014).